Synthesis and Characterization of Precursors for Chemical Vapor Deposition of Metal Oxide Thin Films

by

May D. Nyman

Thesis submitted to the Faculty of the Virginia Polytechnic Institute and State University in partial fulfillment of the requirements for the degree of

Masters of Science

in

Materials Science and Engineering

APPROVED:

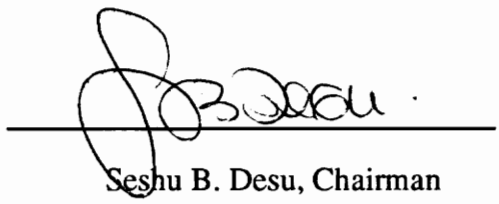

Seshu B. Desu, Chairman

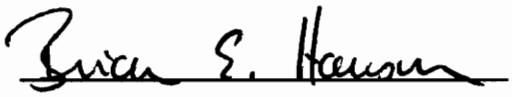

Brian E. Hanson

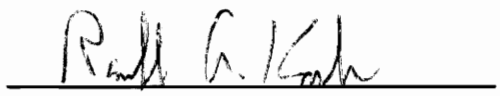

Ronald G. Kander

July, 1992

Blacksburg, Virginia

SYNTHESIS AND CHARACTERIZATION OF PRECURSORS FOR CVD OF METAL OXIDE THIN FILMS

by

May Nyman

Committee Chairman: Seshu B.Desu

Materials Science and Engineering

(ABSTRACT)

Optimal precursor behavior during Chemical Vapor Deposition (CVD) is crucial for reproducible synthesis of high quality thin films. Desirable precursor properties include: 1) volatility and thermal stability at <180 °C (10 - 100 millitorr vapor pressure at atmospheric pressure) 2) low decomposition temperature (350-550 °C) to metal oxide with minimal organic ligand contamination and 3) ambient stability and minimal toxicity. Optimal selection and usage of CVD precursors is implemented by synthesis and characterization studies. Additionally, precursor synthesis and characterization studies render the development of novel precursors, which are specifically engineered for the CVD process.

Lead bis-tetramethylheptadione [$Pb(thd)_2$], lead bis-heptafluorodimethyloctadione [$Pb(fod)_2$], and zirconium tetrakis-tetramethylheptadione [$Zr(thd)_4$], which are lead and zirconium precursors for CVD of $Pb(Zr_xTi_{1-x})O_3$ thin films, and T8-hydridospherosiloxane, which is a silica precursor, were synthesized and purified. Free ligand was the predominant impurity from the lead and zirconium precursor syntheses, and the T8 synthesis produced several byproducts including T10-hydridospherosiloxane and a polymer. The lead and zirconium precursors were purified by recrystallization from

toluene, and the T8 was purified by extracting the byproducts with pentane. Purity of $Pb(thd)_2$, $Pb(fod)_2$ and $Zr(thd)_4$ was confirmed by melting point determination, carbon and hydrogen elemental analysis and proton nuclear magnetic resonance spectrometry (NMR). Purity of T8 was confirmed by proton NMR.

Isothermal gravimetric analysis (TGA) was used to study volatility and thermal stability of the precursors. The $Zr(thd)_4$ isotherms ranged from 180-260 °C, the $Pb(thd)_2$ and $Pb(fod)_2$ isotherms were 80-200 °C, and the T8 isotherms were 80-140 °C. Vapor pressure was calculated from TGA data, with use of diffusion equations. Precursors exhibited vapor pressure ranging from 0.2 - 600 millitorr, over their respective vaporization temperature ranges. Enthalpy of vaporization was calculated from Arrhenius plots of vapor pressure as a function of temperature. The $Zr(thd)_4$ and T8 were observed to be thermally stable over the temperature ranges and durations of experiments. The $Pb(thd)_2$ and $Pb(fod)_2$ are not thermally stable over the vaporization temperatures, and undergo oligomerization when heated at high vaporization temperatures. Addition of a polyether adduct to the lead precursor was proposed to inhibit oligomer formation at high vaporization temperatures.

Precursor decomposition studies were executed in sealed quartz tubes. Products of decomposition were examined by infrared spectrometry, mass spectrometry, and solid state NMR spectrometry. Metal oxide formation from decomposition of precursors was observed at ; 300-350 °C for T8, 350-550 °C for $Zr(thd)_4$, 250-350 °C for $Pb(thd)_2$, and 300 °C for $Pb(fod)_2$. Lead fluoride became the dominant phase of $Pb(fod)_2$ decomposition products above 300 °C. Intermediate decomposition products of all the precursors were documented and discussed. Synthesis and/or isolation of intermediate decomposition products of $Zr(thd)_4$, $Zr_2O_2(thd)_4$, was proposed as a novel precursor for ZrO_2 deposition.

ACKNOWLEDGEMENTS

Many thanks to committee members; Dr. Seshu Desu, Dr. Brian Hanson and Dr. Ron Kander for guidance and assistance in the completion of this document. Thanks to Seshu Desu for allowing me the opportunity to carry out this endeavor, and I am grateful for his infinite patience, and for allowing me so much latitude to learn and work independently. I would also like to thank Brian Hanson for getting me into graduate school (twice)!! Additionally, I am grateful for the use of his lab for one year, his willingness to always help, and the many, many lessons (both fundamental and specific) of chemistry. Thanks to Dr. Pradyot Agaskar, who was also fundamental in the initiation of this project.

I would also like to the thank all the members of the ever-growing thin film lab. Special thanks go to; C. H. Peng for assistance with many aspects of this project (IR analyses, T8 studies, and general discussions on precursor problems), and thanks for always being an inspiration to work hard. Thanks to Jhing Fang Chang, Jie Si and Claire Chen for assistance in synthesis and helping Prof. Qiu, thanks to Prof. Chen and Tsai for assistance with diffusion laws, and thanks to Chiu and Warren for help with vapor pressure studies. Many thanks to all of you I haven't mention yet for just being good friends and colleagues (Chi Kwok, Gene Li, Prof. Qiu, Justin Gaynor, Ashraf, Dr. Yoo, Dr. Ashok, Dillip Vijay, and anyone else I might have forgotten!)

Also, thanks to the various technicians who have assisted; Kim Harrich (mass spec), Bill Bebout, Tom Glass, and Geno Iannaccone (NMR), and Jim Hollenhead (TGA).

Finally, I'd like to thank my husband Matthew Nyman. Without him, graduate school would not have been nearly as enjoyable. His constant encouragement, support, advice and comfort was most valuable. He provided much tangible assistance, as well; including help with diagrams for various presentations, and doing more than his share of household chores (without complaint!!) when I was too wrapped up in school. I look forward to doing it again in New Mexico!

TABLE OF CONTENTS

TABLE OF CONTENTS (continued)

INDEX TO FIGURES

CHAPTER 1

CHAPTER 2

CHAPTER 3

INDEX TO FIGURES (continued)

INDEX TO TABLES

CHAPTER 2

CHAPTER 3

Chapter 1: INTRODUCTION

Numerous thin film materials including metals (i.e. Cu, Al), binary metal oxides (i.e. TiO_2, Ta_2O_5, SiO_2), semiconductor materials (i.e. Si, ZnS, GeAs, InP), polymers (i.e. parylenes, PMMA) and complex metal oxides such as superconductors (i.e. $YBa_2Cu_3O_7$) and ferroelectrics (i.e. $PbTi_xZr_{1-x}O_3$) are routinely deposited by Chemical Vapor Deposition (CVD) processes.

Some CVD methods involve thermal evaporation of a precursor compound, transportation of the evaporated precursor compound to the substrate by a carrier gas, and decomposition of the precursor on the substrate to form the desired thin film material. One basis of categorizing CVD methods is the variation of energy sources used to initiate precursor decomposition to the thin film material. Thermal CVD, photo-assisted CVD, plasma-assisted CVD, and laser-assisted CVD are some examples of Chemical Vapor Deposition techniques. Thermal CVD , in which precursor decomposition is assisted by thermal energy, offers simplicity of method and flexability (i.e. applicable to a variety of precursors) of method, which is not provided by altermative methods.

Thermal CVD conditions effect some properties of the deposited thin films including film composition, phase, and microstructure. The behavior of specific thin film materials such as ferroelectrics, dielectrics, superconductors, semiconductors and piezoelectrics is also affected by deposition parameters. Chemical Vapor Deposition conditions which can be varied to control film properties include: carrier gas composition, temperature of deposition, reactor pressure, rate of deposition, and carrier gas flow rate. Optimization of these CVD deposition conditions is highly dependant on precursor properties. In the following section, the role of the precursor during the CVD process is

described. Additionally, effects of precursor behavior on thin film properties deposited by the CVD process are exemplified.

1.1 Precursor role in the CVD process

The role of the precursor can be summarized in terms of the subsequent "zones" it encounters during CVD, which is depicted schematically in figure 1.1. In zone A, the precursor compound is heated at a suitable temperature at which evaporation will occur. The evaporated precursor specie enters a carrier gas stream, in which it is transported through zone B and into the furnace (zone C). The furnace and/or substrates within the furnace are heated at a temperature which will permit thermal decomposition of the precursor to thin film material on the substrates. If the furnace is a "cold wall reactor", deposition will ideally occur only on the substrates; a "hot wall reactor" will produce deposition on all surfaces within the furnace. Appropriate carrier gas composition is also necessary for thermal decomposition of the precursor in zone C to produce the desired thin film material. For instance, an oxidizing gas such as O_2 or N_20 may be necessary for CVD of metal oxide films, and a reducing gas such as H_2 may be necessary for the growth of metal films. The thermal decomposition step is made up of a series of chemical and physical reactions involving the vapor phase precursor and carrier gases, the substrate and the film surface. Sequential processes of thermal decomposition include gas phase reactions of precursors, adsorption of precursor and/or intermediate products of decomposition onto the surface, surface diffusion, nucleation and growth of film, and desorption of volatile byproducts of precursor decomposition (i.e. the organic ligand of an organometallic compound).[1] Under conditions of suitable vaporization temperature, decomposition temperature, and carrier gas composition, thin film growth by CVD is achievable. More specifically, each individual precursor requires a unique set of

parameters for successful CVD of thin film materials, and not all precursor compounds are equally suitable for all CVD processes.

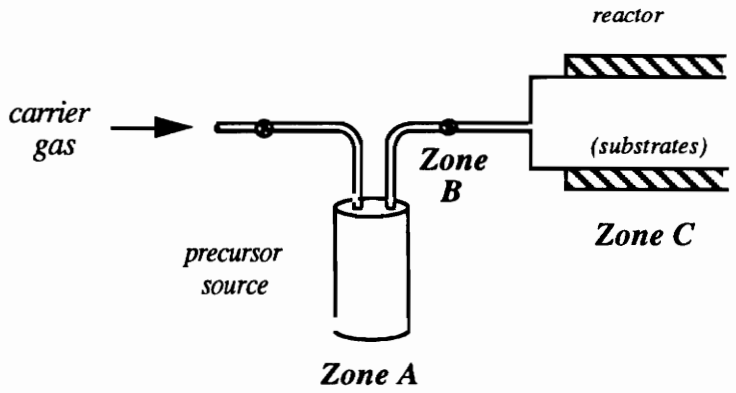

Figure 1.1 Chemical Vapor Deposition Schematic

An ideal precursor for CVD of thin film materials must behave diametrically in subsequent zones A/B and C. In zones A and B, the precursor must be volatile and thermally stable at vaporization temperatures (i.e.10-100 millitorr vapor pressure at <180 °C). High precursor volatility ensures a sufficient amount enters the furnace in the gas phase; consequently, film growth rates and thicknesses are adequate. Thermal stability of the precursor at vaporization temperature is necessary so that vaporization rate is constant over the course of the CVD experiment. If decomposition coincides with vaporization in zone A, vapor pressure will decrease over time. In zone B, the vapor phase precursor is transported from the source to the furnace in the carrier gas stream. Thermal stability and volatility of the precursor must be maintained in this zone; e.g. condensation or decomposition en route to the furnace should not occur. In order to retain the vapor phase precursor without condensation, zone B should be at the same temperature as zone A, or slightly hotter. However, if zone B of the CVD apparatus is too hot, thermal

decomposition will occur unfavorably. In summary, precursor volatility and thermal stability at vaporization temperature in zones A and B ensure consistent and predictable film growth rates during the course of the CVD experiment.

In zone C, the precursor must exhibit rapid decomposition with minimal film contamination from organic ligands of the precursor (i.e. metal fluoride or metal carbide formation) at low substrate temperatures (preferably 350-550 °C). Low decomposition temperature is desirable for; 1) efficiency of experiment and apparatus design and 2) elimination of undesirable reactions of the thin film material with the substrate. Although low decomposition temperature is necessary for the above-mentioned reasons, the temperature should be high enough to produce desirable phase and/or decomposition rate. If plentiful precursor and necessary carrier gases are available in the furnace (i.e. amount of reactants is not the rate controlling factor of the decomposition reaction), the precursor decomposition rate is a function of decomposition temperature.

Although precursor vaporization temperature and precursor decomposition temperature are both ideally low, the difference between the temperatures should be as large as possible:

$$T(\text{decomposition}) - T(\text{vaporization}) = \Delta T$$

ΔT is ideally small as possible

T(decomposition) is low as possible

If the temperature at which vaporization of the precursor occurs is close to the temperature at which decomposition occurs, then decomposition will likely occur in zones A and B.

One additional desirable precursor property is ease of handling. This is not a trivial concern, because many of the compounds which possess the afore-mentioned, desirable properties are often air sensitive, light sensitive, moisture sensitive, toxic, or pyrophoric.

Extreme precautions must be taken in both the storage and usage of compounds with these undesirable properties. Additionally, precursors which are not stable under ambient conditions might behave unpredictably and inconsistently, due to alteration during storage.

In summary, a precursor for CVD of a thin film material must possess the following properties: 1) high vapor pressure at low vaporization temperature (i.e. 10-100 millitorr at <180 °C) 2) thermal stability at vaporization temperature, and at 50 °C above vaporization temperature 3) rapid decomposition at low temperature (i.e. 350-550 °C) with minimal contamination from the organic constituents of the precursors 4) stability under ambient conditions and nontoxicity.

1.2 Studies of precursor behavior under CVD conditions

As suggested by the above discussion, many properties of thin film materials produced by the CVD method are affected by precursor behavior during the various steps of the process. Therefore, thin film properties can be optimized by altering the various CVD parameters which in turn are determined by the precursor behavior (i.e. vaporization temperature, decomposition temperature). Moreover, a precursor can be engineered so that it possesses desirable properties for the CVD process. Understanding precursor behavior during Chemical Vapor Deposition is most fundamental in optimization of the process for a chosen precursor. Numerous studies focused on the understanding of precursor behavior have been reported in the literature. All of these experiments can be trivially categorized as; 1) CVD experiments or 2) non-CVD experiments. The CVD experiments are subdivided as; a) real time studies of precursor behavior and b) indirect studies of precursor behavior. Real time studies involve interfacing of CVD apparatus with a spectrometric device (i.e. UV-Vis, IR, mass spec), through which precursor behavior can be examined directly during the course of the experiment. Indirect

studies involve executing numerous CVD experiments under a matrix of variable parameters, and inferring precursor behavior by trends observed in the resulting thin film properties. Non-CVD experiments include any in which a potential precursor in subjected to conditions which simulate CVD, and the behavior is studied as a function of these conditions. In this section, the afore-mentioned methods of studying CVD precursor behavior are discussed, and exemplified by literature reports.

1.2.1 CVD experiments

1.2.1.1 Precursor behavior inferred from film properties

This approach involves examination of a film characteristic as a function of a single CVD parameter which directly affects precursor behavior. For instance, film thickness can be used to study precursor volatility as a function of vaporization temperature. Okada et al. [2] and Si et al. [3] independently reported ZrO_2 film growth variation as a function of vaporization temperature of the precursor. Precursor decomposition rate as a function of substrate temperature can also be determined by variation in film growth rate. Okada et al. [2] studied lead zirconium titanate (PZT) film growth rate as a function of substrate temperature for various combinations of lead, zirconium and titanium precursors. Tsuruoka et al. [4] reported Y-Ba-Cu oxide (YBCO) thin film growth rate as a function of substrate temperature.

Decomposition of the precursor.is also affected by carrier gas composition, which can be examined in terms of film properties. For instance, Tsuruoka et al.[4] discussed the effect of different oxidizing gases (O_2 and N_2O) on the growth rates of YBCO films. Parson et al. [5] demonstrated that fluorine contamination in films deposited from fluorinated precursors can be eliminated with the addition of water vapor to the carrier gas stream.

Indirect studies of thin film precursors by CVD experiments are problematic for several reasons. These experiments are time consuming and potentially expensive, because only one parameter can be altered at a time in order to study the effect of that parameter. Additionally, most information about precursors which can be inferred from CVD experiments is quantitative. It is more difficult to obtain qualitative data, such as mechanisms of decomposition. Most importantly, an ambiguity is presented by the many CVD parameters; alteration of a single CVD parameter will more likely produce multiple responses, rather than a single response.

1.2.1.2 Precursor behavior in real time CVD

This type of study involves interfacing of analytical equipment with the CVD apparatus. For instance, a spectrometer (i.e. infrared spectrometer, mass spectrometer) can be set up at various positions on the apparatus to sample the gas phase precursors in subsequent zones A, B and C. Comita and Kodas [6] interfaced a mass spectrometer with laser-assisted CVD apparatus, and sampled the gas phase reactants and products of decomposition in real time. Heidberg et al. [7] also used laser-assisted CVD combined with mass spectrometry to study precursor decomposition mechanisms by sampling gas phase reactants and products. Braichotte and van den Bergh [8] used laser-assisted CVD combined with real time optical transmittance to examine precursor decomposition mechanisms. Rate-determining steps of decomposition were inferred from variation in concentration of gas phase precursor in the "boundary layer" as a function of applied laser power.

In situ studies have been very successful with laser-assisted CVD; however, there are some major difficulties with the interfacing of a thermal CVD apparatus with spectrometric equipment. A "hot wall reactor" is heated throughout, usually to temperatures greater than 300 °C. Consequently, interfacing with a spectrometer is

logistically difficult. Although the "cold wall reactor" is more suitable for interfacing, decomposition of precursor is minimal and localized. Therefore, monitoring of products of decomposition would be difficult because a large concentration of nondecomposed precursor would dominate the spectrometer samplings. Another difficulty presented by thermal CVD is the inability to pulse the decomposition energy source. Because the energy source for laser-assisted CVD can be pulsed, reactants and products of decomposition can be examined separately, if the spectrometer samples both in phase and out of phase with the laser. In situ spectra of the thermal CVD reactions would indiscriminately sample both gas phase reactants and products simultaneously.

1.2.2 Non-CVD experiments

An alternative approach to characterization of precursor behavior during CVD involves individual experiments in which a potential precursor is subjected to conditions which simulate that which are encountered during the CVD process. A potential precursor is a metal-containing compound which possesses characteristics necessary for the CVD process. These include volatility, thermal stability, rapid and clean decomposition mechanisms. Clean decomposition is defined as decomposition with minimal contamination from organic constituents which result in metal carbide or metal fluoride formation. Frequently, reported characterization studies of potential precursors were intended for applications other than CVD, such as separation of metal mixtures by gas chromatography of volatile metal compounds (see below). However, these reports document characteristics of potential precursors which are highly applicable to CVD studies.

Many volatility experiments, such as thermogravimetric and gas chromatographic, were carried out on metal β-diketonates to implement analytical separations of complex

metal mixtures. Metal β-diketonates represent a class of volatile metal chelates which is presently widely exploited for CVD of many thin film materials. These earlier studies provide valuable information pertaining to the compounds' usefulness for the CVD process. Pertinent studies include thermogravimetric separations of groups of metal β-diketonates which have been carried on the alkaline earth metals [9], and rare earth metals. [10, 11, 12, 13] Also applicable to CVD precursor issues are studies involving gas chromatography techniques to separate groups of metal β-diketonates, such as transition metals and main group IIA and IIIB metals. [14, 15, 16] Characterization of metal β-diketonate volatility by both thermogravimetry and gas chromatography have also been reported for alkaline earth metals [17] and rare earth metals [18], and transition metals[19].

Thermal decomposition experiments of metal β-diketonates have also been reported. [20 21] In these experiments main group IA and IIA metals and first row transition metals were thermally decomposed, and the gas phase byproducts were monitored via mass spectrometry. Although there was no mention in these studies about the potential applications to CVD, information concerning thermal stability and decomposition mechanisms of potential CVD precursors (metal β-diketonates) is provided. Bradley [22] have reported extensive studies on volatility and thermal decomposition of metal alkoxides, another class of volatile metal compounds which have been exploited for CVD applications. Although much of Bradley's research dates back to before there was an interest in metal alkoxides as precursors for CVD, his experiments provide valuable data concerning the volatility and decomposition conditions and mechanisms of these CVD precursor compounds.

More recently, characterization experiments of potential precursors have been executed for application to the CVD process of thin film synthesis. For instance, precursors for CVD of copper thin films have been well characterized in terms of volatility,

thermal stability, and decomposition mechanisms [23, 24, 25]. Sirio et al. [24] and Pauleau and Dulac [26] characterized some aluminum precursors for application to CVD. Another well-studied set of precursors is that which is used for CVD of Yttrium-Barium-Copper Oxide (Y-Ba-Cu-O) superconducting thin films. This system presents some challenging problems, due to the thermal instability of the barium oxide precursors. Harima et al. [27, 28] documented decomposition mechanisms of yttrium, barium and copper precursors via thermogravimetric, DSC and infrared spectrometry experiments. Yuhya et al. [29] characterized volatility properties of Y-Ba-Cu-O precursors via vapor pressure experiments, thermogravimetry and DSC. Turnipseed et al. [30] used mass spectrometry and thermogravimetry to examine the thermal stability of Y-Ba-Cu-O precursors. Gardiner et al. [31] reported volatility and thermal stability of barium precursors, which were characterized via vapor pressure experiments and Single-Crystal X-Ray Analyses.

In summary of this section, precursors for Chemical Vapor Deposition can be studied by CVD experiments, as well as by experiments which approximate CVD conditions. Although the non-CVD experiments exemplified above do not possess the same elegance as the real-time experiments, they provide exemplary information pertaining to precursor behavior during the CVD experiment. Additionally, non-CVD precursor experiments are less expensive and logistically simpler to execute than real-time experiments. They are also not constrained by the CVD reactor conditions; for instance, poor pressure and heat control within the CVD system limits vapor pressure studies.

1.3 Objectives of study

Studies of precursor behavior under CVD conditions assist in successful precursor selection and usage by providing a base of knowledge which can be utilized in the following manners: 1) optimization of CVD conditions in order to produce optimal quality

thin films from a chosen precursor 2) selection of the best precursor for a given film, substrate and set of CVD parameters 3) design of novel precursors which possess optimal properties for the CVD process.

The objective of the study presented herein is to devise a protocol for synthesis, purification and characterization of precursors for CVD, in order to obtain the afore-mentioned advantages for precursor selection and usage. Precursors which studies were focused on include zirconium tetrakis-tetramethylheptadione [$Zr(thd)_4$], lead bis-tetramethylheptadione [$Pb(thd)_2$], lead bis-heptafluorodimethyloctadione [$Pb(fod)_2$] and O_h-hydridospherosiloxane [T8].

The $Zr(thd)_4$, $Pb(thd)_2$, and $Pb(fod)_2$ are members of a large class of coordination compounds called metal β-diketonates with the general formula $M^{n+}(ROCCHCOR)_n$, where R is an alky or fluoroalkyl group. $Pb(fod)_2$, $Pb(thd)_2$ and $Zr(thd)_4$ are useful as precursors for CVD of lead-based ferroelectrics such as lead titanate or $Pb(Zr_xTi_{1-x})O_3$ [PZT]. The hydridospherosiloxane, $H_8Si_8O_{12}$, or T8, is a cagelike structure of Si-O-Si bonds with octahedral symmetry. T8 belongs to the spherosiloxane group which has a general formula of $(RSiO_{1.5})_n$. T8 is a novel precursor for SiO_2 thin films. Silicon dioxide thin films are useful for numerous applications including semiconductor applications, antireflection coatings, high temperature optical filters and thermal stabilizers of solar cells.[32]

The lead and zirconium metal β-diketonate precursors are discussed in chapter 2. Synthesis of the three compounds is described; the $Zr(thd)_4$ synthesis was optimized from a literature report, and the $Pb(fod)_2$ and $Pb(thd)_2$ were synthesized by a novel method. Purification and purity analyses are discussed. Volatility and thermal stability of the precursors is characterized by thermogravimetric and mass spectrometry techniques. Vapor pressures of the precursors is calculated from the thermogravimetric data. Precursor

decomposition experiments are analyzed via infrared spectrometry and mass spectrometry. The precursors are discussed in terms of their usefulness for the CVD process. Additionally, designs for novel precursors which are optimized for CVD processes are formulated from the studies.

The studies of T8-hydridospherosiloxane reported in chapter 3 follow the same basic outline as chapter 2. Literature methods of synthesis, purification and purity analysis are reported. Thermogravimetry was used to characterized the volatility, thermal stability, and to calculate vapor pressures. Decomposition experiments to form SiO_2 were studied via infrared spectrometry and ^{29}Si solid state NMR. The novel precursor is discussed in terms of its suitability for the CVD process, compared to the suitability of alternative SiO_2 precursors which have been reported in the literature.

---

1 Jensen, Klavs F. and Kern, Werner; "Thermal Chemical Vapor Deposition"; Thin Film Processes II, (edited by Kern and Vossen), Academic Press, Chapter III, (1991).

2 Okada, Masaru; Tominaga, Koji; Araki, Teruhiko; Katayama, Shigehisa; and Sakashita, Yukio, "Metalorganic Chemical Vapor Deposition of c-Axis Oriented PZT Thin Films", Japanese Journal of Applied Physics, 29 (4), pp 718-722, (1990).

3 Si, Jie; Peng, Chien H. and Desu, Seshu B.; "Deposition and Characterization of Metalorganic Chemical Vapor Deposition of ZrO_2 Thin Films Using $Zr(thd)_4$", Materials Research Society Symposium Proceeding, (Fall 1992), vol 250.

4 Tsuruoka, Taiji; Kawasaki, Ryodo; and Abe, Hitoshi, "Y-Ba-Cu-O Film Growth by OMCVD Using N2O", Japanese Journal of Applied Physics, 28, (10), pp L1800-L1802, (1989).

5 Parson, A.J.; Charles, R.J.; Schmidt, D.N., Scedon, J.R.; Mickiko, G.K.; Braginski, A.I., "Chemical Vapor Deposition of YBa2Cu3O7 Using Metalorganic Chelate Precursors", Applied Physics Letters, 53 (18), pp 1756-1758, (1988).

6 Comita, Paul E. and Kodas, Toivo T., "Modulated Laser Beam Relaxation Spectrometry of Laser-induced Chemical Vapor Deposition", Applied Physics Letters, 51, (25), pp 2059-2061, (1987).

7 Heidberg, Joachim; Daghighi-Ruhi, Rahman; Von Weyssenhoff. Hanns; and Habekost, Achim. "Laser-stimulated Noble Metal Deposition from Gaseous and Condensed Acetylacetonates. Photoreactions in the Supersonic Jet and Above Silicon". Materials Research Society Symposium Proceedings, 101, pp 221-229, (1988).

8 Braichotte, D. and van den Bergh, H. "Gas Phase versus Surface Contributions to Photolytic Laser Chemical Vapor Deposition Rates", Applied Physics A, 45, pp 337-343, (1988).

9 Reichert, C.; Bancroft, G.M.; Westmore, J.B., "Mass Spectral Studies of Metal Chelates. V. Mass spectra and appearance potentials of some fluorine-substituted acetylacetonates", Canadian Journal of Chemistry, 48, pp 1362-2370, (1970).

10 Fujinaga, Taitiro; Kuwamota, Tooru; Sugiura, Kenji; Matsubara, Norio, "Fundamental Investigation of Thermal Properties of Rare-Earth b-Diketonates", Talanta, 28, pp 295-300, (1981).

11 Fujinaga, T.; Kuwamota, T.; and Murai, S., "Gas Chromatography of Metal Chelates with Carrier Gas Containing Ligand Vapor", Analytica Chimica Acta, 71, pp 141-150, (1974).

12 Fujinaga, T.; Kuwamota, T.; and Murai, S., "Gas Chromatography of metal chelates with carrier gas containing ligand vapor: thorium trifluoroacetylacetonate", Analytica Chimica Acta, 71, pp 141-150, (1971).

13 Richardson, Mary Frances and Sievers, Robert E.; "Volatile Rare Earth Chelates of 1,1,1,5,5,5-Hexafluoro-2,4-pentanedione and 1,1,1,2,2,3,3,7,7,7-Decafluoro-4,6-heptanedione", Inorganic Chemistry, 10 (3), pp 498-504, (1971).

14 Schwarberg, J.E.; Moshier, R.W. and Walsh, J.H., "Feasibility of Gas-Liquid Chromatography for Quantitative Determination of Aluminum (III), Gallium (III), Indium(III) and Beryllium (II) Trifluoroacetylacetonates", Talanta, 11, pp 1213-1224, (1964).

15 Sievers, Robert E.; Ponder, B.W.; Morris, Melvin L.; and Moshier, Ross W., "Gas Chromatography of Metal Chelates of Acetylacetone, Trifluoroacetylacetone, and Hexafluoroacetylacetone", Inorganic Chemistry, 2 (4), pp 693-698, (1963).

16 Sievers, Robert E.; Connolly, Joseph W.; and Ross, William D., "Metal Analysis by Gas Chromatography of Chelates of Heptafluorodimethyloctadione", Journal of Gas Chromatography, pp 241-247, (May 1967).

17 R. Belcher; Cranley, C.R.; Majer, J.R.; Stephen, W.I and Uden, P.C., "Volatile Alkaline Earth Chelates of Fluorinated Alkanoylpivalylmethanes", Analytica Chimica Acta, 60 pp 109-116, (1972).

18 Springer, Charles S.; Meek, Devon W.; and Sievers, Robert E., "Rare Earth Chelates of 1,1,1,2,2,3,3-Heptafluoro-7,7-dimethyl-4,6-octanedione", Inorganic Chemistry, 6 (6), pp 1105-1110, (1967).

19 Wolf, Wayne R.; Sievers, Robert E; Brown, Glenn H., "Vapor Pressure Measurements and Gas Chromatographic Studies of the Solution Thermodynamics of Metal β-diketonates", Inorganic Chemistry, 11 (9), pp 1995-2002, (1972)..

20 Von Hoene, Joan; Charles, Robert G.; and Hickam, William M., "Thermal Decomposition of Metal Acetylacetonates", Journal of Physical Chemistry, 62, pp 1098-1101, (Sept. 1958)

21 Charles, Robert G. and Pawlikowski, M. Arlene; "Comparative Heat Stabilities of Some Metal Acetylacetonate Chelates", Journal of Physical Chemistry, 62, pp 440-444, (1958).

22 Bradley, D.C.; Mehrotra, R.C.; Gaur, P.D. "Metal Alkoxides", Academic Press: (1978).

23 Jain, A; Chi, K.M.; Kodas, T.T.; Hampden-Smith, M.J.; Farr, J.D. and Paffett, M.F., "Chemical Vapor Deposition of Copper from (Hexafluoroacetylacetonato)(alkyne)-copper (I) Complexes via Disproportionation", Chemistry of Materials, 3, pp 997-999, (1991).

24 Pauleau, Y. and Fasasi, A.Y., "Kinetics of Sublimation of Copper (II) Acetylacetonate Complex Used for Chemical Vapor Deposition of Copper Films", Chemistry of Materials, 3, pp 45-50, (1991).

25 Sirio, C.; Poncelet, O.; Hubert-Pfalzgraf, L.G.; Daran, J.C. and Vaissermann, J.; "Reactions Between Copper (II) β-diketonates and Metal Alkoxides as a Route to Soluble and Volatile Copper (II) Oxide Precursors: Synthesis and Molecular Structure of $Cu_4(\mu_3\eta^1\text{-}OC_2H_4IO^iPr)_4(acac)_4$ and $(acac)Cu(\mu\text{-}OSiMe_3)_2Al(OSiMe_3)_2$", Polyhedron, 11 (2), pp 177-184, (1992).

26 Pauleau, Y. and Dulac, O.; "Vaporization Processes of Aluminum β-Diketone Chelates", Chemistry of Materials, 3, pp 280-286, (1991)

27 Harima, Hiroshi; Ohnishi, Hiroshi; Hanaoka, Ken-ichi; Tachibana, Kunihide; Kobayashi, Minoru and Hoshinouchi, Susumu, "Spectroscopic Study on a Discharge Plasma of MOCVD Source Gases for High-Tc Supercoductig Films", Japanese Journal of Applied Physics, 29 (10), pp 1932-1938 (October, 1990).

28 Harima, Hiroshi; Ohnishi, Hiroshi; Hanaoka, Ken-ichi; Tachibana, Kunihide; Goto, Yoshiyuki, "An IR Study on the Stability of Y(DPM)3, Ba(DPM)2, and Cu(DPM)2 for UV Irradiation", Japanese Journal of Applied Physics, 30 (9A), pp 1946-1955, (September 1991).

29 Yuhya, S. et al, "Volatilities of Precursors for CVD of Superconducting Thin Films" pp 232-235

30 Turnipseed, S.B.; Barkley, R.M. and Sievers, R.E., "Synthesis and Characterization of Alkaline-Earth-Metal b-diketonate Complexes Used as Precursors for Chemical Vapor Deposition of Thin-Film Superconductors", Inorganic Chemistry, 30 (6), pp 1164-1170, (1991).

31 Gardiner, R.; Brown, D.W.; Kirlin, P.S.; Rheingold, A.L., "Volatile Barium b-Diketonate Polyether Adducts. Synthesis, Characterization, and Metalorganic Chemical Vapor Deposition", Chemistry of Materials, 3 (6), pp 1053-1059, (1991).

32 Desu, S.B.; Agaskar, P.A.; Peng, C.H.; and Tian, S., "Low Temperature CVD of SiO2 using Novel Precursors", (Accepted by the Electrochemical Society; to be published summer 1992)

Chapter 2: LEAD AND ZIRCONIUM β-DIKETONATES

2.1 Introduction

2.1.1 Precursor choice for CVD of PZT

2.1.1.1 Metal alkoxides and metal alkyls

Chemical Vapor Deposition of PZT thin films usually requires three precursors; one titanium compound, one zirconium compound and one lead compound. Metal alkoxides, with the general formula $M^{n+}(OR)_n$ are a group of volatile metal complexes which have been exploited as CVD precursors. Titanium alkoxides, such as titanium isopropoxide perform well under both ambient and CVD conditions. Titanium isopropoxide is reasonably stable under ambient conditions, it does not present any extreme health hazards, vaporization temperatures as low as 30 °C have been reported as suitable for the CVD process,[1] and it decomposes cleanly to TiO_2 at 400 °C. On the other hand, the analogous zirconium alkoxides are somewhat problematic. Although zirconium alkoxides are sufficiently volatile for the CVD process at low vaporization temperatures (CVD source temperature of 30 °C is reported for zirconium t-butoxide[1]), they undergo a hydrolysis process which produces more water upon exposure to very small amounts of atmospheric moisture:

$$2\text{M-OR} + 2H_2O \text{ ----------> } 2\text{M-OH} + 2\text{R-OH} \quad (2.1)$$

$$2\text{M-OH} \text{ ----------> } \text{M-O-M} + H_2O \quad (2.2)$$

The difference in degree of moisture sensitivity of the titanium alkoxides and the zirconium alkoxides is a function of the metal atom size. Both are d^0 metals in the (IV) oxidation state, and are very electronegative. The smaller Ti^{4+} ion is somewhat shielded from atmospheric moisture by its organic ligands, but the larger Zr^{4+} ion is not completely shielded by its ligands, and reacts with atmospheric moisture.

Simple lead alkoxides and lead alkyls have also proven to be problematic. To be used as a CVD precursor for PbO[1], tetraethyl lead must be cooled to -10 °C. The vapor pressure of tetraethyl lead at room temperature presents a significant toxicity problem. Additionally, lead alkyls are photosensitive, and decompose by free radical decay. Lead alkoxides are also liquids at room temperature, and possess significant vapor pressure which create toxicity problems. Additionally, the large Pb(IV) ion suffers the hydrolysis problem typical of metal alkoxides.

In general, metal alkoxides are highly volatile, decompose to metal oxides at low temperatures, are commercially available, and their thermal chemistry has been well documented.[2] The titanium alkoxide precursor exemplifies these advantages for the CVD process; however, the lead and zirconium alkoxides are less than ideal precursors for the CVD process. Zirconium and lead β-diketonates are potential alternatives.

2.1.1.2 Metal β-diketonates

Metal β-diketonates is a general class of chelating compounds which consists of a metal center of n^+ oxidation state, and 'n' number of chelating β-diketonate ligands (figure 2.1).

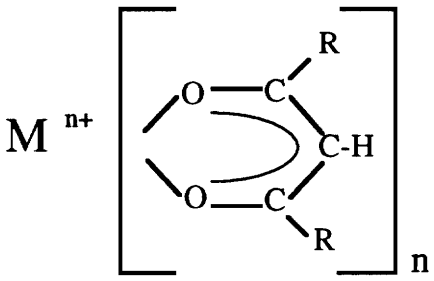

Metal β-diketonate

R = alkyl or fluoroalkyl group

Figure 2.1

Virtually all β-diketonate chelates are highly volatile (i.e. volatile enough to execute quantitative gas chromatography of metals), and β-diketonate chelates of most classes of metal are known.[3] The volatility of β-diketonate complexes of the first row transition metals increases with decreasing metal ion diameter. This is also well documented for the alkaline earth β-diketonates[4] and the rare earth β-diketonates[5,6,7]. A plausible reason for this phenomenon is more effective shielding of the metal center by the ligands with decreased metal size, thus decreasing molecular interactions. Molecular interactions which decrease volatility of metal β-diketonates include weak associations such as van der Waals forces, and stronger associations such as oligomer formation.[3] Oligomer formation is mostly observed for β-diketonate chelates of larger metals, as a means of increasing coordination number of the metal center.

Table 2.1 Lead β-diketonates (from Schweitzer)

Name	R_1, R_2	abbreviated name	T (°C) for 1 torr vapor pressure
lead bis-acetylaceonate	CH_3, CH_3	$Pb(acac)_2$	95
lead bis-trifluoroacetylacetonate	CF_3, CH_3	$Pb(tfa)_2$	72
lead bis-hexafluoroacetylacetonate	CF_3, CF_3	$Pb(hfa)_2$	67
lead bis-dimethylheptadione	CH_3, $C(CH_3)_3$	$Pb(dhd)_2$	76
lead bis-tetramethylheptadione	$C(CH_3)_3$, $C(CH_3)_3$	$Pb(thd)_2$	60
lead bis-heptafluoroheptadione	CH_3, C_3F_7	$Pb(fhd)_2$	95
lead bis-heptafluorodimethyloctadione	$C(CH_3)_3$, C_3F_7	$Pb(fod)_2$	68 (0.6 torr VP)

Metal β-diketonate volatility can be increased by variation of the R-groups on the chelate ring. In general, increased bulkiness of the R-group, and increased fluorine substitution on the R-group increases volatility. This trend is demonstrated for lead β-diketonates in table 2.1. The increased volatility is apparent with chelates of increased fluorination: $Pb(acac)_2 < Pb(tfa)_2 < Pb(hfa)_2$ and increased bulkiness: $Pb(acac)_2 < Pb(dhd)_2 < Pb(thd)_2$. Increased bulkiness of the ligand increases metal chelate volatility by preventing intermolecular interactions. Fluorination has the same effect, because fluorine atoms are somewhat larger than the protons for which they substitute.

Thermal stability of the metal β-diketonate is also sensitive to variation of the R-substituent and metal ion size. Effective shielding of the metal ion due to either small ion size or bulkiness of the ligand results in increased thermal and ambient stability. This effect can be explained in the same manner in which increased volatility of the metal β-diketonate is explained. Increased shielding of the metal center renders the compound less prone to intermolecular reactions to form oligomers, or reactions with water or oxygen to increase the coordination number.

2.1.2 Choice of precursors for this study

The discussion above reveals the importance of careful selection of the lead and zirconium precursors. Therefore, this chapter focuses on synthesis and characterization of several zirconium β-diketonates which appear to be promising as CVD precursors.

Premise for zirconium precursor selection for this study is based on past use of various lead and zirconium β-diketonates as CVD precursors in our lab. Chemical Vapor Deposition of ZrO_2 thin films from zirconium β-diketonate precursors is documented in a report by Desu, Tian and Kwok.[8] The precursors used include zirconium tetrakis-acetylacetonate and zirconium tetrakis-trifluoroacetylacetonate [$Zr(acac)_4$ and $Zr(tfa)_4$]. Low precursor vapor pressure and carbon contamination in the film rendered the $Zr(acac)_4$ unsuitable for CVD of ZrO_2. Films deposited from the $Zr(tfa)_4$ precursor contained fluorine. This previous study suggests a nonfluorinated β-diketonate with bulky R-groups which increase the precursor volatility might be suitable. Therefore zirconium tetrakis-tetramethylheptadione [$Zr(thd)_4$] (figure 2.2) was chosen for study.

In our lab, lead β-diketonates had not been extensively used as precursors for PbO at the initiation of this study. Therefore, lead bis-heptafluorodimethyloctadione [$Pb(fod)_2$] and lead bis-tetramethylheptadione [$Pb(thd)_2$] (figure 2.2) were chosen for study, based on their relative thermal stability and volatility, which was reported by Schweitzer[9] (Table 2.1). The thd complex, $Pb(thd)_2$, is an air stable solid (M.P. = 129 °C) with bulky t-butyl groups at all the R-sites. The fod complex, $Pb(fod)_2$, is also an air stable solid (M.P. = 76 °C) with a bulky t-butyl group at one R-site, and a heptafluoropropyl (also quite bulky) group at the other R-site. Both precursors have relatively high volatility (Table 2.1) and should be relatively thermally stable, due to the nature of the R-substituents.

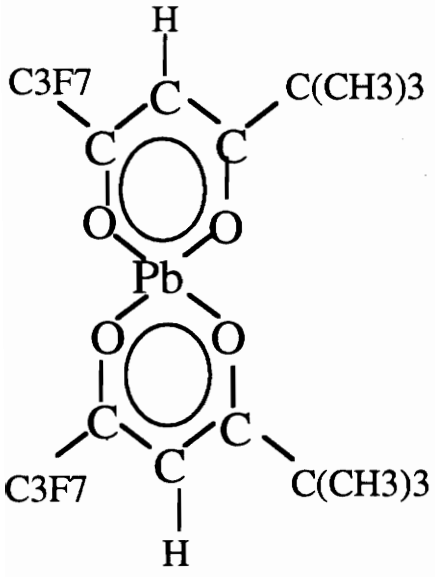

Pb(fod) 2

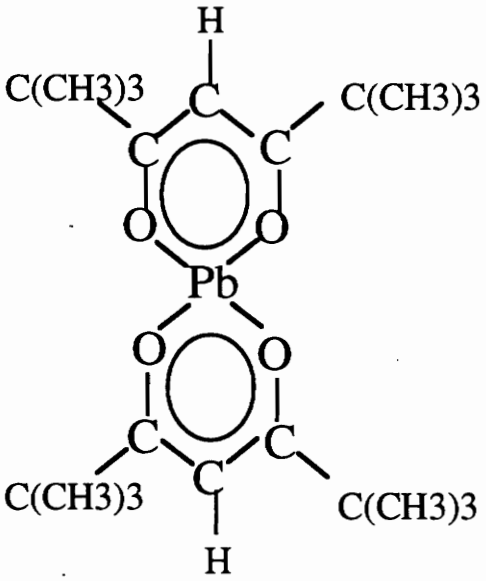

Pb(thd) 2

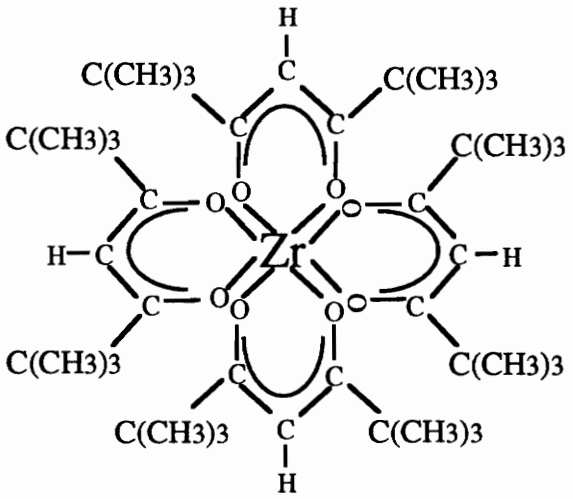

Zr(thd) 4

Figure 2.2 Metal β-diketonate precursors for lead and zirconium

The objective of the work presented herein is of dual nature. First, the specific intent of this study is to synthesize and purify $Pb(fod)_2$, $Pb(thd)_2$ and $Zr(thd)_4$, and examine their volatility, thermal stability and decomposition properties, and discuss the pertinence of these properties to the CVD process. The more general objective of this work is to establish a base of knowledge for CVD precursor studies. Methodology is presented to allow any given precursor, or class or precursors to be studied more efficiently and effectively, and to systematically develop novel precursors specifically engineered for the CVD process.

2.2 Experimental

2.2.1 Synthesis of Precursors

2.2.1.1 General Procedures

Some processes and instrumentation techniques were used for serveral of the syntheses, and will be covered in this section. Therefore, specific discussions of these techniques for individual precursors will be referenced to this section.

2.2.1.1.1 Purification of β-diketonate ligands

The protonated ligands, H-fod and H-thd are comercially avaliable by several suppliers such as Aldrich and Eastman-Kodak. The purity of the ligands is not consistant from one supplier to the next, and decomposition sometimes takes place over extended storage time. Decomposition is indicated by a discoloration of the oily ligand. In its pure form, it should be virtually colorless, and impure ligand is off-white to yellow. Therefore, purification of the β-diketonate ligand was occasionally necessary.

Impure ligands were distilled to rid them of yellow color (impurities from decomposition) via standard freeze-thaw pump cycles preceding the distillation. A bulb-to-bulb distillation apparatus (figure 2.3) was evacuated to 0.004 - 0.01 torr, flame dried, and backfilled with dry N_2. The ligand was syringed into flask A through the 24/40 neck, which was corked with a rubber septum. The ligand was frozen in a liquid nitrogen bath, and the apparatus was pumped down to 0.004 - 0.01torr (the working pressure of the mechanical pump before evacuating the apparatus). The system is then closed to the vacuum, and the ligand was thawed (can be assisted by warm tap water bath, 30-50 °C). Rapid degassing (boiling) took place upon thawing. The freeze-thaw pump cycle was repeated 3-4 times, or until the ligand did not rapidly boil upon thawing. Then the liquid nitrogen bath was transferred to flask B, the apparatus was opened to vacuum, and the ligand was distilled to flask B within several hours. The process was sped up to 45 minutes by adding a warm water bath to flask A during the distillation.

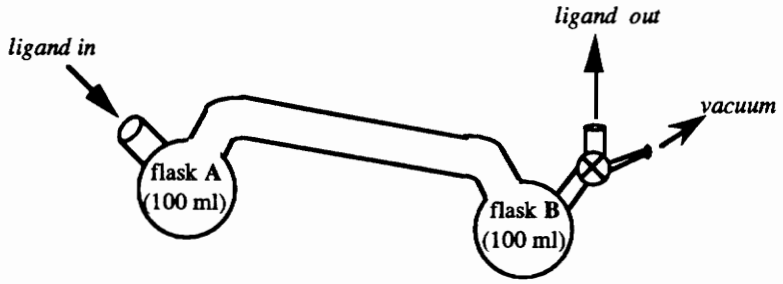

Figure 2.3 ligand purification apparatus

2.2.1.1.2 Purification of metal β-diketonates

All metal β-diketonates synthesized in this study were purified by recrystallization from toluene. The major impurity of the metal β-diketonates (both synthesized and purchased) is protonated ligand. Excess ligand is used for the synthesis reactions, so it is necessary to remove this impurity from synthesized metal β-diketonates. Additionally, zirconium tetrakis-acetylacetonate [$Zr(acac)_4$], the zirconium source for the $Zr(thd)_4$ synthesis, required recrystallization. The $Zr(acac)_4$, as purchased from Aldrich, was slightly yellow, rather than white. The yellow color increases with time and indicates the presence of protonated ligand, formed as a consequence of hygroscopic $Zr(acac)_4$ reacting with atmospheric moisture. The various metal β-diketonates differ in solubility in the toluene, optimum crystallization temperature, and optimum dissolution temperature. These specific details will be discussed accordingly. All toluene used for recrystallization was dried over sodium metal and benzophenone indicator, and distilled.

2.2.1.1.3 Proton NMR techniques

Since protonated ligand presented a significant impurity problem in the metal β-diketonates, proton NMR spectrometry of the compounds was executed with a focus on the enol peak (the enol proton replaces the metal in protonated β-diketonate ligands). All proton NMR spectra in this paper were obtained from a Bruker 200 instrument with a 5 mm probe. A sweep width 6024 Hz was used rather than the default value of 2994 Hz, in order to locate the enol peak (located at 14-17 ppm). Samples were dissolved in deuterated chloroform, and referenced to tetramethyl silane at 0 ppm (Hz/MHz operating frequency).

2.2.1.2 Synthesis and Purification of Precursors

2.2.1.2.1 Zirconium tetrakis-tetramethylheptadione

The reactants for the $Zr(thd)_4$ synthesis, $Zr(acac)_4$ and H-thd, were initially purified. The H-thd (catalog # 15,575-6, 95% purity) was purchased from Aldrich and purified (described in section 2.2.1.1.) The $Zr(acac)_4$ (Aldrich catalog # 33,800-1, 98% purity) was recrystallized from toluene 3-4 times, or until no yellow color was apparent. Solubility of $Zr(acac)_4$ is 1 g per 3 ml hot toluene (65 °C). The purity of recrystallized $Zr(acac)_4$ was confirmed by proton nuclear magnetic resonance spectroscopy. Protonated β-diketonate ligand impurity present in the metal β-diketonates is indicated via proton NMR by the enol peak, which substitutes in the metal position in the chelating ring. The enol peak of the H-acac (free ligand), which is located at 15.4 ppm was not be present in the pure $Zr(acac)_4$. Additionally, the methyl peak of the metal-bonded acetylacetonate ligand is shifted slightly upfield to 1.9 ppm from the methyl peak position at 2.1 ppm of the hydrogen-bonded acetylacetonate ligands. The methine peak of the hydrogen-bonded acetylacetonate is located at 5.4 ppm, as is the methine peak of the metal-bonded acetylacetonate. In addition to disappearance of the enol peak, absence of splitting or broadening of the methyl peak also indicates purity of $Zr(acac)_4$ (no detectable free ligand).

A modified version of the zirconium tetrakis-tetramethylheptadione [$Zr(thd)_4$] metathesis synthesis described by Pinnavaia et al. [10] was used. Modifications were necessary to minimize decomposition during the reaction, which is implemented by excessive heating, and use of impure reagents. Therefore, the heating time and temperature were reduced, and the reactants were distilled or recrystallized as appropriate, before use. Recrystallized zirconium tetrakis-acetylacetonate [$Zr(acac)_4$] (4.75 g., 9.89 mmol) and distilled tetramethylheptadione [H-thd] (28 ml, 136 mmol) were combined in a 100 ml

round bottom flask. The flask was equipped with a distilling head and distillate trap. The apparatus was purged with dry nitrogen at a constant rate (100-150 ml/min) (figure 2.4), and approximately 7 ml H-acac and H-thd was collected in the distillate trap. Passing a constant stream of nitrogen through the apparatus increased the rate of removal of H-acac and H-thd from the reaction flask. Therefore, the reaction was carried out at 120 °C for 12 hours, instead of 145 °C for 24 hours, as reported by Pinnavaia.[10] Lowering the temperature and decreasing the time of the experiment minimized thermal decomposition of the reactants during the course of the procedure.

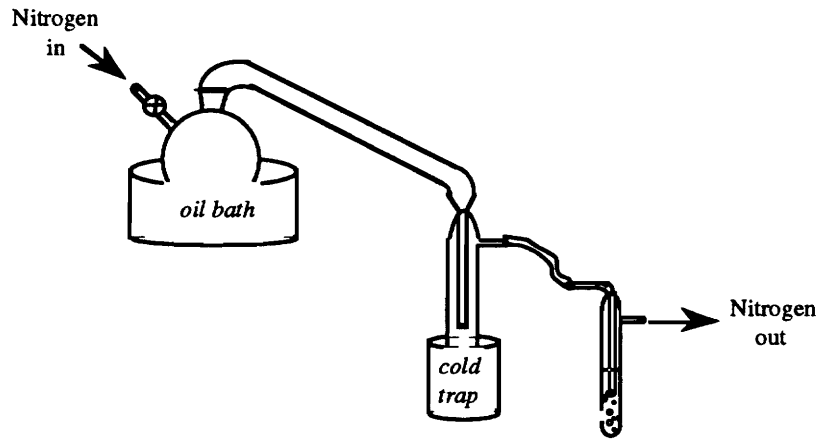

Figure 2.4 $Zr(thd)_4$ synthesis apparatus

The flask containing $Zr(thd)_4$ product and remaining H-acac and H-thd is equipped with a second distillation head and a cold trap. Freeze-thaw pump cycles (see section 2.2.1.1) under 0.004 - 0.01 torr are implemented to degas the excess ligand in the product mixture. During the thaw cycles, the product mixture was heated to 60-65 °C to ensure the H-thd melted, and degassing took place. A liquid nitrogen bath was then placed at the distillate trap, and H-acac and H-thd was removed under continuous vacuum, with the

product mixture at 65 °C. Next, the product was recrystallized from toluene 3-4 times, or until any yellow color disappeared, which was produced by thermal decomposition of reactants during the course of the metathesis reaction (section 2.2.1.2). The solubility of the $Zr(thd)_4$ product at this stage of purification is approximately 1-2 ml toluene per gram.Therefore, 5 ml toluene was added initially and the solution is heated and stirred. If dissolution is not complete, 1-5 more ml is added slowly until all $Zr(thd)_4$ is dissolved. Finally, the product was heated at 50 °C in vacuo to remove any excess ligand and solvent.

The product was a white crystalline product with melting point of 345 °C, which agrees with the melting point reported by Pinnavaia et al.[10] The yield from $Zr(acac)_4$ varied from 70 - 95% yield, depending on the amount recovered during recrystallization from toluene. The absence of any excess, nonbonded ligand was confirmed by proton nuclear magnetic resonance spectroscopy. The enol peak of H-thd at 16.1 ppm was not found in the final product (figure 2.5). Additionally, the methyl and methine peaks of the ligand complexing the Zr-metal center were located at 1.02 ppm and 5.7 ppm. The methyl peak is shifted upfield from the nonbonded ligand position of 1.12 ppm. The methine peak of the $Zr(thd)_4$ is unchanged from the H-thd position. The absence of the methyl peak at 1.12 ppm also suggested the lack of excess, nonbonded ligand. Carbon and hydrogen

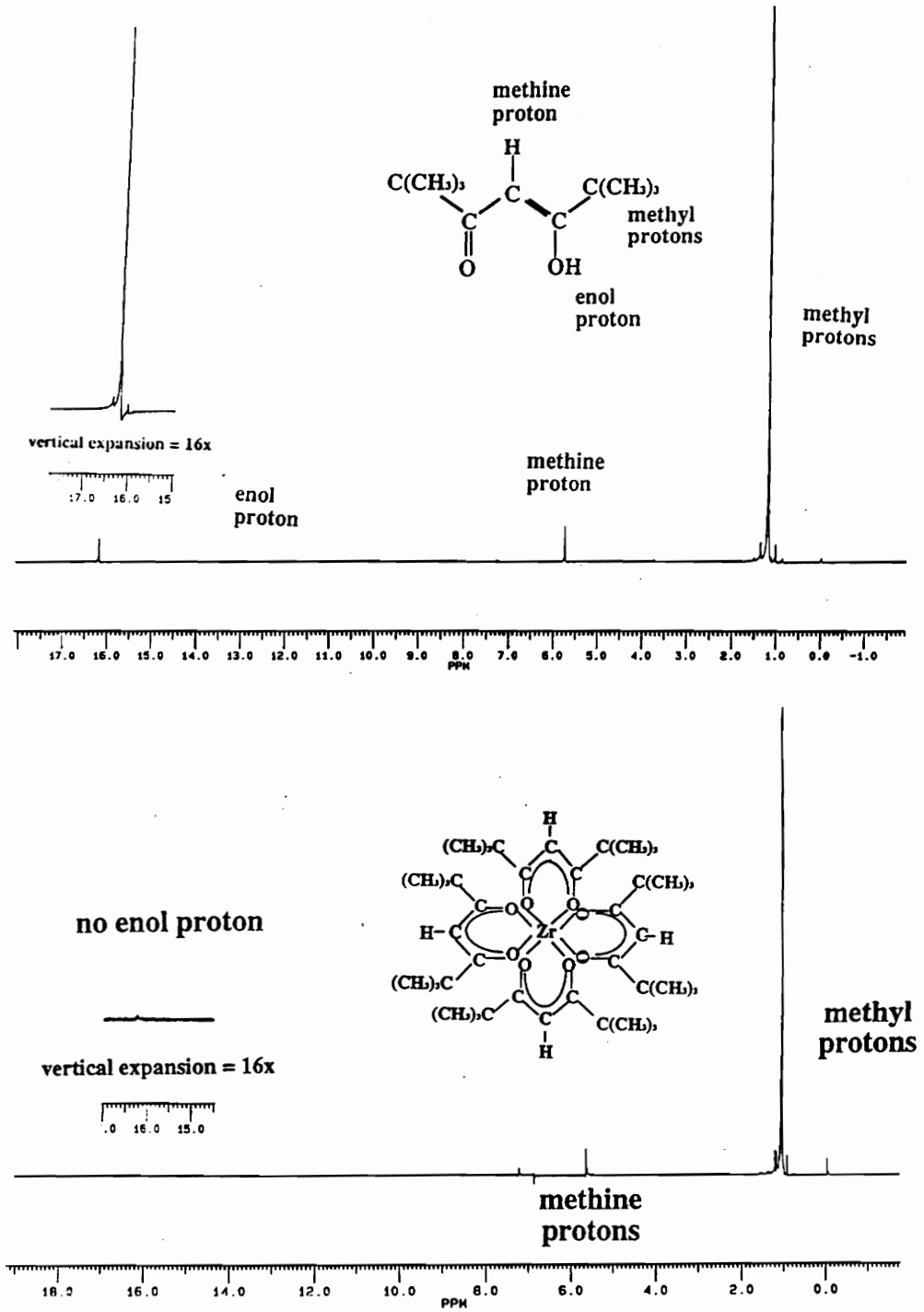

Figure 2.5 Proton NMR spectra of H-thd and $Zr(thd)_4$

elemental analyses were done by Atlantic Microlabs; *calculated:* 64.16% carbon, 9.23 % hydrogen. *found:* 63.95% carbon, 9.15% hydrogen.

2.2.1.2.2 Lead β-diketonate Synthesis

Synthesis of lead bis-heptafluorodimethyloctadione [$Pb(fod)_2$] was originally attempted using methods reported by Sievers and Connolly [11] and Belcher et al. [12]. The synthesis reported by Sievers and Connolly involves refluxing heptafluorodimethyloctadione (H-fod) and diethyl ether with powdered lead metal. However, in our experiment, the lead metal "sintered" very rapidly, thus greatly decreasing the surface area, and consequently decreasing the reactivity. No reaction product was obtained from this method. The method reported by Belcher involved vigorous mixing of aqueous lead acetate with an organic solution of ether and H-fod, extracting the $Pb(fod)_2$ product into the ether phase, and crystallizing at 0 °C. Due to the extreme solubility of $Pb(fod)_2$ in the presence of nonbonded H-fod ligand, crystallization of the $Pb(fod)_2$ from the ether phase was very difficult. Although the product was probably present in the ether phase, it was never isolated.

In response to this difficulty with $Pb(fod)_2$ crystallization, a novel synthesis method for lead β-diketonates was developed. The prototype synthesis was designed to be neat and stoichiometric, in attempt to easily isolate the $Pb(fod)_2$ product. The general reaction for the novel lead β-diketonate synthesis is:

$$PbO + 2H\text{-}L \text{ ----------> } Pb(L)_2 + H_2O \quad (2.3)$$

where H-L is the protonated β-diketonate ligand. Ultrasonic energy rather than heating was employed to implement this reaction. Ultrasonic energy facilitates reactions by a process

called "cavitation", which involves the formation and collapse of cavities to produce shock waves in the reaction medium. This process assists the reaction by dispersing the PbO powder, and possibly producing activated free radicals.[13]

The novel lead β-diketonate reaction initially reported for the synthesis of $Pb(fod)_2$ [14,15] is as follows. Ten ml pentane and six ml heptafluorodimethyloctadione [H-fod] (Aldrich catalog # 17,516-1, 98% purity) (26 mmol) were combined in a 50 ml flask, which was immersed in a Branson 2200 ultrasonic bath. Two grams PbO (10 mmol) was added slowly, 0.4 grams at a time. As the reaction proceeded, the PbO disappeared, and a yellow, oily layer and a water layer were formed. The yellow layer contained nonreacted H-fod, $Pb(fod)_2$ and pentane. The product mixture was filtered to remove any remaining PbO. The flask containing the mixture of $Pb(fod)_2$, H-fod, water and pentane was equipped with a distilling head. Freeze-thaw pump cycles (described in $Zr(thd)_4$ synthesis) were applied to implement distillation at reduced temperature. The product mixture was heated in vacuo (0.01 torr) at 50 °C for 24 hours in order to remove water, excess H-fod and pentane.

The product of the reaction is a pale yellow powder with a melting point of 76 °C. Reported melting temperatures of $Pb(fod)_2$ include 72 °C [9], 74 - 75.1 °C [11], and 74 °C [12]. Yields from PbO ranged from 90 - 98 %. Since $Pb(fod)_2$ was not recrystallized from a solvent during the purification process, the yields were mainly a function of the extent of reaction of the PbO, rather than the efficiency of the crystallization. The absence of any excess, nonbonded ligand was confirmed by proton nuclear magnetic resonance spectroscopy. The broad enol peak of H-fod at 15.0 ppm was not found in the final product (figure 2.6). Additionally, the methyl and methine peaks of the ligand complexing

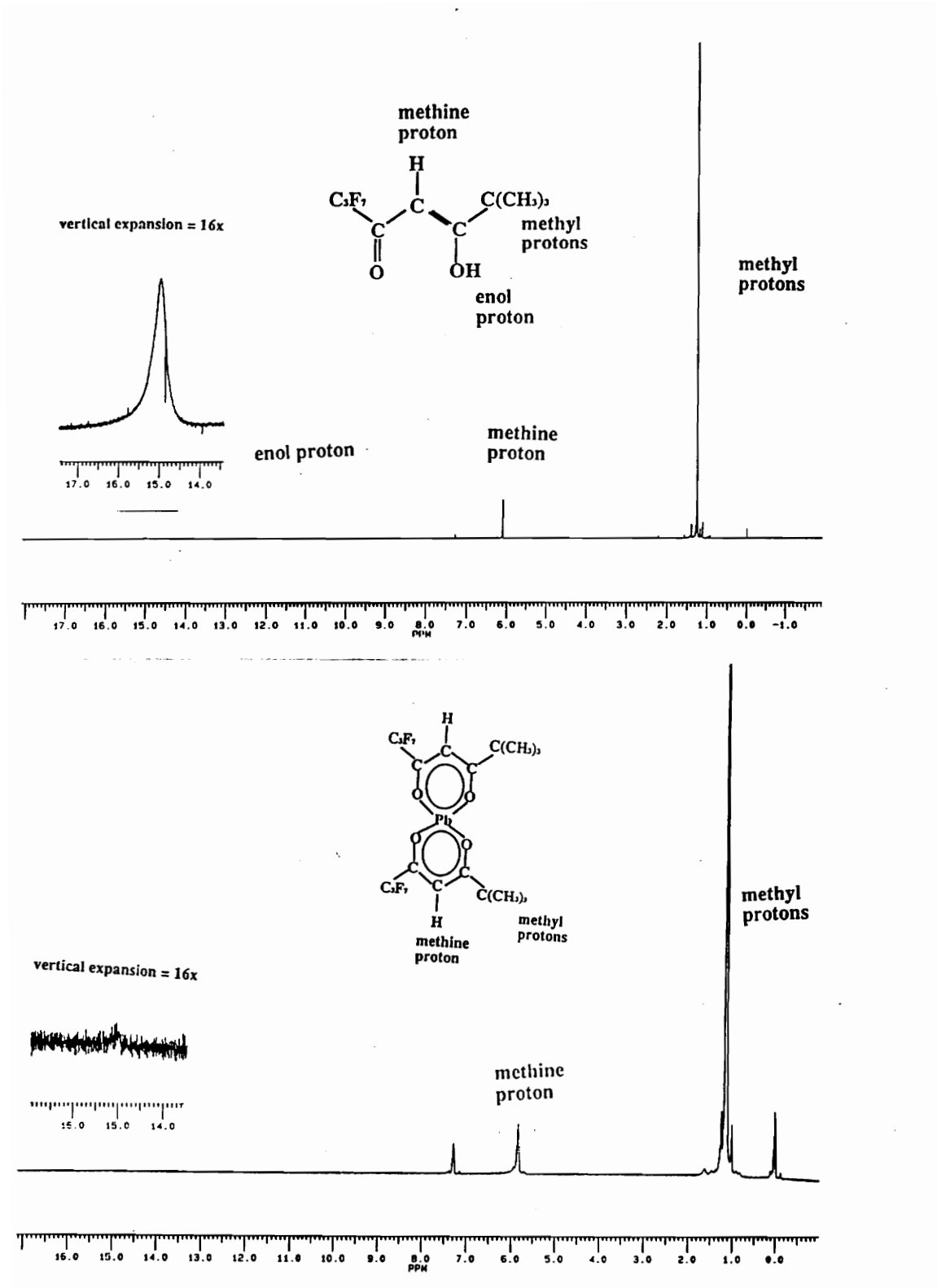

Figure 2.6 Proton NMR spectra of H-fod and Pb(fod)2

the Pb-metal center were located at 1.1 ppm and 5.8 ppm, respectively. These peaks are shifted upfield from the nonbonded ligand positions of 1.2 ppm and 6.0 ppm, respectively. The absence of the methyl peak at 1.2 ppm and methine peak at 6.0 ppm suggests the lack of excess, nonbonded ligand. Carbon and hydrogen elemental analyses were done by Atlantic Microlabs; *calculated:* 30.11% carbon, 2.51 hydrogen. *found:* 29.26% carbon, 2.40 % hydrogen.

Although the ultrasound bath synthesis worked satisfactorily, several unfavorable effects had to be continuously corrected, which created problems with potential contamination of the experiment, inconsistent results, and the need for constant monitoring of the experiment. For instance, PbO stuck to the sides of the reaction flask rather than dispersing throughout the reaction medium. Therefore, it was necessary to periodically agitate the reactants with a spatula. Additionally, the water in the ultrasound bath had to be changed several times during the reaction. The water was warmed approximately 10 °C over the course of the experiment, which decreases the efficiency of the cavitation effect [13]. Consequently, the ultrasonic reaction procedure was modified for ease of reaction and efficiency for the synthesis of lead bis-tetramethylheptadione [$Pb(thd)_2$]. Reasons for optimizing the $Pb(thd)_2$ synthesis rather than the $Pb(fod)_2$ synthesis include: 1) $Pb(thd)_2$ is more easily purified than $Pb(fod)_2$, thus facilitating the ease of reproducibility, and 2) $Pb(thd)_2$ proved to be a more useful precursor for chemical vapor deposition of lead oxide (discussed later).

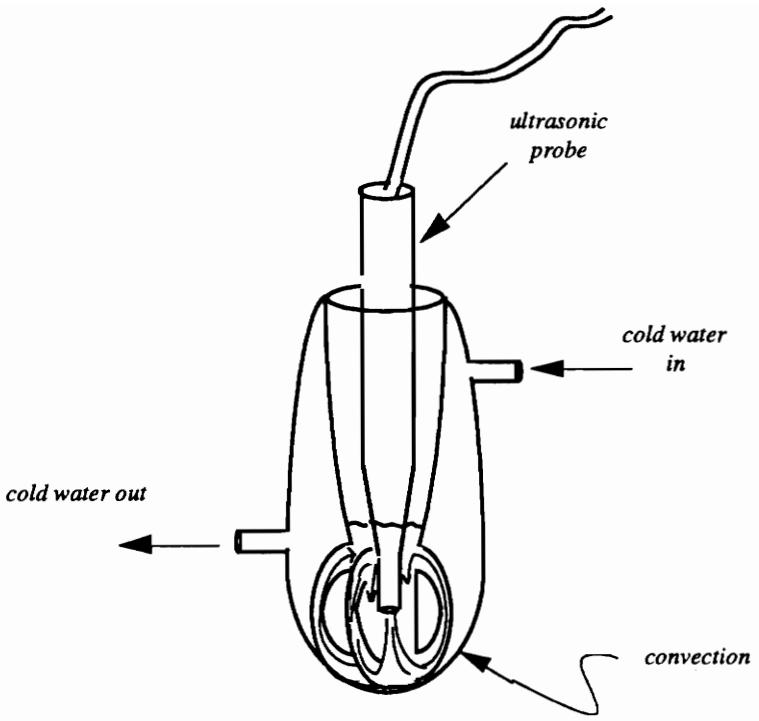

Figure 2.7 Lead precursor synthesis apparatus

A Virtis Virsonic 475 power supply with a 1/2 inch probe convertor was used, rather than a bath, as the ultrasonic source for the optimized reaction. The use of a probe convertor allowed for more efficient delivery of ultrasonic energy by direct immersion of the probe tip into the reaction medium. Another advantage this system provided which the bath did not provide is adjustable energy output (this feature is especially valuable when working with exceptionally large or small reaction media). A reaction flask was designed to optimize the the delivery of the ultrasound energy to the reaction (figure 2.7). The cooling jacket keeps the reaction at the temperature of cold tap water (7-10 °C), and the side arms implement efficient cooling via increased surface area. The side arms also create continuous convection, which enhances the reaction by effectively dispersing solid

reactants (lead oxide). The volume of the tapered portion of the reaction flask in which the reaction takes place is approximately 50 ml, not including the volume occupied by the probe tip. Therefore, the reaction medium should be approximately 50 ml.

The $Pb(thd)_2$ synthesis reaction is as follows. Tetramethylheptadione [H-thd] (28ml, 136 mmol) and 20 ml toluene were combined in the reaction flask. With the power of the ultrasound operating at 50%, lead (II) oxide (10 g, 45 mmol) was added slowly (2 grams at a time) to the toluene/H-thd mixture. Each 2 gram portion of PbO was added as the previous portion completely reacted (indicated visually by disappearance of orange, insoluble PbO powder). After the reaction is complete, the products were filtered to remove any nonreacted lead oxide. Freeze-thaw pump cycles were applied to implement distillation of the excess H-thd and toluene at room temperature (see section 2.2.1.1). The $Pb(thd)_2$ product was then recrystallized from toluene 3-4 times, or until no yellow color is apparent. Solubility of $Pb(thd)_2$ in toluene is 1g $Pb(thd)_2$ per 3-5 ml toluene, and crystallization was executed in an ice water bath (0-5 °C).

The product is a white crystalline solid of melting point 129 °C. Purity of $Pb(thd)_2$ was confirmed by proton NMR spectrometry and elemental analysis. Figure 2.8 shows proton NMR spectra of H-thd and $Pb(thd)_2$. The enol peak of H-thd at 16.1 ppm was not found in the final product. Additionally, the methyl and methine peaks of the ligand complexing the Pb-metal center are located at 1.10 ppm and 5.5 ppm, respectively. The methyl peak is shifted upfield from the H-thd position of 1.12 ppm, and the methine peak is shifted upfield from the H-thd position of 5.7 ppm. The absence of the methyl peak at 1.12 ppm also suggested the lack of excess, nonbonded ligand. Carbon and hydrogen elemental analyses were done by Atlantic Microlabs; *calculated:* 45.3 % carbon, 6.5 % hydrogen. *found:* 45.5 % carbon, 6.5 % hydrogen.

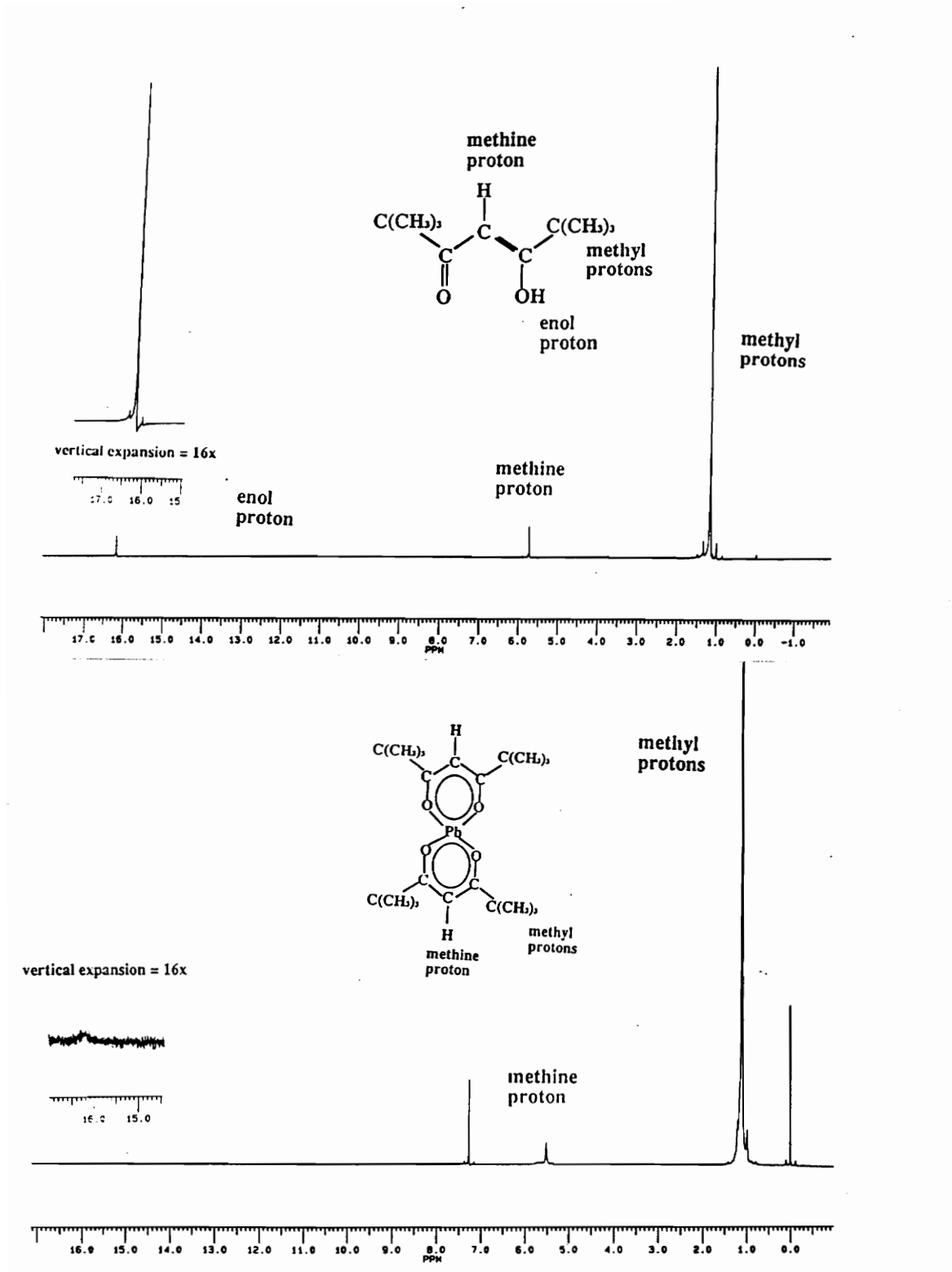

Figure 2.8 Proton NMR spectra of H-thd and Pb(thd)2

2.2.2 Volatility and Thermal Stability Experiments

Isothermal gravimetric experiments (TGA) were carried out in order to examine the volatility and thermal stability of $Zr(thd)_4$, $Pb(thd)_2$ and $Pb(fod)_2$ over a range of vaporization temperatures. Temperatures for the $Pb(thd)_2$ experiments ranged from 80-200 °C, at 10-20 °C increments, and $Pb(fod)_2$ experiments were carried out at 80-180 °C, at 20 °C increments. Experiments were executed at 10 °C increments near the $Pb(thd)_2$ melting point (129 °C), in order to determine the change in volatility behavior around this temperature. The $Zr(thd)_4$ thermogravimetric experiments were carried out at significantly higher temperatures; 180-260 °C at 20 °C intervals. Isothermal gravimetric analysis experiments were executed on a Perkin-Elmer TGS-2 thermogravimetric system. Precursor sample size was kept constant at 2 milligrams for all TGA experiments so that the evaporation surface area was kept constant. Dry nitrogen was chosen as the purge gas to eliminate reactions of the precursor with oxygen or water, which would interfere with vaporization rate of the sample. The N_2 purge rate was kept constant at 25 ml/min. The consistency of purge rate, and the consistency of the sample size were necessary to convert the TGA weight loss at different temperatures to precursor vapor pressures at these temperatures. This point will be discussed in detail in section 2.3.1.1.

Thermogravimetric experiments of the lead precursors above 120 °C exhibited some decomposition, as well as vaporization. Evidence for this occurrence was a break in slope of the TGA curve (% weight/time), which occurred when 30-85% of original sample weight had evaporated from the sample pan. Additionally, decomposition products, which were darker in color than the original precursors were visible in the sample pan at the conclusion of these experiments.

Because the remaining, decomposed precursor was too little to retrieve for analysis, the experiments were replicated on a larger scale, and the decomposed product was

collected for analysis. Replicated experiments were carried out in a 25 ml round bottom flask, with 250 milligram samples of $Pb(fod)_2$ and $Pb(thd)_2$. The flask containing the precursor was submerged in a 140 °C oil bath, and the flask was purged with dry nitrogen at a rate of 25 ml/min. After several hours, a fraction of the sample had sublimed and condensed on the cool part of the flask which was not submerged in the oil bath, and the decomposed precursor remained in the bottom of the flask.

This decomposed sample was retrieved for chemical ionization mass spectrometry analysis. Analyses were carried out on a VG 7070 mass spectrometer. Samples were scanned from 200-1500 mass units. Ultramark 1621 was used for high mass calibration (above 750 mass units), and perfluorokerosene (PFK) was used for the low mass calibration (standards obtained from PCR Incorporated; Gainsville FL). Isobutane reagent gas was used as the chemical ionization source. Complete mass spectra are compiled in appendix D.

2.2.3 Decomposition Experiments

Thermal decomposition experiments of the metal β-diketonate precursor compounds [$Zr(thd)_4$, $Pb(fod)_2$, and $Pb(thd)_2$] were carried out in sealed quartz tubes under an oxygen atmosphere. Table 2.2 summarizes the parameters for the decomposition experiments. Variations of the reactor volume and oxygen pressure was necessary in order to accommodate specific logistical problems of individual precursors. For instance, a larger cylinder volume was used for the $Pb(fod)_2$ experiments to withstand the extra pressure generated by the water (discussed later) added to these decomposition experiments. For the same reason, the oxygen pressure under which the $Pb(fod)_2$ experiments were carried out was less than a full atmosphere. Oxygen was present in excess (column 4, table 2.2) so that all of the precursor present, in principle, could be oxidized. Equations 2.4 - 2.6 show

the possible reaction products. It is assumed that formation of metal oxides is thermodynamically favored over formation of ligand oxidation products.

Table 2.2 Conditions for decomposition experiments

precursor	volume of cylinder	amount of precursor	amount of O2	**excess O2
*Pb (fod) 2	0.14 L	0.6 g (0.6mmol)	0.7 (4.0 mmol)	× 6.7
Pb (thd) 2	0.04 L	0.1 g (0.17 mmol)	1.2 atm (2.0 mmol)	× 23.5
Zr (thd) 4	0.04 L	0.1 g (0.12 mmol)	1.2 atm (2.0 mmol)	× 16.7

* explanation of further experimental parameters in text

**explanation in text

$$2\,Pb(C_{10}F_7H_{10}O_2)_2 + H_2O + O_2 \xrightarrow{\Delta} 2\,PbO + C_{10}F_7H_{11}O_2 + \text{(ligand decomposition products)} \quad (2.4)$$

$$2\,Pb(C_{11}H_{19}O_2)_2 + O_2 \xrightarrow{\Delta} 2\,PbO + C_{11}H_{20}O_2 + \text{(ligand decomposition products)} \quad (2.5)$$

$$Zr(C_{11}H_{19}O_2)_4 + O_2 \xrightarrow{\Delta} ZrO_2 + C_{11}H_{20}O_2 + \text{(ligand decomposition products)} \quad (2.6)$$

The excess oxygen was necessary to ensure the rates of metal oxide formation would be independent of amount of oxygen (i.e. first order reaction). In order to prevent the formation of metal fluorides[16] , 0.2 ml (5X stoichiometric excess) water was added to each $Pb(fod)_2$ decomposition experiment. Presence of water ties up the fluorine in H-F bonds, so that metal fluorides do not form so easily. Possible ligand decomposition products mentioned in equations 2.4-2.6 include CO_2, H_2O, CH_4. Additional ligand decomposition products of $Pb(fod)_2$ include CF_4 and HF.

The apparatus used for sealing the quartz tubes is illustrated in figure 2.9. The cylinder containing a silicon wafer (discussed later), the weighed precursor sample (and water, in the case of $Pb(fod)_2$) was evacuated to 0.3 - 0.6 torr, and backfilled to the appropriate pressure with pure oxygen. This process was repeated three times. The quartz cylinder was then submerged in liquid nitrogen to create a partial vacuum in the cylinder . A gas-oxygen flame was used to seal the neck of the cylinder. The cylinders were then put in a large box furnace at the designated temperature for the designated time.

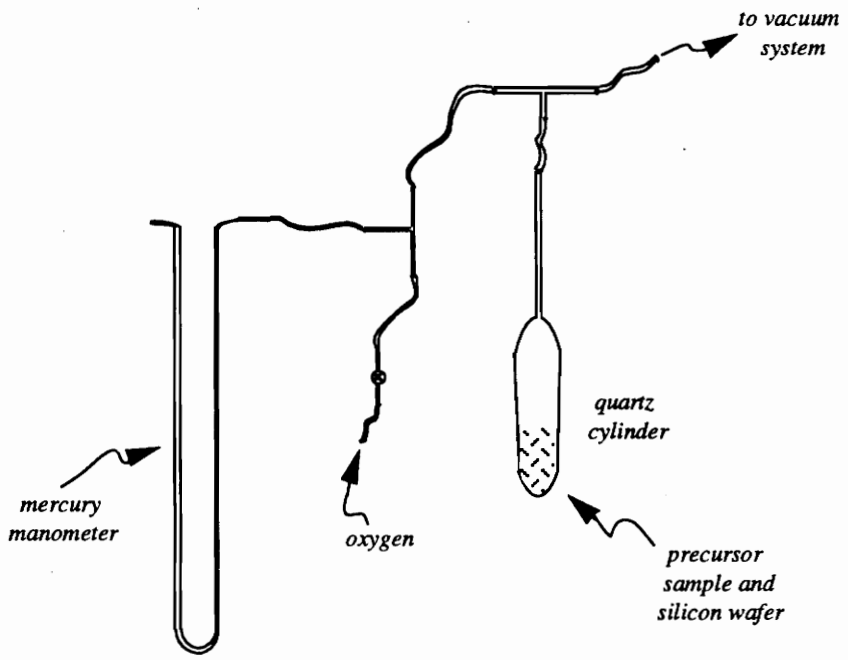

Figure 2.9 Tube sealing apparatus

After the heating experiments, each tube was broken, and the silicon wafer was retrieved for infrared measurements of the decomposition products. Since the solid decomposition products were randomly distributed over the area of the quartz tube walls, the silicon substrate had a coating of representative decomposition products and reactants, including nondecomposed precursor, metal oxide product, and species intermediate between precursor and metal oxide. Water was also present , especially in the decomposition experiments carried out at the higher temperatures (the organic ligands combust to CO_2 and water at higher decomposition temperatures). Therefore, substrates were dried in air before carrying out infrared analyses on the remaining condensed phase decomposition products.

Infrared measurements of the decomposition products were executed on a Bomem DA3.02 FTIR spectrometer with a resolution of 0.5 cm^{-1}. Measurements were taken in

both the 400-5000 wavenumber (cm^{-1}) range, and the 125-700 wavenumber range. The instrument was equipped with a globar source, KBr beam splitter and DTGS detector for measurements in the region of wavenumbers ranging from 400-5000 cm^{-1}. A globar source, 3 μm pellicle mylar beam splitter and DTGS detector was used for measurements in the region of 125 - 700 wavenumbers. Chemical ionization mass spectrometry was also used to examine some of the decomposition products that were obtained at lower temperatures. Experimental procedure and instrumentation for the mass spectrometry is described in Section 2.2.2.

2.3 Results and Discussion

2.3.1 Volatility and Thermal Stability

The isothermal gravimetric experiments were executed in order to obtain an understanding of precursor behavior at vaporization temperatures. The thermograms of $Pb(fod)_2$, $Pb(thd)_2$, and $Zr(thd)_4$ are shown in Figures 2.10, 2.11, and 2.12, respectively. At all vaporization temperatures for the three precursors, the initial %weight loss/time slope is constant, and the slopes increase with increasing vaporization temperature. The $Zr(thd)_4$ 240 °C and 260 °C isotherms show complete evaporation of the precursor sample within 37 and 15 minutes, respectively. The $Zr(thd)_4$ 180, 200, and 220 °C isotherms show that complete evaporation of the precursor sample does not occur within 60 minutes, but the rate of weight loss is constant. The isotherms of $Pb(fod)_2$ and $Pb(thd)_2$ suggest somewhat different behavior of these precursors at vaporization temperatures. Again, initial vaporization rate is constant for all isotherms, but there is a subsequent break in the %weight/time slope of the of the isotherms above 120 °C for both $Pb(fod)_2$ and $Pb(thd)_2$. After the break in slope of these isotherms, there is a second constant vaporization rate,

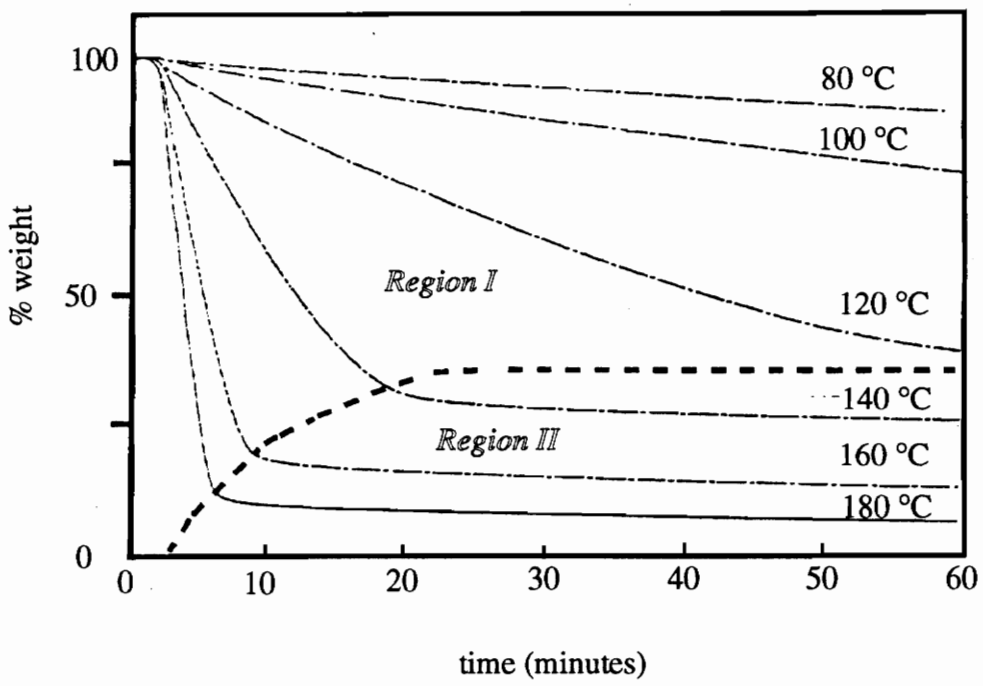

Figure 2.10 Pb(fod)2 isotherms

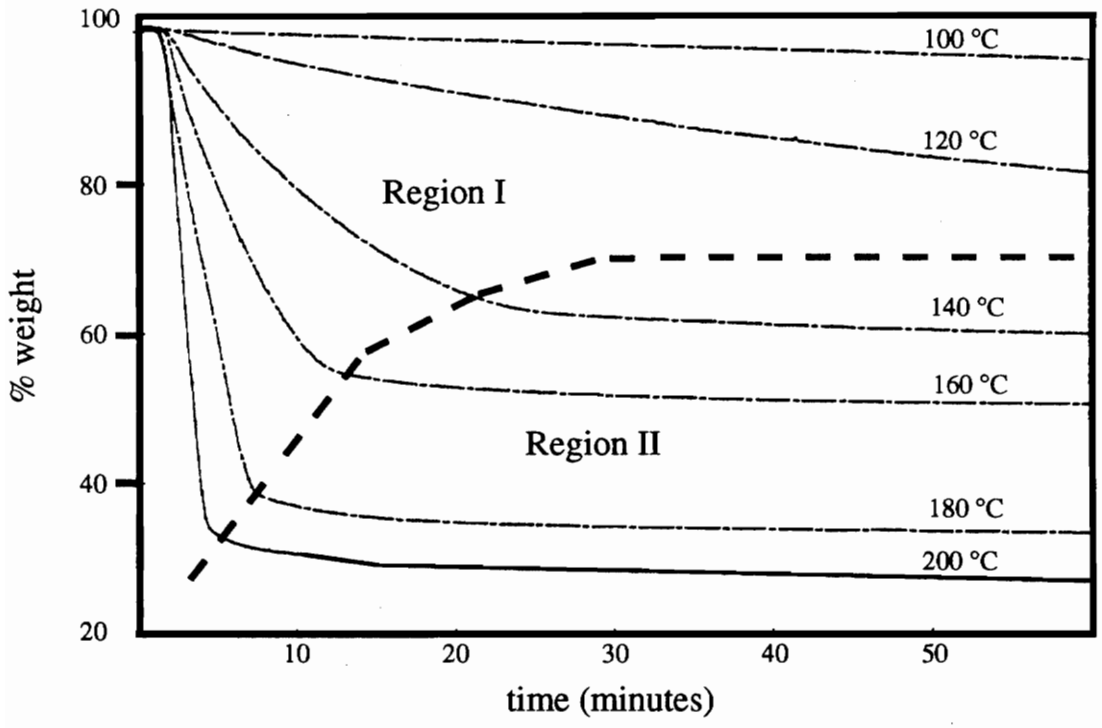

Figure 2.11 $Pb(thd)_2$ isotherms

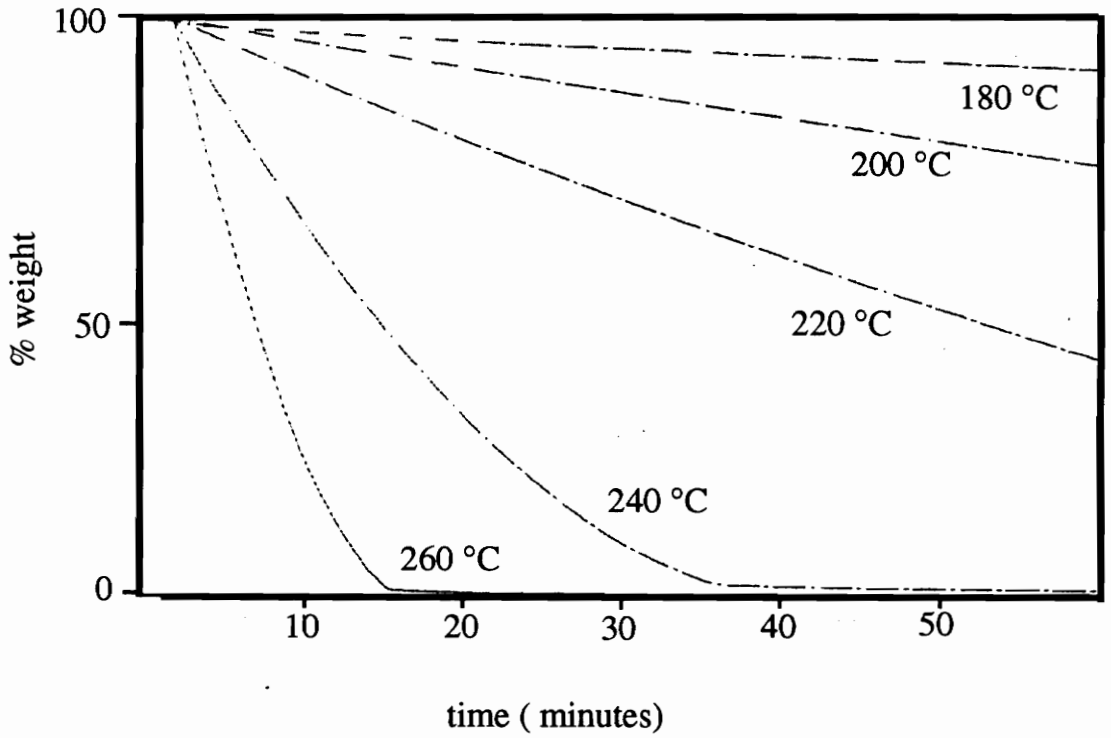

Figure 2.12 $Zr(thd)_4$ isotherms

much less than the initial rate. The break in slope occurs when decomposition of the precursor molecule overtakes evaporation of the precursor molecule as the rate controlling mechanism of weight loss. It is assumed that decomposition of the precursor is controlling the rate of weight loss after the break in slope. This assumption is presently made because the material remaining in the sample pan is altered (darkened) in appearance from the original precursor sample.

For the sake of discussion, the lead precursor thermograms have been subdivided into areas of thermal stability of the precursor and thermal instability of the precursor, respectively labeled Region I and Region II. Region I also refers to the entire $Zr(thd)_4$ thermogram, because the precursor appears to be thermally stable over the range of vaporization temperatures and times. Region I is further analyzed by converting rate of weight loss to precursor vapor pressure over the range of vaporization temperatures. Discussions of region II will include conjectured decomposition mechanisms, possible causes for these reactions, and potential means of preventing this thermal decomposition at vaporization temperatures.

2.3.1.1 Region I

In order to calculate precursor vapor pressure from the %weight loss/time slope, the rate determining step of vaporization must be defined. Rate of vaporization is affected by three subsequent processes: 1) "escape" of the precursor molecule into the gas phase from the solid or liquid precursor surface 2) diffusion of the precursor through the "effective boundary layer" (defined later) above the liquid/vapor or solid/vapor interface 3) removal of the precursor from the boundary layer by the purge gas.

The precursor molecule must overcome intermolecular attractive forces in order to "escape" the solid/liquid surface. The metal β-diketonate molecules are losely held together

in the condensed phase by van der Waals forces, which increase with increased metal diameter, and decreased ligand bulkiness (discussed in detail in section 2.1).[3] Generally, van der Waals forces of a solid does not make up a significant portion of the overall crystal lattice energy. Therefore, the escape of the metal β-diketonate molecule from the solid surface, or overcoming the van der Waals forces, is most likely not the rate controlling step of vaporization.

The rate controlling step of vaporization of the precursor molecule is now limited to either 1) removal of the vaporous molecule above the effective boundary layer by the purge gas, or 2) diffusion of the vaporous molecule through the effective boundary layer. The thermogravimetric experiments can be controlled so that diffusion of the precursor molecule through the effective boundary layer is the rate controlling step. If the rate controlling step were removal of the evaporated molecule above the effective boundary layer by the nitrogen purge, then increase of purge rate should increase the rate of weight loss. This experiment was carried out for several temperatures for each precursor. Doubling the nitrogen purge rate from 25 ml/min to 50 ml/min resulted in no change in rate of weight loss. Therefore, precursor vapor pressure can be calculated from the TGA weight loss data with use of gas diffusion laws, assuming diffusion of the precursor molecule through the effective boundary layer is the rate-determining step.

The relationship between the rate of precursor weight loss and the system parameters which control the diffusion of the precursor is:

$$\Delta m \propto J = DC(T)/d \qquad (2.7)$$

The rate of precursor weight loss is Δm, J is the diffusional flux, D (cm^2/sec) is the diffusion coefficient of the precursor vapor in the system, and C is the concentration of the precursor vapor in the saturated carrier gas.

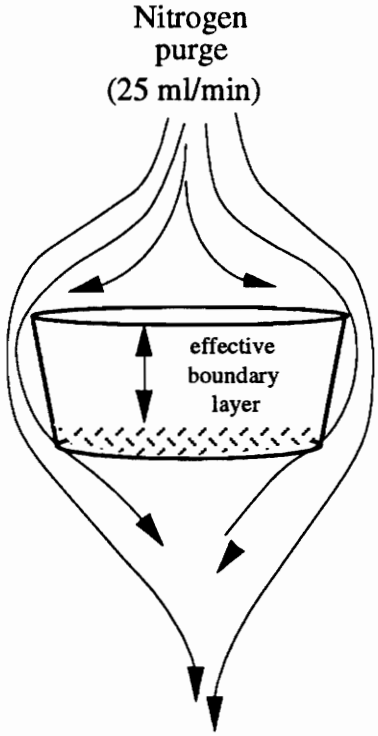

Figure 2.13 Flow of purge gas over TGA sample pan

Figure 2.13 schematically demonstrates the "effective boundary layer (the d term). The precursor sample pan of the TGA instrument hangs in a vertical, quartz tube furnace in the laminar flow path of the purge gas. The purge gas flows perpendicular to the surface of the sample, deflects around the sample pan, and exits the furnace below the pan. Within the confines of the pan sides, there is no effective flow of purge gas which can transport vaporized precursor molecules. The precursor molecules must diffuse up the height of the pan sides before the carrier gas removes them from the furnace. Therefore, the height of

the pan sides is defined as the diffusional length of the precursor, or the effective boundary layer thickness. [17]

Precursor vapor pressure can be calculated as a function of temperature from the TGA weight loss curves:

$$\Delta m / \Delta t = [MDP(T)/(RTd)]S \quad (2.8)$$

The rate of weight loss is $\Delta m/\Delta t$ (g/sec), which is extracted from the thermograms, M is molecular weight (g/mol) of the precursor, D is the diffusion coefficient (cm^2/sec), P(T) is precursor vapor pressure (atm), R is the gas constant (atm cm^3/K mol), T is temperature (K) of the isothermic experiment, d is diffusional length (cm) and S is area of the precursor/gas interface. The diffusional coefficient can be calculated from the following equation:

$$D = kT[(1 + \lambda/l)^{-1} + 2.25\lambda/l](6\pi\eta l)^{-1} \quad (2.9)$$

Boltzmann's constant is k (J/K), T is temperature (K), λ is mean free path of the carrier gas molecule (cm), l is diameter of the diffusing precursor molecule (cm), and η is dynamic viscosity of the carrier gas.

The %weight/time slopes of the isotherms must be converted to Δmass/ Δtime, which is presented in table 2.3. Other parameter values which are necessary to calculate precursor vapor pressure are presented in table 2.4. The diameters (l) of the diffusing precursor molecules were approximated from single crystal X-ray data in the literature. The compound most similar to $Zr(thd)_4$ for which X-ray data was reported is $Zr(acac)_4$.[18] No lead β-diketonate X-ray data was available; therefore $Sn(acac)_2$ X-ray data was used to

Table 2.3 $\Delta m/\Delta t$ of $Pb(thd)_2$, $Pb(fod)_2$ and $Zr(thd)_4$

	Precursor weight loss / time (mg/min)		
Temperature (°C)	$Pb(thd)_2$	$Pb(fod)_2$	$Zr(thd)_4$
80	0.000301	0.00243	
100	0.00149	0.00605	
110	0.00366		
120	0.00688	0.0186	
140	0.0389	0.0835	
160	0.0966	0.232	
180	0.227	0.573	0.00248
200	0.502		0.00940
220			0.0207
240			0.0726
260			0.154

Table 2.4 Parameters for diffusion controlled vapor pressure calculations

	$Pb(thd)_2$	$Pb(fod)_2$	$Zr(thd)_4$
approximate diameter of molecule (angstroms) (l)	7.15	7.15	6.90
mol weight (g/mol)	575	797	823
diffusion coefficient (cm^2/sec) (D)	1.25	1.25	1.29
dynamic viscosity of carrier gas (η)	2.0×10^{-4} g/cm sec		
mean free path of carrier gas (λ)	7.5×10^{-6} cm		
area of precursor evaporation surface (S)	0.126 cm		
diffusion length [boundary layer thickness] (d)	0.19 cm		

obtain the approximate bond angles and lengths.[19] The diameter of $Pb(fod)_2$ and $Pb(thd)_2$ were assigned the same value; i.e. the different sizes of the R-groups were ignored. Mean free path (λ) of the purge gas was calculated using ideal gas assumptions, and the dynamic viscosity (η) was calculated using Lennard-Jones parameters.[20] The area of the precursor/gas interface (S) was kept approximately constant by using an equal sample size (2 mg) for each isothermic experiment. The precursor/gas surface area changes with evaporation of the precursor sample, which can be seen in the slight curvature of the slopes in figures 2.10-2.12. Therefore, the initial slope of $\Delta m/\Delta t$ was always chosen for the calculations.

Calculated vapor pressures plotted as a function of temperature (figure 2.14) reveal the logarithmic dependance on temperature. Vapor pressures range from approximately 0.2 - 600 millitorr for the three metal β-diketonates. This range of vapor pressures agrees well with the range of measured vapor pressures of transition metal β-diketonates reported by Wolf et al.[21] There is a discontinuity in slope at the $Pb(thd)_2$ melting point. This is not observed for the $Pb(fod)_2$ and Zr(thd)4 because they do not melt over the temperature ranges of the experiments ($Zr(thd)_4$ melts at 345 °C, and $Pb(fod)_2$ melts at 76 °C). From the Arrhenius dependence of the vapor pressure on vaporization temperature, enthalpy of vaporization was calculated:

$$\ln P = -\Delta H_{vap} / RT \qquad (2.10)$$

where $-\Delta H_{vap}/R$ is equal to the slope $\Delta(\ln P)/\Delta(1/T)$ of the Arrhenius plot (figure 2.15). The calculated enthalpies are listed in figure 2.15. These values are comparable to those reported of transition metal β-diketonates[22] and rare earth metal β-diketonates[22]. Again,

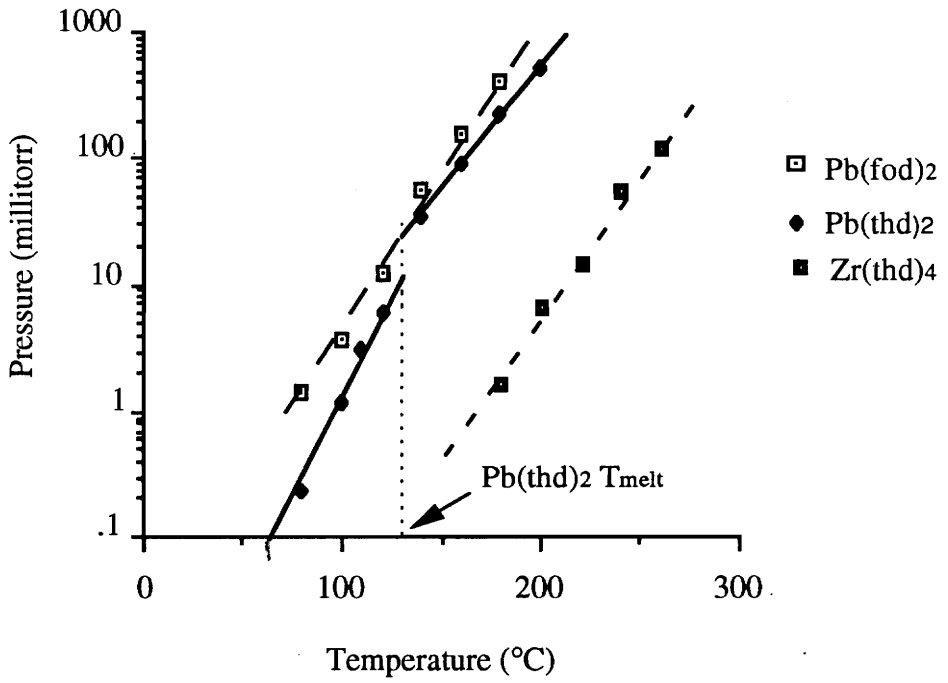

Figure 2.14 Vapor pressure of precursors as a function of temperature

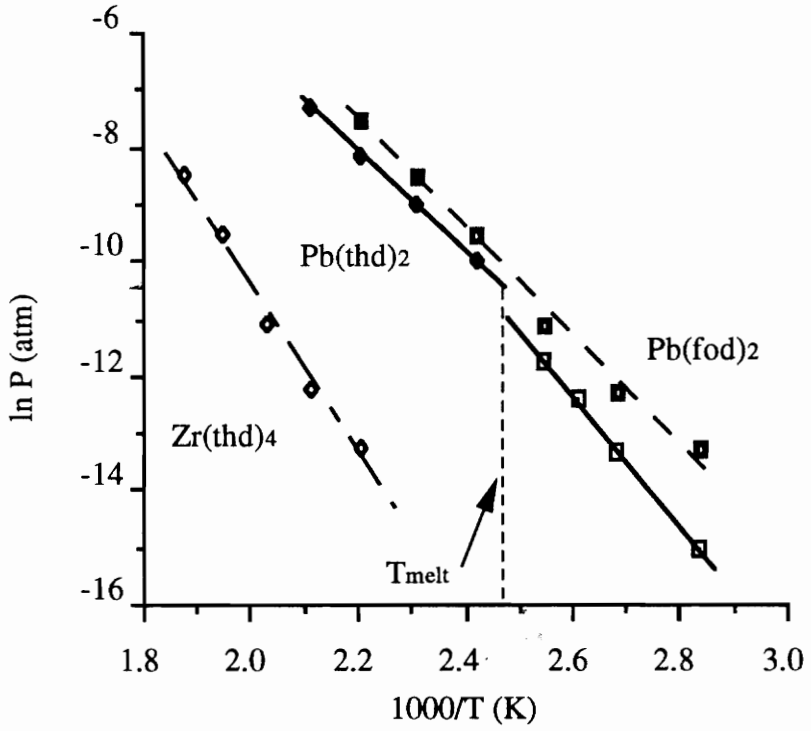

ln (P) = -ΔHvap/RT	
▫ Pb(thd)2 (below Tmelt)	ΔHvap = 95.0 KJ/mol
◆ Pb(thd)2 (above Tmelt)	ΔHvap = 73.1 KJ/mol
■ Pb(fod)2	ΔHvap = 78.8 KJ/mol
● Zr(thd)4	ΔHvap = 107.4 KJ/mol

Figure 2.15 Arrhenius plot of precursor vapor pressure

$Pb(thd)_2$ exhibits a break in slope at 129 °C, and two enthalpies of vaporization are calculated for $Pb(thd)_2$.

2.3.1.2 Region II

In region I, vaporization rate increased with increasing vaporization temperature for $Pb(fod)_2$, $Pb(thd)_2$ and $Zr(thd)_4$. In region II, the vaporization rate of both $Pb(fod)_2$ and $Pb(thd)_2$ decreases with increasing temperature of the isothermal experiment (figure 2.16). Additionally, the rate of vaporization decreases as much as 4 orders of magnitude from region I to region II of an isotherm. The rates of vaporization for $Pb(fod)_2$ and $Pb(thd)_2$ at 140, 160, and 180 °C are compared for region I and region II in table 2.5.

Table 2.5 Comparison of vaporization rates in region I and II

precursor		rate of weight loss (mg/min)		
		140 °C	160 °C	180 °C
$Pb(fod)_2$	Region I	0.0835	0.232	0.537
	Region II	0.0011	0.00075	0.000089
$Pb(thd)_2$	Region I	0.0389	0.0966	0.227
	Region II	0.0019	0.0012	0.00079

The decrease of lead precursor volatility with increasing temperature suggests that the vaporization rate in region II may be controlled by intermolecular association reactions which decrease the vaporization rate. Additionally, in order to account for the decrease in volatility with increase in temperature, these intermolecular reactions must increase in rate with increasing temperature. It is assumed that the volatility-decreasing reactions involve

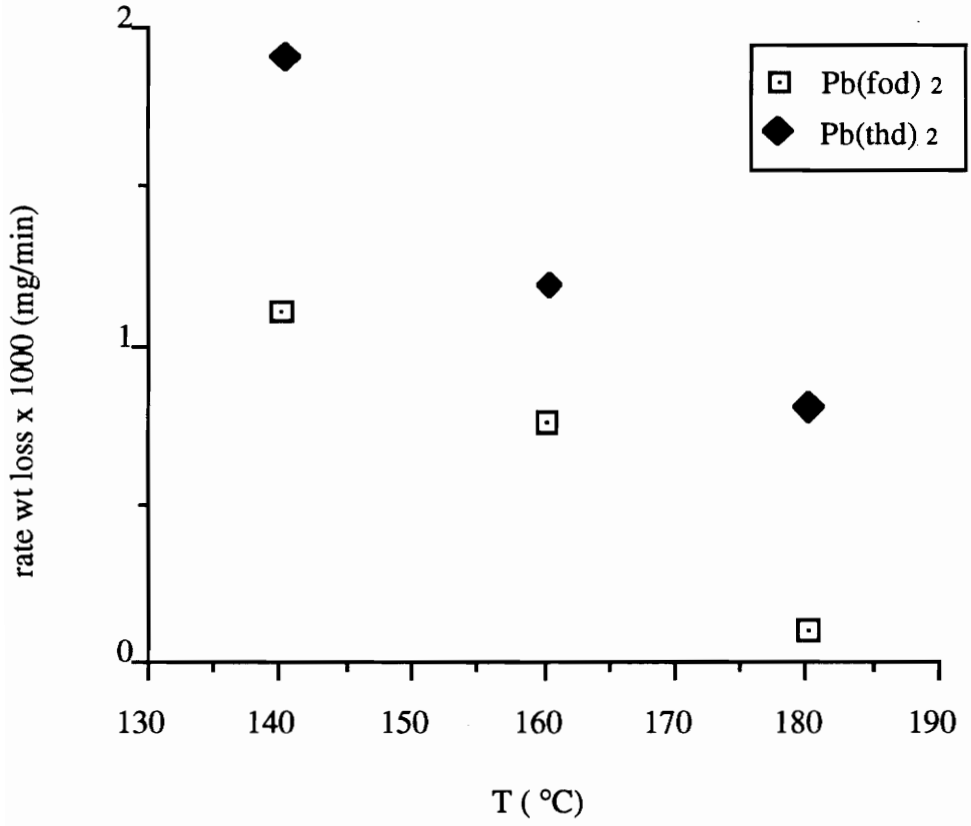

Figure 2.16 Rate of vaporization of lead β-diketonates in region II

only the precursor molecules, because the only other component present in the TGA experiments is inert, dry nitrogen purge gas. One possible rate controlling, intermolecular reaction is the formation of oligomeric complexes from monomeric molecules. In the case of this mechanism, reactions would decrease the volatility of the lead β-diketonates by decreasing the number of lighter, volatile monomers and increasing the number of heavier, less volatile oligomers.

Table 2.6
Species detected by mass spectrometry of: 1) lead precursors 2) decomposition products obtained by heating samples at 140 °C in N_2 purge.

Pb(fod)2				Pb(thd)2			
precursor		decomposition product (140 °C)		precursor		decomposition product (140 °C)	
specie	relative abundance	specie	relative abundance	specie	relative abundance	specie	relative abundance
Pb(fod)2	30%	Pb(fod)2	100%	Pb(thd)2	100%		
Pb(fod)	100%	Pb(fod)	100%	Pb(thd)	100%	Pb2(thd)3	100%
Pb(fod) - 2F	10%	Pb(fod)2 - 8F	45%	Pb(thd)2 -			
Pb(fod)2 -		Pb(fod)2 -		(t-butyl)	100%	Pb2(thd)3 -	70%
(t-butyl)	10%	(t-butyl)	10%	Pb2(thd)3	100%	(t-butyl) -	
Pb(fod)2 - 8F	20%	Pb2(fod)3	<5%	Pb3(thd)4 -		2(methyl)	
Pb2(fod)3	100%	(no daugter ion of		3(t-butyl)	<1%		
Pb2(fod)3 -		Pb2(fod)3 detectable)					
C3F7 - (t-butyl)	30%						
Pb2(fod)3 - 8F	10%						

In order to further examine the rate controlling, intermolecular processes of region II, the isothermal TGA experiments were replicated on a larger scale (discussed in detail in section 2.2.2), and mass spectrometry was used to compare the precursors to the products of decomposition at vaporization temperatures. Mass spectral data of 1) species which did not vaporize during the experiment (unsublimed fraction) , and 2) original synthesized and purified $Pb(fod)_2$ and $Pb(thd)_2$ are shown in table 2.6. The percent relative abundance

is scaled relative to the species in highest concentration. If several species are present in similar concentrations of the total sample, then they will appear as the same relative abundance. This is the case for the most abundant species (100% relative abundance) in the $Pb(fod)_2$ precursor sample, the heated $Pb(fod)_2$ sample, and the $Pb(thd)_2$ precursor sample.

The mass spectral data suggests that $Pb(thd)_2$ precursor also contains a significant amount of $Pb_2(thd)_3$, and $Pb(fod)_2$ also contains $Pb_2(fod)_3$. The portion of the thd-complexes remaining unvaporized after heating at 140 °C under a N_2 purge contains only $Pb_2(thd)_3$. Two possible conclusions concerning the disappearance of the $Pb(thd)_2$ monomer are proposed: 1) All the monomer vaporized out of the apparatus, leaving only $Pb_2(thd)_3$. 2) Some of the unvaporized monomer dimerized to form $Pb_2(thd)_3$. The TGA data supports the second conclusion. If the first conclusion were true, the rate of weight loss observed in region II would be controlled by the evaporation of $Pb_2(thd)_3$. If this evaporation is analogous to the evaporation rate of the monomeric specie (region I), then evaporation rate should increase with increasing isothermal temperature. However, evaporation rate decreases with increasing isothermal temperature in region II.

The mass spectral data of the fod-complexes suggests a different behavior upon prolonged heating. After heating in N_2 purge at 140 °C, less than 5% of the $Pb_2(fod)_3$ remains. Additionally, there is a higher concentration of unfragmented $Pb(fod)_2$ detected in the heated sample than in the precursor sample. However, most of the $Pb(fod)_2$ in the precursor sample is detected as daughter ions, whereas most of the $Pb(fod)_2$ in the heated sample is detected as a parent ion. Two models are proposed to explain this phenomena: 1) The $Pb_2(fod)_3$ is not thermally stable, and degrades to $Pb(fod)_2$ during heating. 2) Heating results in further oligomerization of the $Pb_2(fod)_3$ oligomer to produce complexes

which are not detectable within the mass range of the the mass spectrometer (< 2500 mass units) such as Pb_4fod_6 (2616 g/mol) or $Pb_5(fod)_6$ (2823 g/mol).

The first model is difficult to accept because the formation of $Pb(fod)_2$ from $Pb_2(fod)_3$ requires excess ligand, and the proton NMR analyses and carbon /hydrogen elemental analyses suggest there is not a significant amount of excess ligand (discussed in detail in section 2.2.1). Additionally, if more volatile $Pb(fod)_2$ were formed from less volatile $Pb_2(fod)_3$, then the rate of vaporization should increase, rather than decrease in region II.

Although there is a significantly higher concentration of $Pb(fod)_2$ parent ions present in the heated sample than the precursor sample, the relative abundances is important to note here that the fod-complexes become more fragmented than the thd-complexes from the chemical ionization process. This is a consequence of the electronegative nature of the fluorines in the fod ligand; fluorine withdraws delocalized π-electrons from the chelating ring, and bonds within the ring are subsequently weakened.[23] Therefore, the relative abundance of unfragmented $Pb(fod)_2$ species in the heated sample is anomalously high, compared to the relative abundance of $Pb(fod)_2$ in the precursor sample (i.e. a larger portion of the $Pb(fod)_2$ should be fragmented). This might suggest that the excess $Pb(fod)_2$ detected in the heated sample is actually a daughter ion of a higher weight oligomer, rather than a parent ion. More supporting evidence for higher weight oligomer formation of $Pb(fod)_2$ in region II (>2500 mass units) is apparent in table 2.5. In region I for temperatures 140, 160, and 180 °C, $Pb(fod)_2$ consistently has a higher vaporization rate than $Pb(fod)_2$. However, in region II, the vaporization rates of the $Pb(fod)_2$ isotherms are consistently lower than the vaporization rates of the $Pb(thd)_2$ isotherms. This evidence agrees well with the hypothesis that $Pb(fod)_2$ forms oligomers upon heating at higher vaporization temperatures, which are too heavy to be detectable by mass spectrometry techniques.

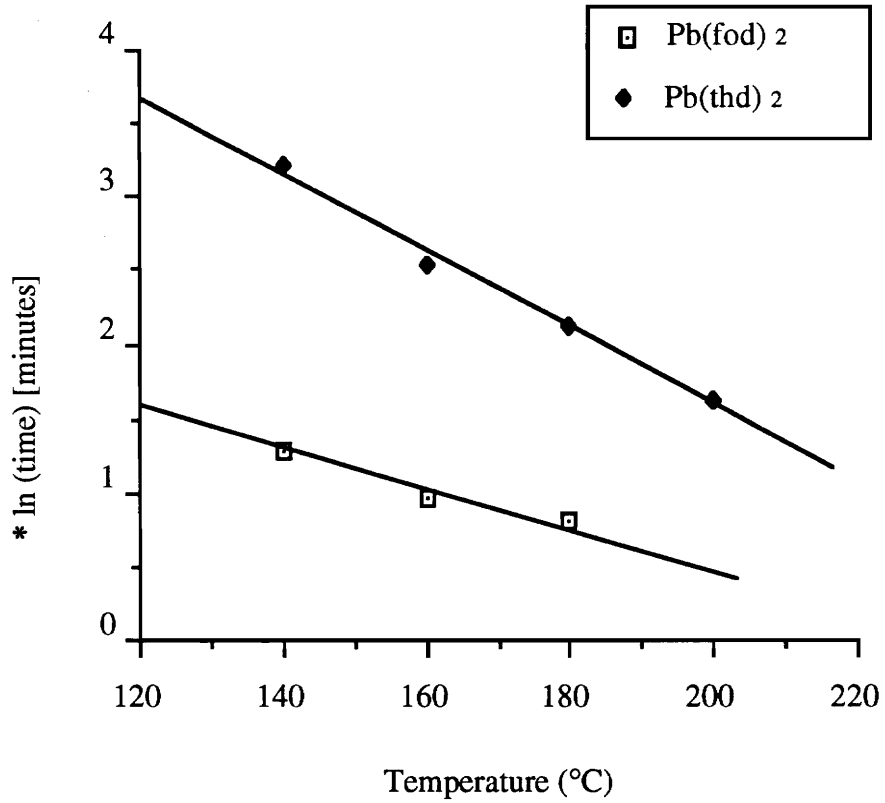

* duration of precursor stability before onset of oligomer formation (i.e. onset of region II)

Figure 2.17
Duration of lead precursor stability as a function of temperature

Another important feature of region II is the duration of lead precursor stability before onset of decomposition (i.e. break in slope) as a function of temperature. It is apparent in figures 2.10 and 2.11 that the higher the vaporization temperature, the earlier oligomer formation is initiated. Figure 2.17 reveals that the duration of precursor stability decreases logarithmically with linear increase in vaporization temperature. This relationship provides two branches of information. First, since the precursor stability is graphed linearly as a function of temperature, the relationship can be extrapolated over a whole range of temperatures. This provides practical information concerning how long a precursor can be heated before oligomer formation is initiated, and vapor pressure is significantly decreased. Second, the Arrhenius relationship between duration of precursor stability and vaporization temperature might provide a value for activation energy of oligomer formation. Presently, the process is not understood well enough to apply this relationship. However, qualitative observations (figure 2.17) suggest: 1) $Pb(thd)_2$ has a longer duration of thermal stability than $Pb(fod)_2$ over the temperature range studied. 2) If the slope of $\Delta(\ln \text{time})/\Delta(1/T)$ does represent an activation energy of the oligomer formation, then $Pb(thd)_2$ has a higher activation energy than $Pb(fod)_2$ (i.e. it is easier to oligomerize $Pb(fod)_2$ than $Pb(thd)_2$).

In summary of section 2.3.1 the following conclusions are made: 1) $Zr(thd)_4$ is thermally stable over the range of vaporization temperatures and times of the TGA experiments, and $Pb(fod)_2$ and $Pb(thd)_2$ are not thermally stable above 120 °C for any significant length of time. 2) The thermal instability is caused by oligomerization, which increases in rate with increasing temperature. Implications of these conclusions lead to ideas for fulfillment of the final objective of this study presented in section 1.3 . This objective is the optimization of precursors by the development of novel precursors which are engineered for the CVD process.

The major difference between the thermally stable $Zr(thd)_4$ and the thermally unstable lead β-diketonates [$Pb(thd)_2$ and $Pb(fod)_2$] is the number of coordinating ligands. Zirconium possesses 4 chelating ligands, or 8 bonds on the metal center. Lead possesses only 2 ligands, or 4 bonds on the metal center. Oligomer formation of metal β-diketonates has been described as a means of satisfying a degree of unsaturation of the metal center[3]. This is especially true for very large metal ions with low oxidation state, such as barium (II). Large metal ions with low oxidation state undergo oligomerization because the metal center is not sufficiently shielded by its few ligands (number of ligands equals oxidation state), and molecular interactions are more easily initiated. Since lead is also a very large metal ion, and zirconium is a relatively small metal ion, it is quite possible that the difference in thermal stability between the zirconium precursor and the lead precursors is that intermolecular reactions of lead precursors are more easily initiated.

2.3.1.3 Suggested future work

The previous analysis suggests that the lead precursors could be made more stable by adding more ligands to the metal center. Gardiner et al.[24] reported increase in volatility and thermal stability of barium (II) β-diketonates by increasing coordination through one tetraglyme ligand. Tetraglyme ($CH_3O(CH_2O)_4CH_3$) is a chelating ligand which bonds 5 times to the metal center through the lone pairs of the oxygens. Synthesis of 3 nine-coordinate compounds including $Ba(hfa)_2(CH_3O(CH_2O)_4CH_3)$, $Ba(tfa)_2(CH_3O(CH_2O)_4CH_3)$ and $Ba(thd)_2(CH_3O(CH_2O)_4CH_3)$ was reported.[25]

For future work, it is suggested that synthesis and characterization of mixed lead β-diketonate/polyether complexes should be carried out. In principle, the total coordination number of the compound can be varied from 6-9 by the choice of polyether. A monoglyme adduct (2 oxygens) will give a total coordination number of 6, and diglyme, triglyme and

tetraglyme could give coordination numbers of 7,8 and 9, respectively. The syntheses of $Pb(thd)_2$·tetraglyme and $Pb(thd)_2$·monoglyme were attempted briefly, starting with $Pb(thd)_2$ and the polyether. None of the desired product was isolated. It is suggested for future syntheses of these compounds, an alternative lead compound (i.e. lead alkoxide) is reacted with the β-diketonate ligand and polyether, rather than reacting the lead β-diketonate ligand with the polyether.

2.3.2 Decomposition Properties

In this section, the results of decomposition studies are presented and discussed with two major goals in mind. First, information which would directly apply to use of these precursors for the CVD process is presented. These topics include; onset and completion temperatures of metal oxide formation from the precursor, and identification of all additional phases formed by thermal decomposition processes.

The second goal is to approach an understanding of thermal decomposition processes of the precursor. Metal β-diketonates are rather complex molecules, and the thermal decomposition to metal oxides possibly involve some intermediate steps which form isolable compounds. Even in the case of simpler molecules such as the alkoxides, intermediate compounds such as mixed metal hydroxides-oxides-alkoxides, and oligomers have been documented[25]. Analagous studies of metal β-diketonates are not well documented in the literature. In general decomposition of the gas phase precursor to the metal oxide thin film during CVD comprises a complex sequence of reactions including; 1) gas phase reactions of the precursor near the substrate surface 2) adsorption of the precursor molecules (including products of gas phase reactions) onto the substrate surface 3) movement of molecules along the substrate surface 4) surface reactions of the precursors with film/substrate 5) desorption of precursor byproducts. In the case of the

metal alkoxides, the initiation step to metal oxide formation invariably results in less volatile compounds (i.e. oligomers, mixed metal hydroxide-oxide-alkoxides). Condensation of less volatile intermediate species on the substrate surface, followed by decomposition to metal oxides, is a reasonable mechanism of precursor decomposition.

The results of the decomposition studies of $Pb(thd)_2$ and $Zr(thd)_4$ discussed in this section suggest the existence of intermediate decomposition species which are analogous to those reported for the metal alkoxides. Decomposition studies of $Pb(fod)_2$ are also briefly mentioned. However these studies were not carried out in so much detail, due to experimental difficulties.

2.3.2.1 Thermal Decomposition of $Zr(thd)_4$

Sealed-tube decomposition experiments for $Zr(thd)_4$ were executed over the temperature range of 350 - 550 °C and decomposition times ranged from 10 to 90 minutes. Decomposition products of all experiments were examined by infrared spectrometry in the far IR range, 125-700 cm^{-1}. These spectra are compiled in Appendix A. The far infrared spectrum of $Zr(thd)_4$ precursor, and spectra of decomposition products from experiments carried out at 350, 450, 500, and 550 °C for 40 minutes are presented in figure 2.18. Spectra in figure 2.19 include $Zr(thd)_4$ precursor, and decomposition products at 550 °C for 10, 20 and 40 minutes. The spectra of decomposition products with increasing temperature and a constant time of 40 minutes, and the spectra of decomposition products with increasing time and constant temperature of 550 °C are quite similar. Therefore, progression of decomposition products of $Zr(thd)_4$ illustrated in figures 2.18 and 2.19 will be discussed together.

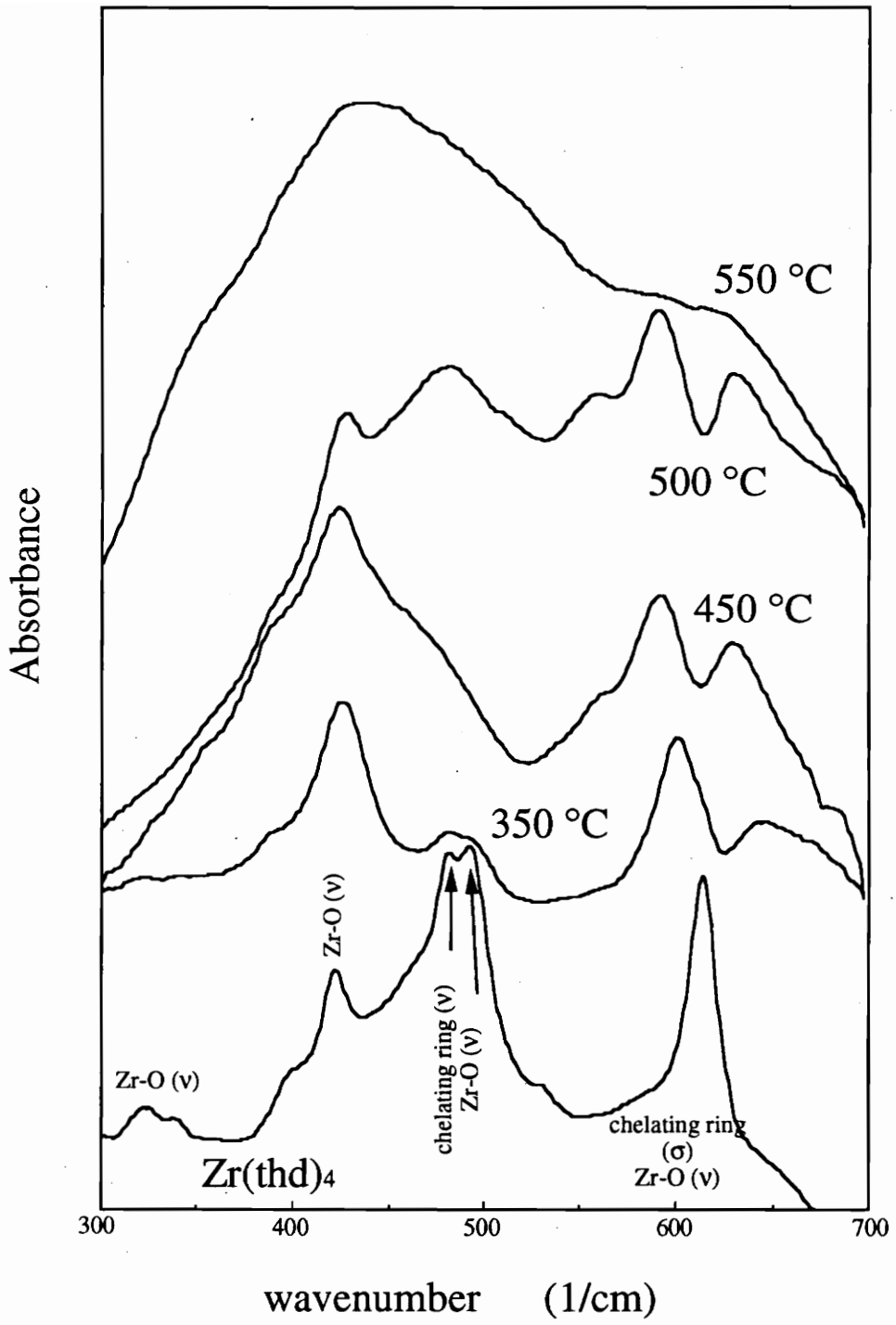

Figure 2.18
Far IR spectra of $Zr(thd)_4$ decomposition products
(40 minute decomposition time)

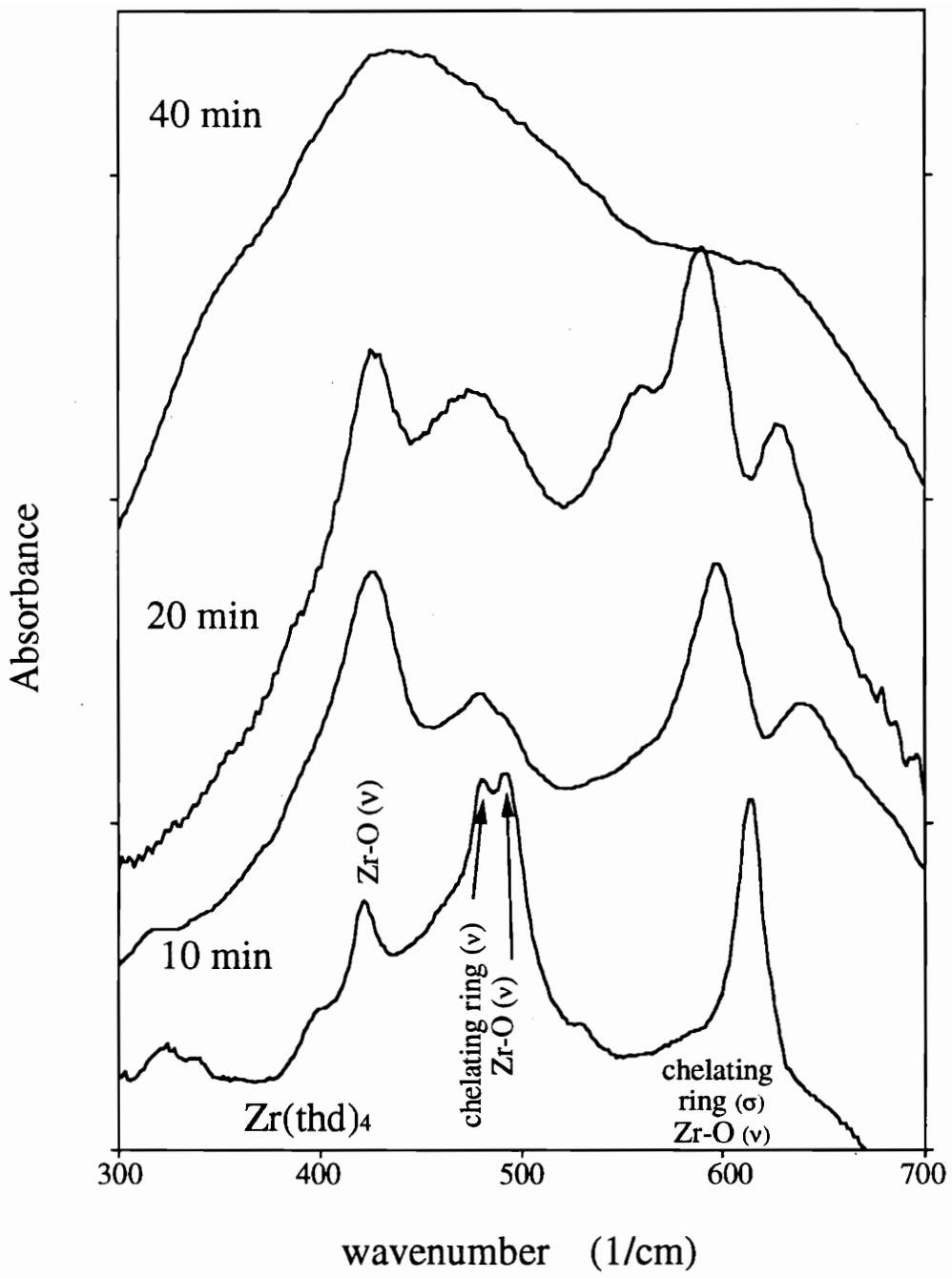

Figure 2.19
Far IR spectra of $Zr(thd)_4$ decomposition products (decomposition temp = 550 °C)

2.3.2.1.1 Evolution of Zr-ligand bonds during thermal decomposition

In the far infrared region, the observed bands are due to the metal-oxygen bond.[26] Some of the peak positions are sensitive to the nature of the chelating β-diketonate ring, as well as to the metal ion, and some are sensitive only to the metal ion. With reference to several sources,[3,27,28,29] the major peaks in the spectrum of $Zr(thd)_4$ precursor were identified due to metal-oxygen, or metal-chelate. The absorption peak at 613 cm^{-1} is a combination of bending (σ) of the chelating ring, and stretching (ν) of the zirconium-oxygen bond. [3,28] The two peaks at 481cm^{-1} and 492 cm^{-1} represent stretching of the chelating ring and stretching of the zirconium-oxygen bond. [28,30] Absorption peaks of zirconium-oxygen stretch (ν) which are not ligand sensitive are located at 322 cm^{-1} and 422 cm^{-1}.[3]

Since the peak at 613 cm^{-1} and the split peak centered at 481 and 492 cm^{-1} are sensitive to the chelating ring, they will suffice as fingerprint peaks of the $Zr(thd)_4$ precursor. The split peak completely disappears in both the decomposition product spectrum of 450 °C for 40 minutes, and the decomposition product spectrum of 550 °C for 10 minutes. The peak at 613 cm^{-1} is split to two peaks located at 596 cm^{-1} and 635 cm^{-1} in the decomposition product spectrum of 350 °C for 40 minutes and the decomposition product spectrum of 550 °C for 10 minutes. These peaks persist up to decomposition conditions of 500 °C for 40 minutes and 550 °C for 20 minutes. The small peak located at 322 cm^{-1} which was identified as a zirconium-oxygen stretch probably is also sensitive to the chelating ring, because it disappears under the same decomposition conditions as the split peak at 481 cm^{-1} and 492 cm^{-1}. Two additional peaks observed consistently at intermediate decomposition conditions are located at 425 cm^{-1} and 478 cm^{-1}. These peaks are first observed at decomposition conditions of 500 °C for 40 minutes and 550 °C for 20 minutes. At decomposition conditions of 550 °C for 40 minutes, all peaks are

encompassed by a very broad peak centered at 425-450 cm^{-1}, with a shoulder around 607-626 cm^{-1}. This peak is amorphous ZrO_2, thus marking the completion time and temperature of ZrO_2 formation from $Zr(thd)_4$. The peak positions were confirmed by IR spectrometry of ZrO_2 reference.

In summary of these experiments, IR absorption peaks are observed in $Zr(thd)_4$ decomposition products under intermediate conditions, which are not observed in either the $Zr(thd)_4$ precursor, or the final ZrO_2 product. In other words, intermediate species are formed upon heating of the $Zr(thd)_4$ precursor, which react to form ZrO_2, upon further heating.

Another intriguing consistency observed in the intermediate products of decomposition is the solubility properties of the various samples. Decomposition products which possess peaks at 596 and 635 cm^{-1}, but do not have the precursor fingerprint peaks at 425 and 478 cm^{-1} (i.e. 350 °C for 40 min and 550 °C for 10 min), were completely soluble in organic solvents such as toluene. On the other hand, decomposition products which possessed all four peaks at 596, 635, 425, and 478 cm^{-1} were only partially soluble in organic solvents. This indicates that $Zr(thd)_4$ decomposition products which have the IR spectral peak positions at 596 and 635 cm^{-1} consist mainly of intermediate products of decomposition, and contain no ZrO_2. Additionally, decomposition products which have all four intermediate peaks present in the IR spectrum consist of a mixture of intermediate products and ZrO_2.

Chemical ionization mass spectrometry was employed to attempt to identify the intermediate species which have IR absorptions at 596 and 635 cm^{-1} (i.e. decomposition products formed at 350 °C for 40 min or 550 °C for 10 min). Mass spectrometry of the $Zr(thd)_4$ precursor is also presented for comparison. The results are summarized in table 2.7. The $Zr(thd)_4$ sample consists mainly of monomeric species, and very few oligomeric

species (<5%). Oligomeric species are frequently reported to exist in the solid state of metal β-diketonates.[3] The monomeric daughter ions [$Zr(thd)_3$, $Zr(thd)_2(OH)$ and Zr(thd)O] are analogous to those observed in the reported mass spectrum of $Zr(acac)_4$.[30] Mass spectral data suggests the $Zr(thd)_4$ product of decomposition at 350 °C for 40 minutes is a mixture of 2 and 3 zirconium oligomeric species, containing both Zr-thd chelating bonds and Zr-O bonds. (These species will be discussed in further detail later.) The only discernable peak of monomeric $Zr(thd)_4$ in this sample was a 10% relative abundance of $Zr(thd)_4$ - t-butyl.

Table 2.7 Mass spectral identification of $Zr(thd)_4$ and decomposition species

$Zr(thd)_4$			$Zr(thd)_4$ decomposed in oxygen (350 °C for 40 minutes)		
specie	molecular weight	relative abundance	specie	molecular weight	relative abundance
$Zr(thd)_3$	640	100%	$Zr_2(thd)_4(O)_2$	946	85%
$Zr(thd)_2(OH)$	474	10%	$Zr_2(thd)_5(O)$	1113	25%
Zr(thd)(O)	290	10%	$Zr_3(thd)_8(O)$	1753	100%
$Zr(thd)_4O_2$	946	5%	$Zr_3(thd)_5(O)_2$	1220	70%
$Zr_2(thd)_7$ - t-butyl	1406	<1%	$Zr_3(thd)_4(O)_2$	1037	100%

Proton nuclear magnetic resonance spectrometry presents further evidence for the existence of mixed Zr-O-thd structures. Figure 2.20 shows the methyl proton region of NMR spectra of 1) $Zr(thd)_4$, and 2) $Zr(thd)_4$ decomposition products at 350 °C for 40 minutes. There is only one peak in the methyl region of the NMR spectrum of $Zr(thd)_4$

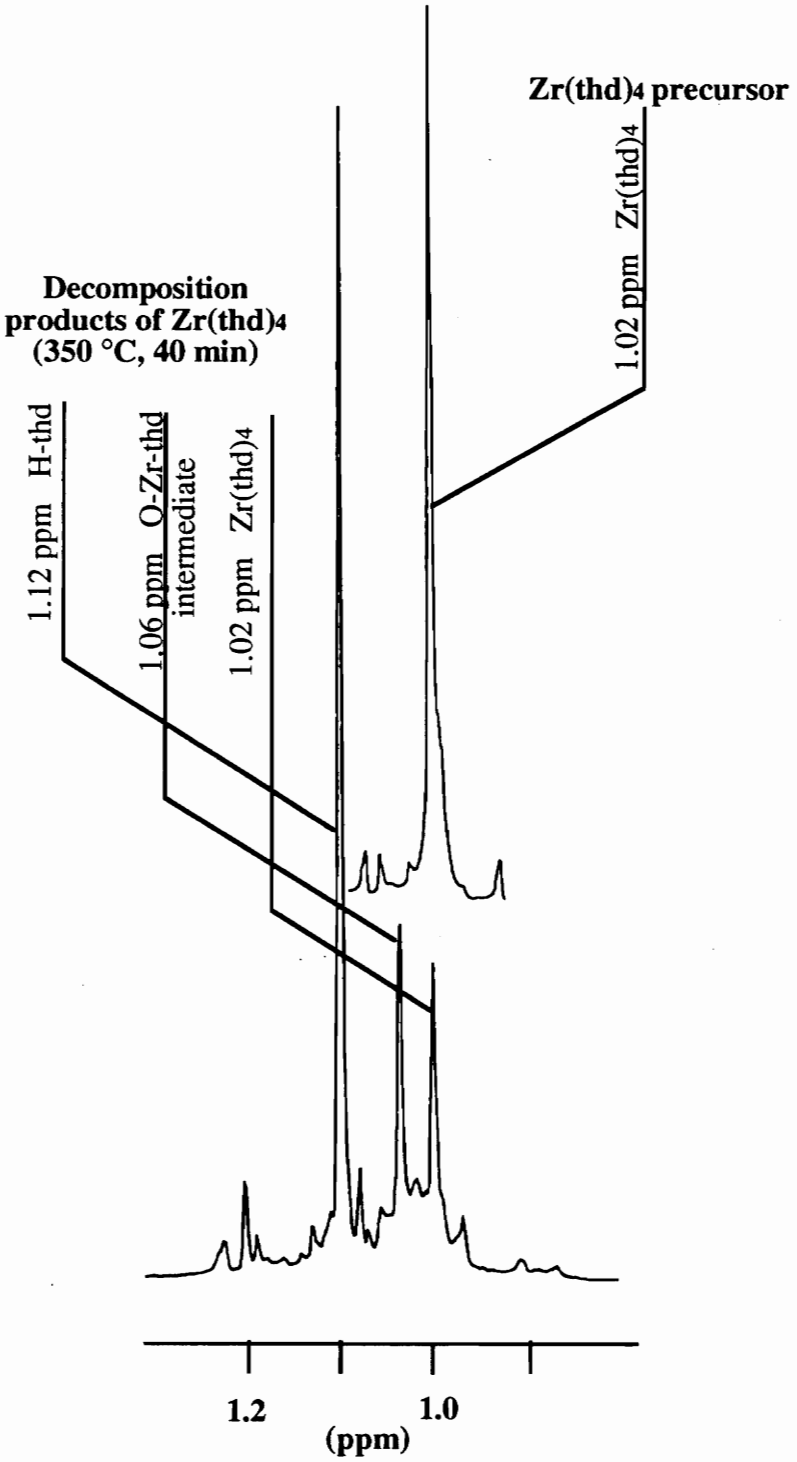

Figure 2.20 Proton NMR methyl region.
[Zr(thd)4 precursor and decomposition products (350 °C, 40 min)]

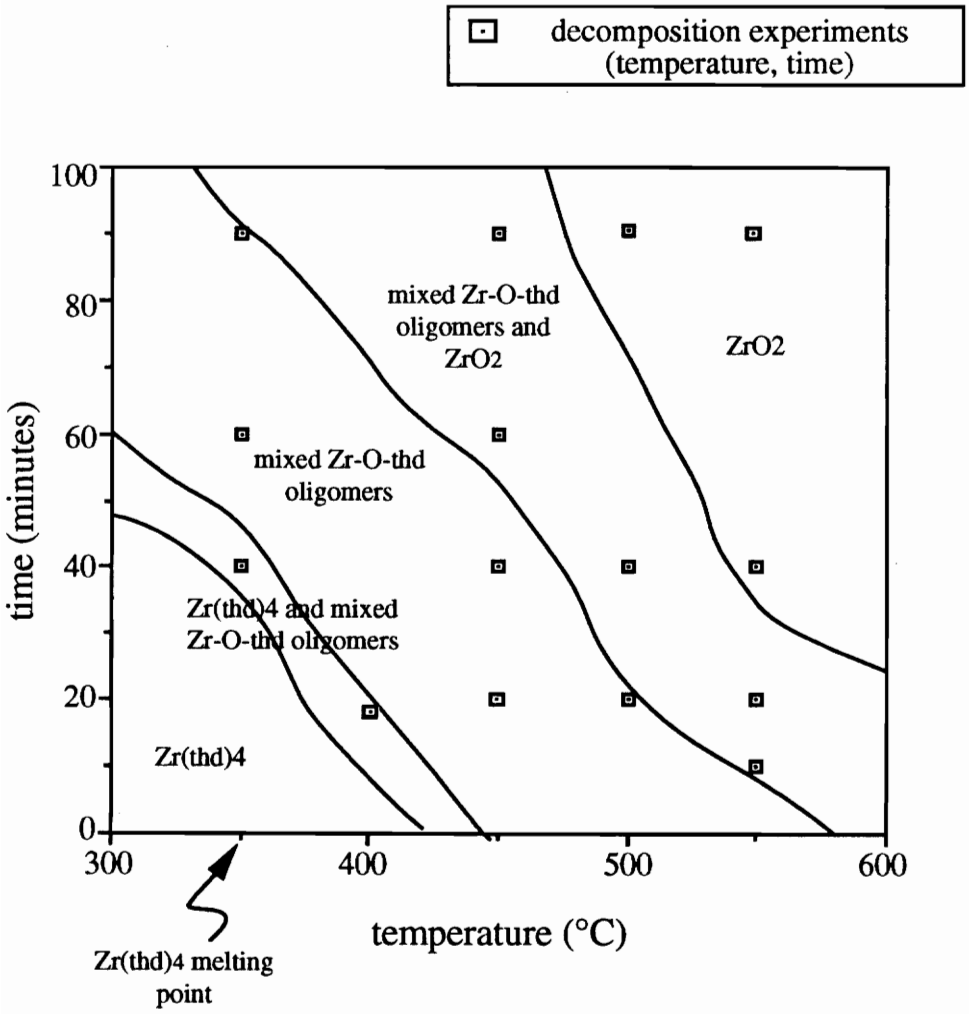

Figure 2.21
Stability diagram of Zr(thd)4 heated at decomposition temperatures in an oxygen atmosphere

precursor, which is located at 1.02 ppm. In the NMR spectra of decomposition products obtained at 350 °C for 40 minutes, there are three major peaks in the methyl region, and many minor peaks. The largest peak is located at 1.12 ppm, which is the methyl position of the H-thd ligand, as shown in figure 2.5. The presence of nonbonded ligand is consistent with the mass spectrometry results. The ratio of thd : Zr is less for the oligomers (4:3 - 8:3) than for the monomer (4:1), so free ligand is generated by the process of oligomer formation from monomers. The second methyl peak is the methyl peak of the $Zr(thd)_4$ precursor (1.02 ppm). The third major methyl peak located at 1.06 ppm has not been previously identified in thd-containing samples; therefore, it probably belongs to the mixed ligand, oligomeric complexes. The position of this peak , which is located between the H-thd methyl peak and the $Zr(thd)_4$ monomer methyl peak, is consistent with NMR theory of peak positions. Protons which are in an electron rich environment require a higher applied magnetic field to be brought into resonance, and are located closer to 0 ppm (upfield), and protons which are less shrouded by electrons are shifted further downfield. The methyl protons of the thd-ligand bonded to the metal are located in a more electron rich environment than the free ligand methyl protons, because delocalized electron bonding exists in the metal chelating ring. Therefore, the Zr-thd methyl peak is further upfield than the H-thd methyl peak. In the case of the mixed O-Zr-thd complexes, the methyl protons are shrouded by the delocalized chelate ring electrons. However, the Zr ion is also bonded to electronegative oxygen, which would remove some of the electron density from the chelating ring. Therefore, it is not unreasonable for the methyl peak of the mixed ligand complex to be located between the methyl peaks of the $Zr(thd)_4$ monomer and the H-thd.

Intermediate species consisting of zirconium, oxygen and thd have been identified in products of partial thermal decomposition of $Zr(thd)_4$ via IR spectrometry, proton NMR spectrometry and mass spectrometry. Presence of ZrO_2 in decomposition products has

been verified by its lack of solubility in organic solvents, and by IR spectrometry. The presence of $Zr(thd)_4$ monomer in decomposition products is identified by the fingerprint peaks at 613, 482, and 491 cm^{-1}. In order to compile the results of this study, a stability diagram of the $Zr(thd)_4$/O-Zr-thd/ZrO_2 system was constructed (figure 2.21).

2.3.2.1.2 Evolution of chelating ring during thermal decomposition

In addition to the far IR spectral analyses, a few samples were examined via mid-IR spectrometry (400 - 5000 cm^{-1}). All the C-H, C-O, and C-C absorptions are located in the mid IR region; therefore, decomposition of the ligands is observed in this region. Figure 2.22 displays the mid-IR spectra of H-thd, $Zr(thd)_4$, and products of decomposition experiments carried out under the follow conditions: (40 min, 350 °C), (40 min, 450 °C), and (40 min, 550 °C). Major peaks were identified with reference to several sources[28,31] ; these are labeled as bond stretching (ν), in plane bending (σ) and out of plane bending (π). The decomposition of the skeletal chelating ring structure upon heating can be observed in the evolution of the characteristic C-O and C-C absorptions. The absorption band at 873 cm^{-1} is the stretching mode of C-O and C-C of the chelating ligand.[28] This band is reduced in intensity upon decomposition at 350 °C, and absent upon decomposition at 450 °C. The CH_3 symmetric deformation is observed at 1363 cm^{-1} for the H-thd, and at 1359 cm^{-1} for the $Zr(thd)_4$. [28] Upon decomposition of $Zr(thd)_4$ at 350 °C and 450 °C, the symmetric deformation band of CH_3 is split to 1359 cm^{-1} and 1381 cm^{-1}. This split might also be consistent with the split of the methyl peak in proton NMR spectrometry (figure 2.20). Somewhere between 450 °C and 550 °C all absorptions bands of the chelating ring disappear. At this point , most of the β-diketonate chelating ring is is evidently combusted to water, and volatile phases such as methane and CO_2. Increased pressure in the sealed tubes suggests volatile byproducts, and water is visible. "Soot" is also evident, because

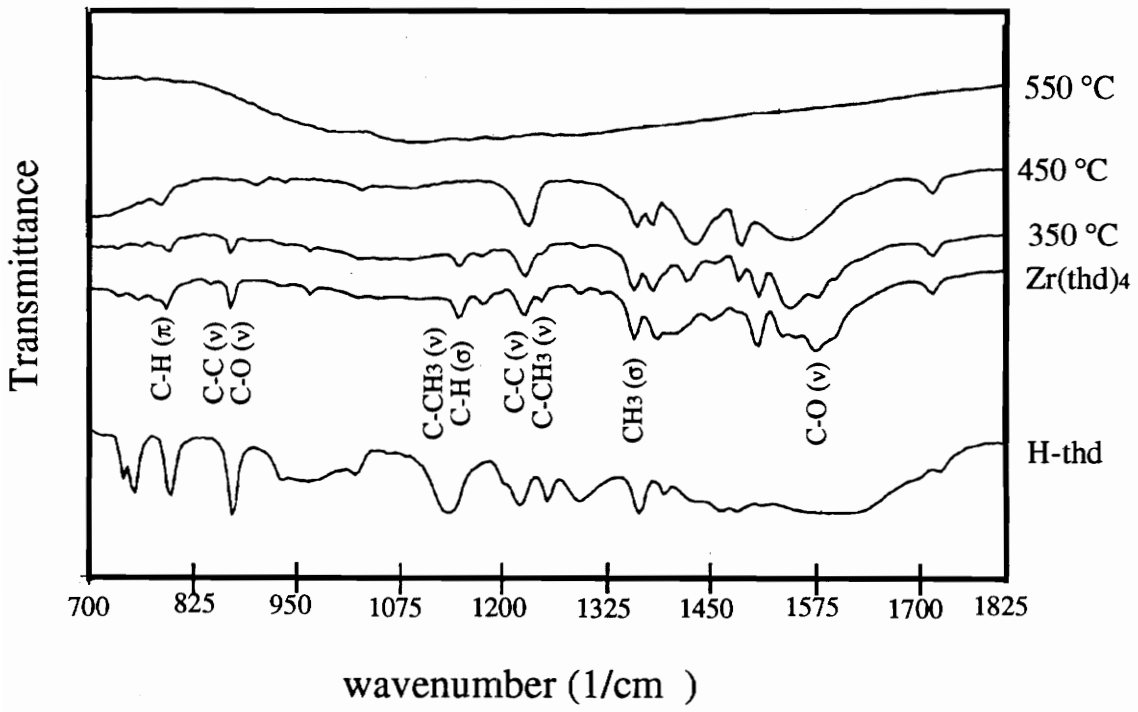

Figure 2.22
Mid IR spectra of $Zr(thd)_4$ decomposition products (40 minute decomposition time)

there is not enough oxygen present to stoichiometrically oxidize all the carbon of the thd-ligands.

2.3.2.1.3 Suggested Future Work

In summary of this section on $Zr(thd)_4$ decomposition studies, the final objective of this study presented in section 1.3 will be addressed. This objective is the development of novel precursors which are specifically engineered for the CVD process. The mixed thd-Zr-O species detected by mass spectrometry invoke some ideas concerning novel ZrO_2 precursors. The structures of four of the major detectable species, $Zr_2(thd)_5(O)$, $Zr_3(thd)_8(O)$, $Zr_3(thd)_4(O)_2$ and $Zr_3(thd)_5(O)_2$, are rather difficult to surmise. Because there is an odd number of thd ligands and/or odd number of zirconium atoms in these species, the zirconiums of a single molecule will have varying coordination (two to eight ligand bonds per zirconium), since bridging of the thd-ligands is unlikely. The bridging structure is unlikely because of the very stable nature of the 6-member chelating ring which the β-diketonate ligand forms with the metal (stabilized by delocalized π-electron bonding). To gain an understanding of the feasible structures of these oligomers, all means of coordination of the oxygen and thd ligands must be examined. The oxygens ligands are not necessarily limited to coordinating only two zirconiums, and the ketone oxygens of the thd-ligands are not limited to coordinating one zirconium. Oxygen possesses two lone electron pairs which can be donated to a second metal center. Therefore, a third bond is possible for both the oxygen ligand which bridges two zirconiums, and for the thd-oxygen which bridges the zirconium and the β-carbon of the chelating ring. Cotton and Rice[32] reported the structure of the dimer $[Fe(acac)_2]_2$ to have the oxygen of the chelating ligand of one iron atom to be located in the coordination sphere of the other iron atom. In other words, the oxygen of the thd-ligand can bridge the two metal centers and the carbon of the

chelating ring. Similarly, the oxygen ligand can bridge three metal centers. There are many possibilities how these species could be coordinated, but further work, such as single crystal X-ray analysis, is necessary to characterize these structures.

The fifth mixed thd-Zr-O specie detectable by mass spectrometry, $Zr_2(thd)_4(O)_2$, is possibly more comprehensible than the other four. Mehrotra[3] reported the crystal structure of $Ti_2(acac)_4(O)_2$, a compound analogous to the dimeric specie $Zr_2(thd)_4(O)_2$. This structure is depicted in figure 2.23 for the $Zr_2(thd)_4(O)_2$ specie. The structure described by Mehrotra consists of two edge sharing octahedra with the metals at the octahedral centers and bridging oxygens along the shared edge.

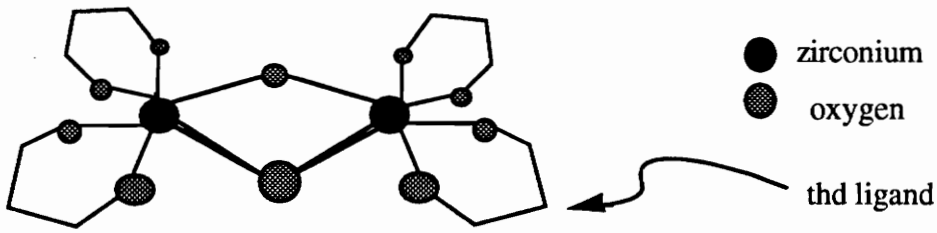

Figure 2.23 $Zr_2(thd)_4(O)_2$

This structure is closer to the final perovskite structure of PZT than $Zr(thd)_4$. The zirconium are in 6-fold coordination, instead of 8-fold coordination, and Zr-O-Zr bonds already exist in the structure.

In order to utilize this intermediate phase as a precursor for CVD, synthesis and/or isolation of the molecule must carried out, and its volatility properties must be characterized. Another thin film production process which might benefit from the synthesis and characterization of $Zr_2(thd)_4(O)_2$ is the solution methods. This compound is potentially useful for solution methods because 1) it is soluble in organic solvents and 2) high volatility of precursors is not necessary for this method.

Additionally, formation of ZrO_2 from this compound could probably be executed at a lower formation temperature than the 500-550 °C necessary to decomposed $Zr(thd)_4$ to ZrO_2. This is assumed because $Zr_2(thd)_4(O)_2$ is the intermediate species of the $Zr(thd)_4$/O-Zr-thd/ZrO_2 system in which: 1) $Zr(thd)_4$ is stable from ambient temperature to around 400 °C, 2) intermediate species are formed from approximately 350-500 °C, and 3) ZrO_2 is formed at approximately 500 °C (figure 2.21).

2.3.2.3 Thermal decomposition of $Pb(thd)_2$

Sealed-tube decomposition experiments for $Pb(thd)_2$ were executed over the temperature range of 200 - 500 °C, and decomposition times ranged from 15 to 80 minutes. Decomposition products of all experiments were examined via infrared spectrometry in the far IR range (125-700 wavenumbers). These spectra are compiled in appendix B. Figure 2.24 shows the far IR spectra of $Pb(thd)_2$ precursor, and decomposition products of experiments executed for 40 minutes at 250 °C, 300 °C, 350 °C and 400 °C. In addition to the near IR analyses, a few decomposition products were examined in the mid IR range to observe the decomposition of the chelating ring. Figure 2.25 shows the spectral range of 700-1700 cm^{-1} of $Pb(thd)_2$ precursor, and products obtained from decomposition at 300, 350, and 400 °C for 40 minutes. Interpretation is analogous to the interpretation of the $Zr(thd)_4$ mid IR spectra (figure 2.22). Complete decomposition of the chelating ring is never observed in figure 2.25. This is in agreement with the $Zr(thd)_4$ decomposition spectra, because complete decomposition of the $Zr(thd)_4$ chelating ring took place above 450 °C. The far IR decomposition product spectra of experiments executed at 40 minutes with increasing temperature covers the entire range of $Pb(thd)_2$ decomposition products observed. Therefore, the decomposition will be discussed with reference to figure 2.24.

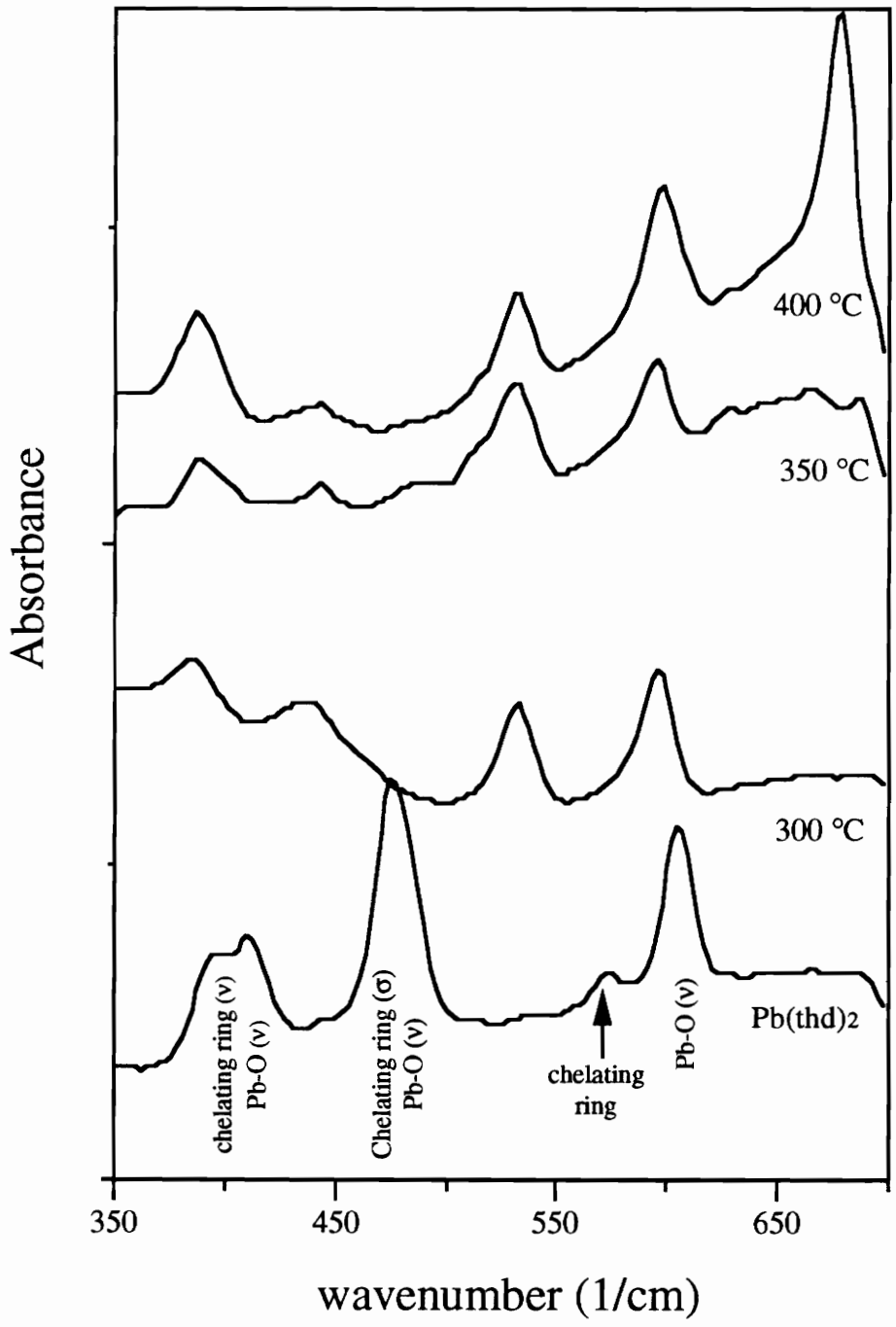

Figure 2.24
Far IR spectra of Pb(thd)2 decomposition products (40 minute decomposition time)

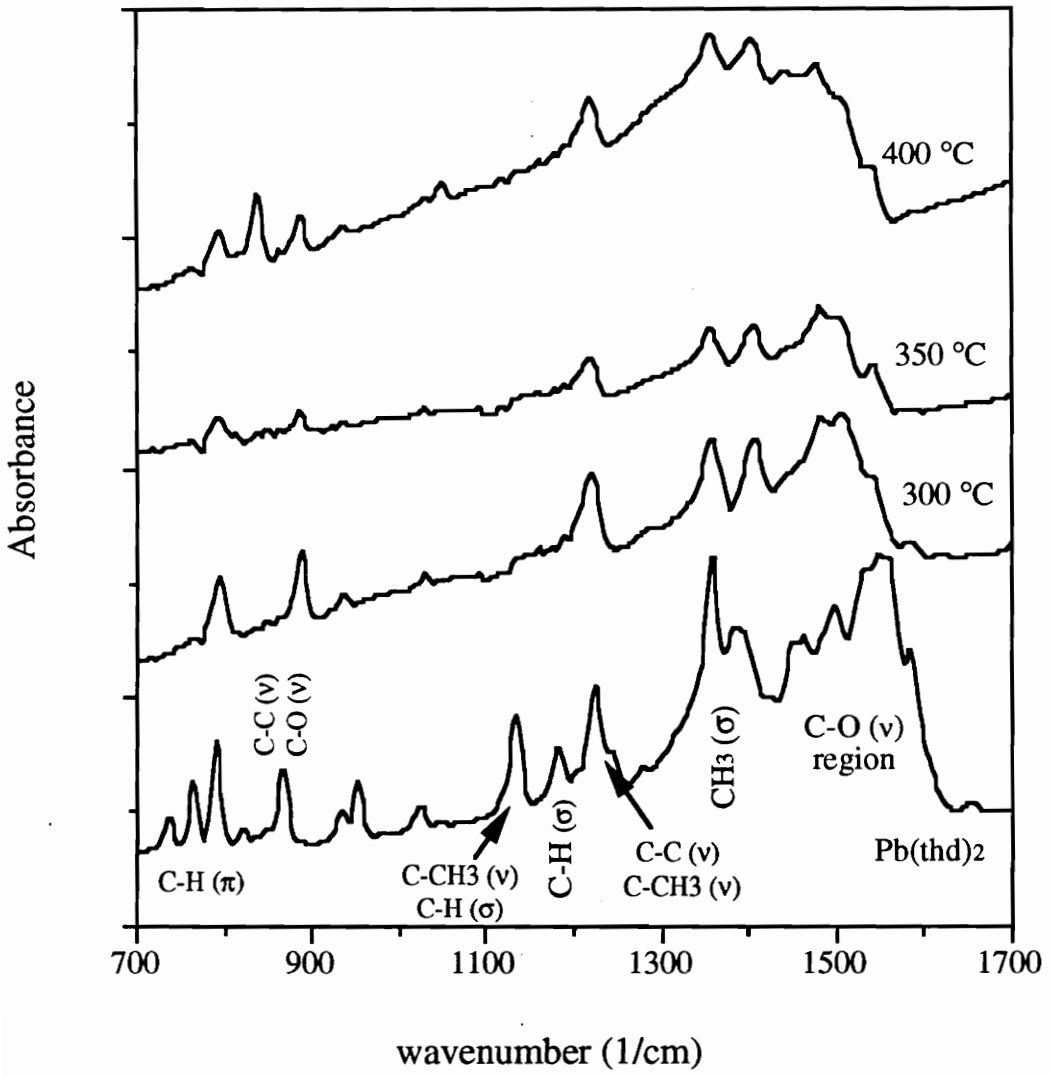

Figure 2.25
Mid IR spectra of Pb(thd)2 decomposition products (40 minute decomposition time)

The far IR spectra of $Pb(thd)_2$ precursor were interpreted with reference to a report by Lawson[30] concerning far IR spectra of metal acetylacetonates. The greek character "ν" denotes stretching of the Pb-O bond or the chelating ring; "σ" denotes bending of the chelating ring (figure 2.24). The metal-ligand is responsible for all absorptions in the far IR range, as was the case described for $Zr(thd)_4$. The peak positions are labeled in figure 2.24 as Pb-O and/or chelating ring absorptions. The peaks labeled "chelating ring" are Pb-O absorptions which are sensitive to the thd-ligand, and therefore serve as fingerprint peaks for the $Pb(thd)_2$ precursor. These peaks are located at 570 cm^{-1} and 477 cm^{-1}. There is also a split peak with maximums at 392 and 412 cm^{-1} which is sensitive to the chelating ring. There is a fourth, fairly sharp peak located at 155 cm^{-1} which is also sensitive to the chelating ring. This region of the spectra is not shown in figure 2.24 because of the excessive noise in this region for many of the decomposition spectra. However, the region (125-300 cm^{-1}) can be examined in appendix B.

Decomposition products of the experiment carried out at 250 °C for 40 minutes only slightly show the original $Pb(thd)_2$ precursor fingerprint absorptions. There is a slight shoulder remaining of the split peak at 392 and 412 cm^{-1}; and the other chelate-sensitive peaks at 477 and 570 cm^{-1} are not detectable. Absorption peaks of intermediate decomposition products (i.e. mixed O-Pb-thd complexes) are detectable in the range of 300-375 cm^{-1}. The decomposition experiment carried out at 250 °C for 40 minutes shows a broad absorption centered at 360 cm^{-1}. The spectrum of decomposition products obtained at experimental conditions of 300 °C for 40 minutes reveals a split in this broad peak, with maximums at 321 and 387 cm^{-1}. The absorption positioned at 387 cm^{-1} becomes more intense with increasing temperature, and the absorption position at 321 cm^{-1} disappears by 350 °C for 40 minutes.

The Pb-O absorptions of the $Pb(thd)_2$ precursor sample which are not sensitive to the chelating ring are also discernable. These peaks are only slightly sensitive to thermal decomposition of $Pb(thd)_2$ to lead oxide, and are seen in all decomposition spectra of increasing temperature and time of experiment. Also, additional Pb-O peaks which are not present in the precursor sample appear in the decomposition product spectra. The Pb-O absorption in the $Pb(thd)_2$ precursor sample which is only slightly sensitive to the chelating ring is located at 602 cm^{-1}. Decomposition at 250 °C for 40 minutes results in a shift to 595 cm^{-1}. The peak remains in this position for all decomposition products of increasing temperature. The spectrum of decomposition products obtained at 250 °C for 40 minutes has an additional Pb-O absorption at 532 cm^{-1}. This peak remains unchanged for all decomposition conditions of increasing time and/or temperature. Additional peaks located at 387 and 440 cm^{-1} first appear in the decomposition spectrum of 300 °C for 40 minutes, and becomes more intense with increasing temperature and time of decomposition. In order to confirm the assignment of these peaks (595, 532, 440, and 387 cm^{-1}) as Pb-O absorptions, it is necessary to analyze a PbO standard. This proved to be problematic.

Lead reactivity with various experimental media hindered defining of a suitable PbO standard to pinpoint the fingerprint peaks which would indicate initiation and completion of lead oxide formation. The $Pb(thd)_2$ decomposition products were deposited on a silicon wafer in the quartz reaction tube during the experiments (described in section 2.2.3). When the silicon wafer was removed from the tube and dried in air, the mixture of decomposition products adhered to the silicon wafer well enough to allow infrared analysis of the sample. Similarly, the $Pb(thd)_2$ precursor, which was melted on a silicon substrate, adhered sufficiently for analysis. This was not the case of PbO. The fine powder does not adhere, and has a very high melting point. Therefore, PbO powder was mixed with KBr and pressed into a pellet for analysis. In the IR spectrum of the PbO sample in the KBr

pellet medium, a sharp and intense absorption peak is located 688 cm^{-1}. Similarly, both $Pb(fod)_2$ and $Pb(thd)_2$ samples mixed with KBr and pressed into a pellet exhibited the same sharp, intense peak located at 688 cm^{-1}. However, this peak was not found in any of the $Pb(thd)_2$ decomposition experiments which were analyzed on the silicon wafer, including the $Pb(thd)_2$ precursor sample which was melted on the silicon wafer. One possible explanation is that the lead is reacting with the KBr during a stage of preparing the pellet. There are 3 steps in which this could potentially occur; 1) during grinding and mixing of the lead-containing sample with KBr in an acetone medium 2) during heating at 150 °C to drive off moisture 3) during pellet pressing (25,000 lbs pressure for 5 minutes). Several reported compounds containing lead, potassium, bromide and water, documented by X-ray diffraction include; $PbBr_2$, $PbBr_2 \cdot 3H_2O$, PbBr(OH), K_2PbBr_4, KPb_2Br_5, and $KPbBr_3$.[33]

Since a standard could not be obtained by available means of infrared analysis, X-ray diffraction was used to confirm the existence of PbO in the decomposition products. Figure 2.26 illustrates the X-ray diffraction pattern of $Pb(thd)_2$ decomposed at 300 °C for 40 minutes. The two major peaks of massicot PbO are present ($2\theta = 29.1°$, $2\theta = 32.7°$). Other unidentifiable peaks are present. It is reasonable to assume these peaks belong to either $Pb(thd)_2$ precursor, or the intermediate species of O-Pb-thd. Analysis of $Pb(thd)_2$ precursor by X-ray diffraction in the same range as the pattern shown in figure 2.24 (2θ = 25-35°) revealed no peaks. Therefore, no peaks of $Pb(thd)_2$ exist in this range, and the remaining uninterpreted peaks in figure 2.26 probably belong to intermediate O-Pb-thd compounds.

So far, there has been no mention of the intense peak located at 677 cm^{-1} in the spectra of $Pb(thd)_2$ decomposition products obtained at 400 °C for 40 minutes (figure 2.24). This peak is observed consistently in the decomposition products of higher

temperature and/or time of decomposition, starting at 300 °C for 60 minutes, 350 °C for 40 minutes, and 400 °C for 20 minutes. Analysis by X-ray diffraction of the decomposition products obtained at 400 °C for 40 minutes provided a quite plausible explanation for this IR peak at 677 cm^{-1}. The X-ray diffraction pattern of this sample in the range $2\theta = 25° - 35°$ (figure 2.27) has the most intense peak of massicot lead oxide ($2\theta = 29.1°$), and one other peak located at $2\theta = 28.3°$. This peak is located at the position of the most intense lead silicate (Pb_3SiO_5) peak.[34] Lead silicate commonly reacts with silicon substrates at higher temperatures. This reaction has been observed by other workers in this lab during higher temperature CVD deposition (i.e. > 400 °C) of lead materials on silicon substrates.

Further analysis of decomposition experiments executed at intermediate temperatures and/or times were carried out in order to approach a better understanding of the $Pb(thd)_2$ intermediate decomposition species. Mass spectrometry analyses of $Pb(thd)_2$ precursor and $Pb(thd)_2$ decomposition products (300 °C, 40 minutes) are presented in table 2.8. The mass spectral results of the $Pb(thd)_2$ precursor were presented and discussed previously in section 2.3.1. The intermediate decomposition products of $Pb(thd)_2$ are similar to those observed for $Zr(thd)_4$. Mixed O-Pb-thd molecules are the dominant species of the intermediate decomposition products. Feasible structures for these species are not difficult to hypothesize. In the dimer species (2 leads), the oxygens can be terminal or bridging, and the terminal oxygens can be singly or doubly bonded to the lead. In the case of the $Pb_2(thd)_2$ complex, the oxygens of the thd-ligands are likely to be coordinated to one lead, and associated to the other lead within its coordination sphere. This structure for iron acetylacetonates is described by Cotton and Rice.[27]

One interesting feature of these intermediate species detected by mass spectrometry is that the ratios of Pb:O and Pb:thd suggest the molecules would best be arranged in an asymmetric structure. For instance, the PbO(thd) molecule would be asymmetric,

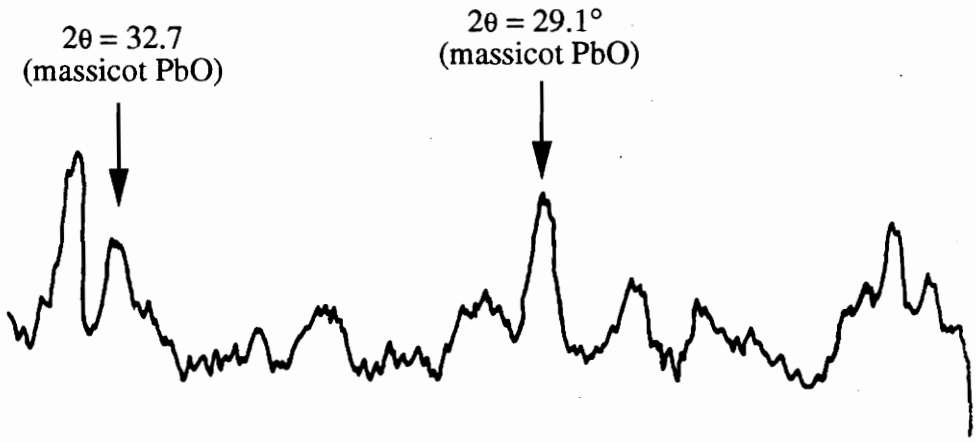

Figure 2.26
X-ray diffraction pattern of Pb(thd)2 decomposition products (300 °C, 40 min)

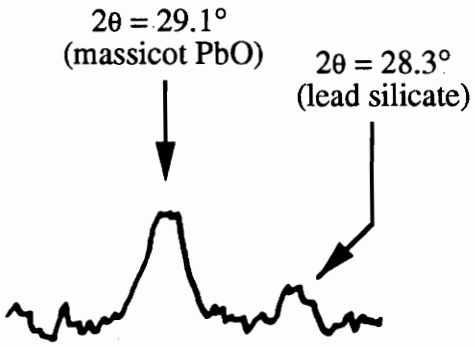

Figure 2.27
X-ray diffraction pattern of Pb(thd)2 decomposition products (400 °C, 40 min)

regardless of the bond angle which exists between O-Pb-thd ring. The asymmetric O-Pb-thd intermediates should also be polar. The asymmetry and polarity of the $Pb(thd)_2$ intermediate decomposition products might play an important role in the CVD process.

Table 2.8 Mass spectral data of $Pb(thd)_2$ intermediates of decomposition.

Pb(thd)2 precursor		Pb(thd)2 decompositin products (300 °C, 40 minutes)	
specie	relative abundance	specie	relative abundance
Pb(thd)2	100%	PbO2(thd) - t-butyl	100%
Pb(thd)	100%	PbO(thd)	90%
Pb(thd)2 - (t-butyl)	100%	Pb2O2(thd)	6%
Pb2(thd)3	100%	Pb2(thd)2 - t-butyl	20%
Pb3(thd)4 - 3(t-butyl)	<1%	Pb2O2(thd)2	<0.5%

To understand this hypothesis, it is useful to examine a study reported by Fischman and Peuskey[34] concerning CVD of silicon carbide with methane as a carbon precursor, and methyltrichlorosilane (MTS) as a silicon precursor. This study demonstrated the mechanisms of the MTS and methane decomposition, and how the mechanisms control the film growth rate. Silicon was found to have a significantly higher growth rate than carbon. The following reasons for this phenomenon were cited: The silicon-carbon bond is thermodynamically the weakest bond in the MTS molecule. Therefore, this bond breaks first by free radical mechanism during gas phase, thermal decomposition. The resulting gas phase silicon radical is $\cdot SiCl_3$. This asymmetric, polar molecule has a greater sticking probability on the polar Si or SiC surface than the symmetric methane molecule, which does not undergo any significant gas phase

decomposition. Therefore, the silicon growth rate is more rapid than carbon growth rate, which is controlled by the increased sticking probability of the silicon precursor intermediate.

Perhaps a similar analogy can be suggested for the relative growth rates of ZrO_2 and PbO from $Zr(thd)_4$ and $Pb(thd)_2$. The decomposition studies of $Zr(thd)_4$ and $Pb(thd)_2$ have shown that $Zr(thd)_4$ requires a significantly higher temperature (500-550 °C) than $Pb(thd)_2$ (300-350 °C) to produce their respective oxides. Decomposition studies have also shown that intermediate molecules of $Pb(thd)_2$ decomposition, such as PbO(thd) might be asymmetric and polar. On the other hand, structures which might be predicted for $Zr(thd)_4$ precursor molecules, such as that shown in figure 2.23 are symmetric. Although the structure of the intermediate species of $Pb(thd)_2$ and $Zr(thd)_4$ decomposition have not been characterized, the general symmetry, or asymmetry of their structure might be understood in a qualitative sense by comparing the oxygen:metal ratios and thd:metal ratios (Table 2.9).

Table 2.9

Metal:ligand ratios of some intermediate decomposition species of $Pb(thd)_2$ and $Zr(thd)_4$

thd : Zr	O : Zr	thd : Pb	O : Pb
2 : 1	1 : 1	1 : 1	2 : 1
8 : 3	1 : 3	1 : 1	1 : 1
4 : 3	2 : 3		

Presented in table 2.9 is the ligand: metal ratios of the most abundant (> 85% relative abundance) species found in the mass spectra of intermediate decomposition species of $Zr(thd)_4$ and $Pb(thd)_2$ (from tables 2.7 and 2.8). In general, there are more zirconiums per

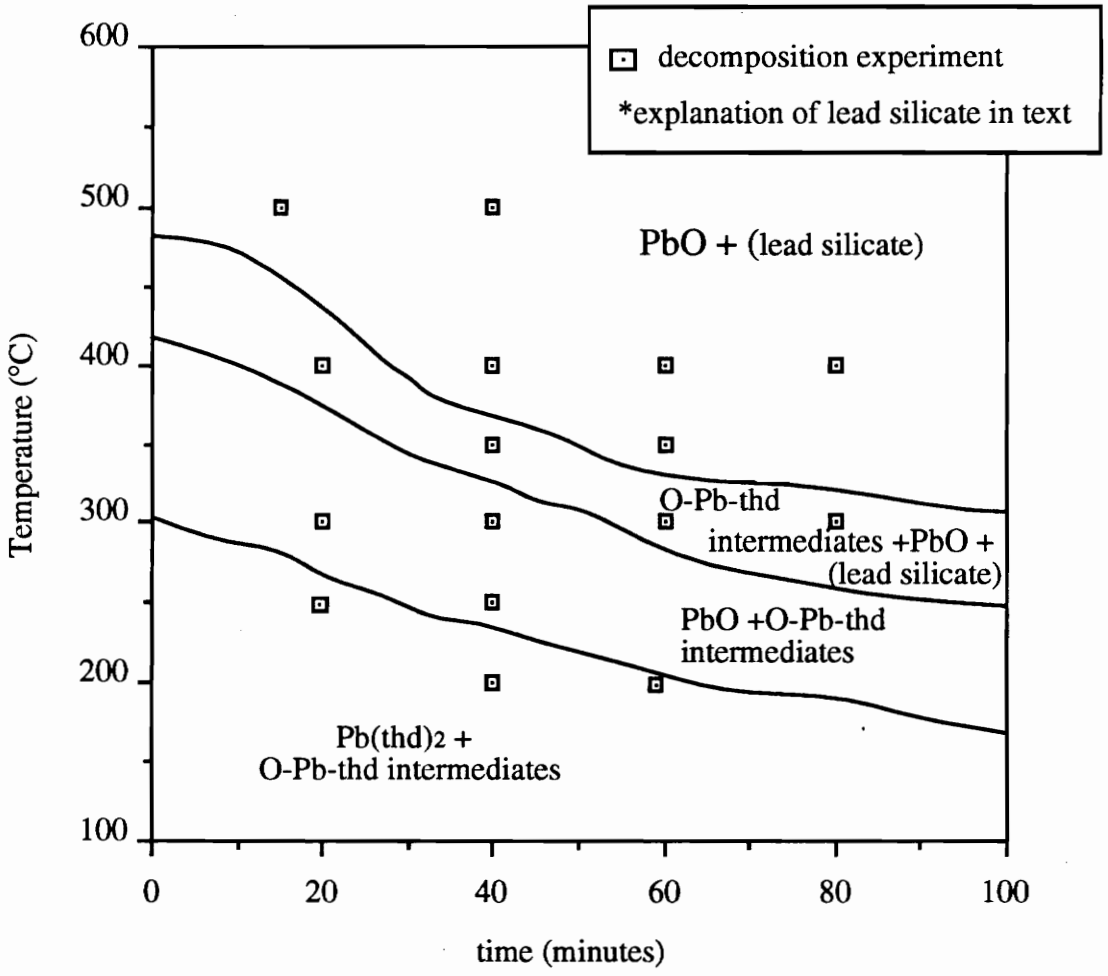

Figure 2.28
Stability diagram of Pb(thd)2 heated
at decomposition temperatures in an oxygen atmosphere

oxygen than there are leads per oxygens. This suggests that the oxygens of the zirconium compounds are more likely to be bridging, and the oxygen of the lead compounds are more likely to be terminal. There are also more thd-ligands per zirconium than there are thd-ligands per lead. In fact, there is only one thd-ligand per one lead in the two most abundant $Pb(thd)_2$ intermediate species. According to these ratios, the zirconium complexes might consist of a central core of Zr-O-Zr bridges, shrouded by a cloud of thd-ligands. On the other hand, the lead species have central leads with terminal oxygens and thd-ligands. In other words, the zirconium intermediate species might be rather symmetric, and the lead intermediate species appear to be asymmetric and polar. This might be a contributing factor to the high temperature necessary to decompose $Zr(thd)_4$, relative to the temperature necessary to decompose $Pb(thd)_2$ (i.e. O-Pb-thd intermediates have higher sticking coefficients that O-Zr-thd intermediates).

Finally, in order to compile the $Pb(thd)_2$ decomposition analyses, a stability diagram (figure 2.28) of the decomposition phases was constructed from the host of decomposition experiments presented in appendix B. Fingerprint peaks included; 477, 392-412, and 570 cm^{-1} for $Pb(thd)_2$ precursor, 532, 595, 387, and 442 cm^{-1} for PbO, 325-375 cm^{-1} for intermediate O-Pb-thd species, and 677 cm^{-1} for lead silicate.

2.3.2.4 Thermal decomposition of $Pb(fod)_2$

The decomposition studies of $Pb(fod)_2$ required the addition of water to each quartz tube experiment, in order to inhibit formation of PbF_2 (section 2.2.3). The addition of water to the tubes created a great increase in pressure upon heating, which frequently resulted in explosions. Larger tubes were necessary to accommodate the pressure, which created great expenses, inconveniences, and they still resulted in occasional explosions.

For these reasons, this study was not carried to completion. However, the few experimental results which were obtained are worthy of mentioning.

Figure 2.29 shows the IR results of decomposition experiments in the 400 - 900 cm^{-1} range. The complete spectra are compiled in appendix C. In the $Pb(fod)_2$ precursor spectrum, the major Pb-O transmittance peaks detected are located at 530, 594, and 630 cm^{-1}. These peaks are also present in the spectrum of $Pb(fod)_2$ decomposed for 30 minutes at 300 °C. The spectrum of the lead oxide standard has a large transmittance peak positioned at 594 cm^{-1}. Since this peak is present in both $Pb(fod)_2$ and PbO IR spectra, it appears to be the ligand-insensitive Pb-O transmittance. In the spectrum of $Pb(fod)_2$ decomposed at 350 °C for 30 minutes, the Pb-O transmittance peak at 594 cm^{-1} is no longer visible. However, a transmittance peak is emerging at 484 cm^{-1} in this spectrum. This Pb-O transmittance peak located at 484 cm^{-1} becomes more intense in the spectrum of products of $Pb(fod)_2$ decomposition for 30 minutes at 400 °C. An additional peak located at 728 cm^{-1} is present in the spectrum of $Pb(fod)_2$ decomposed at 400 °C for 30 minutes. The peaks located at 484 and 728 cm^{-1} are the most intense peak positions present in the PbF_2 standard.

Therefore, this study suggests that PbF_2 forms during thermal decomposition of $Pb(fod)_2$, even in the presence of water. Peak positions of the spectrum of $Pb(fod)_2$ decomposed at 300 °C for 30 minutes suggests initiation of PbO formation. Peak positions of the spectrum of $Pb(fod)_2$ decomposition at 350 °C for 30 minutes does not show the major Pb-O transmittance peak, but has a peak position which is indicative of initiation of PbF_2 formation. The spectrum of decomposition products at 400 °C for 30 minutes contains only Pb-F transmittance peaks, and no Pb-O trtansmittance peaks.

The KBr pellet method was used for these analyses, therefore the impurity peak position of 688 cm^{-1} (discussed in section 2.3.2.2) is also apparent in the PbO standard,

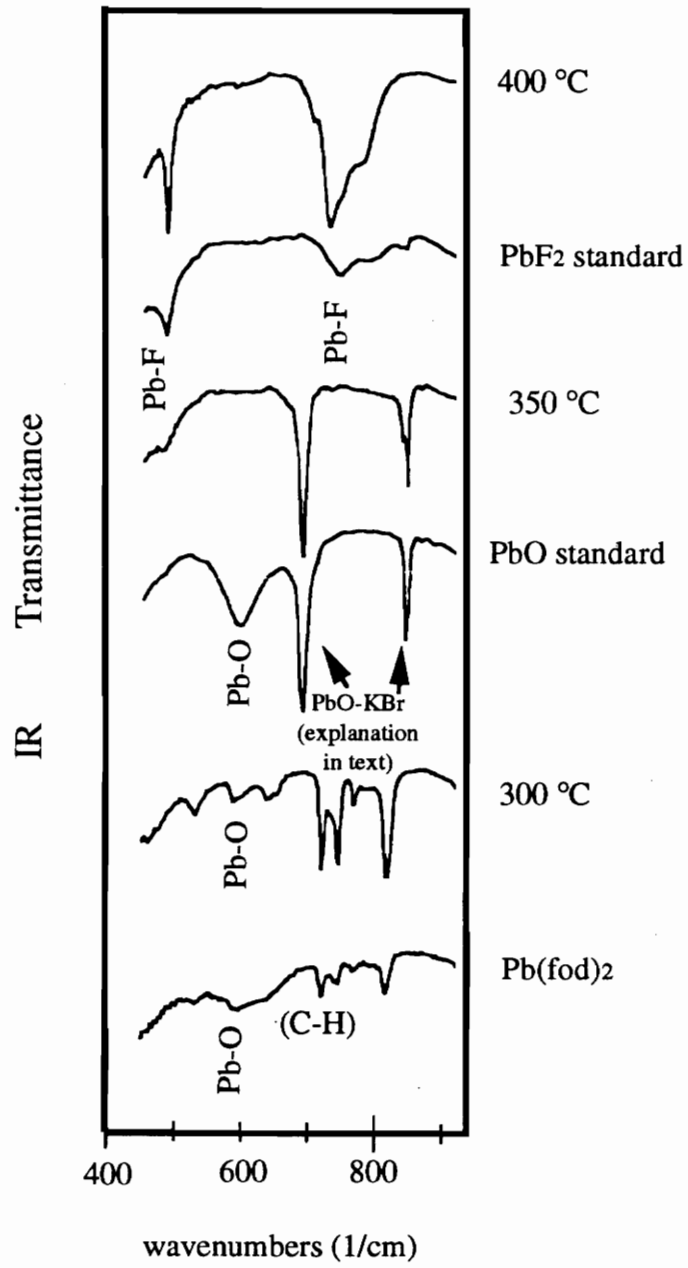

Figure 2.29 Infrared analysis of Pb(fod)2 decomposition (30 min)

and in the decomposition product spectra of 350 °C for 30 minutes. A sharp peak located around 800 cm^{-1} in the spectra of $Pb(fod)_2$ precursor, the PbO standard, and the decomposition products obtained at 300 °C and 350 °C is probably the product of reaction with the KBr, as well.

In summary of this section concerning $Pb(fod)_2$ decomposition, the formation of lead fluoride has been documented. Lead fluoride appears to be the dominant phase formed, as low as 350 °C. Additionally, the formation of lead fluoride took place, despite the fact there was stoichiometrically sufficient water to react with all the fluorine present.

2.4 Conclusions

In order to sufficiently summarize this chapter and justify its significance, the objectives (section 2.1) will be reiterated and addressed, individually. The first objective was to apply the synthesis and characterization studies of $Pb(fod)_2$, $Pb(thd)_2$ and $Zr(thd)_4$ toward an understanding of how these specific compounds behave as CVD precursors. First, all three precursors were synthesized with acceptable purity and reproducibility. Additionally, serendipitous development of a simple and versatile, novel method for lead β-diketonate synthesis was achieved. Difficulties with $Pb(fod)_2$, $Pb(thd)_2$ and $Zr(thd)_4$ syntheses were also noted. For instance, removal of excess ligand from the metal β-diketonate product was found to be a somewhat challenging process, which required some prudence in order to ensure purity. This problem was especially amplified in the case of $Pb(fod)_2$ synthesis, because the metal product is extremely soluble in the excess ligand. Another difficulty was the ambient instability of many of the zirconium compounds used as reactants for zirconium β-diketonate synthesis. For instance, the $Zr(acac)_4$ used for the metathesis synthesis had to be recrystallized and stored in a dry box. Understanding the issues of precursor synthesis are pertinent to the CVD process because: 1) Ease of

synthesis is necessary for efficient production of precursors so that they can be available for CVD on a regular basis (i.e. reproducibility is important). 2) Ease of purification is important so that the purity of precursor is consistent; this is important for consistency of CVD experiments. 3) Understanding how the precursor behaves during synthesis will give some clue of how it will behave during storage. This is important for CVD, because consistency of the experiments also depend on the ambient stability of the precursor.

Volatility experiments have provided some valuable information concerning use as $Pb(fod)_2$, $Pb(thd)_2$ and $Zr(thd)_4$ as CVD precursors. More importantly, a means of determining precursor vapor pressure was developed. Specific results pertaining to use of $Pb(fod)_2$, $Pb(thd)_2$ and $Zr(thd)_4$ as CVD precursors include: 1) Both $Pb(fod)_2$ and $Pb(thd)_2$ are not thermally stable above 120 °C; both undergo oligomerization which increases in rate with increasing temperature. 2) the duration of their thermal stability above 120 °C has been documented. 3) $Pb(thd)_2$ was found to have a slightly lower $\Delta Hvap$ (i.e it is easier to vaporize $Pb(thd)_2$ than $Pb(fod)_2$), when both precursors are above their respective melting points. 4) Oligomerization of $Pb(fod)_2$ occurs more quickly than $Pb(thd)_2$ above 120 °C. 5) $Zr(thd)_4$ is thermally stable over its range of vaporization temperature, and does not appear do undergo any oligomerization. 6) $Pb(fod)_2$ and $Pb(thd)_2$ exhibit vapor pressure of 0.2-600 torr over the range of 80-200 °C, and $Zr(thd)_4$ requires temperatures of 180-260 °C in order to exert equivalent vapor pressure.

These conclusions all provide data which is pertinent to use of these precursors for CVD. For instance, if equivalent vapor pressure of the zirconium and the lead precursor is required, the source temperatures can be chosen to control this parameter. The duration of lead precursor stability at various temperatures is also an important consideration when utilizing these precursors for CVD. Reproducibility of CVD experiments depends on consistent vapor pressure of precursors over the duration of the experiment.

More importantly, vapor pressures were determined from simple TGA experiments, and calculations derived from diffusion laws. This establishes a much simpler path to a quantification of precursor vapor pressure than physically measuring the vapor pressure. Measuring precursor vapor pressure is a very difficult pursuit which requires precise instrumentation and accurate temperature control (The difficulties of these experiments are demonstrated by Wolf et al.[22]).

The decomposition studies also provided some important points concerning use of $Pb(fod)_2$, $Pb(thd)_2$ and $Zr(thd)_4$ as CVD precursors. These include: 1) Onset and completion temperature of ZrO_2 formation from the $Zr(thd)_4$ precursor are 450 °C and 550 °C, respectively. 2) Onset and completion temperature of PbO formation from $Pb(thd)_2$ precursor are 250 °C and 350 °C, respectively. 3) PbO formation from thermal decomposition of $Pb(fod)_2$ precursor is initiated at 300 °C, but PbF_2 becomes the dominant phase above 300 °C. Additionally, an experimental method for decomposition studies of precursors was designed. These studies are important for the CVD process because the minimum decomposition temperatures required for each precursor is bracketed, and reduction of CVD deposition temperature is facilitated. These studies are also helpful in identifying precursors which would potentially result in growth of thin films with ligand impurities (i.e. $Pb(fod)_2$ is prone to PbF_2 formation).

In addition to addressing specific CVD precursor issues, this study has also initiated ideas for the development of novel precursors. Thermal instability of $Pb(fod)_2$ and $Pb(thd)_2$, and thermal stability of $Zr(thd)_4$ were related to the metal ions' respective coordination numbers. Oligomer formation of the lead β-diketonate precursors above 120 °C was hypothesized to provide a means of increasing coordination number on the metal center. Therefore, 6-9 coordinate novel precursors, consisting of lead β-diketonates with polyether adducts were proposed (described in detail in section 2.3.1.3).

The $Zr(thd)_4$ decomposition studies also provided a basis for novel precursor design. Formation of an intermediate product of thermal decomposition, which is closer to the final ZrO_2 structure than $Zr(thd)_4$, was documented (details in section 2.3.2.2). Isolation and characterization of this intermediate decomposition product might prove it to be a suitable precursor for ZrO_2 CVD. The intermediate structure has a potential advantage over $Zr(thd)_4$, in that the structure is closer to the final desired product. Therefore, lower deposition temperature might be achievable.

In summary, this study of lead and zirconium b-diketonate precursors for CVD has provided: 1) information concerning optimal use of $Pb(fod)_2$, $Pb(thd)_2$ and $Zr(thd)_4$ for CVD 2) a basis for studying precursor properties which are pertinent to the CVD process and 3) initiation of novel precursors design, which are engineered for optimal behavior under CVD conditions.

---

1 Sakashita, Yukio; Ono, Toshiyuki; and Segawa, Hideo, "Preparation and Electrical Properties of MOCVD-deposited PZT Thin Films", Journal of Applied Physics, 69, 12, (1991), pp 8352-8357.

2 Bradley, D.C.; Mehrotra, R.C.; Gaur, P.D. "Metal Alkoxides", Academic Press: (1978).

3 Mehrotra, R.C.; Bohra, R.; and Gaur, D.P., "Metal β-diketonates and Allied Derivatives", Academic Press, New York (1978), chapter 2.

4 R. Belcher; Cranley, C.R.; Majer, J.R.; Stephen, W.I and Uden, P.C., "Volatile Alkaline Earth Chelates of Fluorinated Alkanoylpivalylmethanes", Analytica Chimica Acta, 60 pp 109-116, (1972).

5 Fujinaga, Taitiro; Kuwamota, Tooru; Sugiura, Kenji; Matsubara, Norio, "Fundamental Investigation of Thermal Properties of Rare-Earth b-Diketonates", Talanta, 28, pp 295-300, (1981).

6 Fujinaga, T.; Kuwamota, T.; and Murai, S., "Gas Chromatography of Metal Chelates with Carrier Gas Containing Ligand Vapor", Analytica Chimica Acta, 71, pp 141-150, (1974).

7 Richardson, Mary Frances and Sievers, Robert E.; "Volatile Rare Earth Chelates of 1,1,1,5,5,5-Hexafluoro-2,4-pentanedione and 1,1,1,2,2,3,3,7,7,7-Decafluoro-4,6-heptanedione", Inorganic Chemistry, 10 (3), pp 498-504, (1971).

8 Desu, S.B.; Tian, S.; and Kwok, C.K., "Structure, Composition and Properties of MOCVD ZrO2 Thin Films", MRS Symposium Proceedings, 168 (1990), pp 349-356

9 Schweitzer, G.K., Pullen, B.P. and Fang, Y.H., "The volatilities of some lead b-diketonates", Analytica Chimica Acta, 43, pp 332-334, (1968)

10 Pinnavaia, Thomas J.; Mocella, Michael T.; Averill, Bruce A.; Woodward, John T. "Redistribution Reactions of d^0 Metal Diketonates Containing MO_6 and MO_8 Cores". Inoganic Chemistry, 12, [4], pp 763-768 (1973).

11 Sievers, R.E. and Connolly, J.W. "Tris (1,1,1,2,2,2,3,3-Heptafluoro-7,7-dimethyl-4,6-octadionato) Iron (III) and related complexes", Inorganic Synthesis, 12, XII, pp 72-76, (1969).

12 Belcher, R.; Majer, J.R.; Stehpen, W.I.; and Uden, P.C., "The gas chromatography thermal analysis and mass spectrometry of fluorinated lead b-diketonates", Analytica Chimica Acta, 50, pp 423 - 431, (1970).

13 Mason, T.J. and Lorimer, J.P., Sonochemistry, John Wiley & and Sons, New York, chapters 2 and 3, (1988).

14 Nyman, M. and Desu, S.B., "Synthesis and Characterization of Lead bis-heptafluorodimethyloctadione [Pb(fod)2] and its applications to MOCVD of PbO", Ceramic Transactions, 25, pp 219-234, (1991).

15 Nyman, M. and Seshu, S.B., "Volatility and Thermal Stability of Lead bis-heptafluorodimethyloctadione [Pb(fod)2] and Lead bis-tetramethylheptadione [Pb(thd)2] ", Mat. Res. Soc. Symp. Proc., 243 (1992).

16 Barron, Andrew. "Group IIA Metal-Organics as MOCVD precursors for High T_c Superconductors." The Strem chemiker, Vol. XIII, No 1, pp 1-9 (1990).

17 Geiger, G.H. and Poirier, D.R., "Transport Phenomena in Metallurgy", Addison-Wesley Publishing Company, (1973), chapter 2.

18 Silverton, J.V. and Hoard, J.L., "Stereochemistry of Discrete Eight-Coordination. II The Crystal and Molecular Structure of Zirconium(IV) Acetylacetonate", Inorganic Chemistry, 2 (2), (1963), pp 243-249.

19 Ewings, P.F.R; Harrison, P.G. and King, T.J., "Derivatives of Divalent Germanium, Tin and Lead. Part VI. Crystal and Molecular Structure of Bis(1-phenylbutane-1,3-dionato)tin(II)", Journal of the Chemical Society, Dalton, (1975), pp 1455-1458.

20 Bird, R.B.; Steward, W.E. and Lightfoot, E.N., "Transport Phenomena", John Wiley & Sons, (1960), chapter 1.

21 Wolf, W.R.; Sievers, R.E. and Brown, G.H., "Vapor Pressure Measurements and Gas Chromatographic Studies of the Solution Thermodynamics of Metal β-Diketonates", Inorganic Chemistry, 11(9), (1972), pp 1995-2002.

22 Fujinaga, Taitiro; Kuwamoto, Tooru; Sugiura, Kenji and Ichiki, Shigekazu, "Fundamental Investigation of Thermal Properties of Rare-Earth β-Diketonates", Talanta, 28, (1981), pp 295-300.

23 Reichert, C.; Bancroft, G.M.; and Westmore, J.B., "Mass spectral studies of metal chelates. V. Mass spectra and appearance potentials of some fluorine-substituted acetylacetonates", Canadian Journal of Chemistry, 48, (1970), pp 1363-1370.

24 Gardiner, R.; Brown, D.W. and Kirlin, P.S.; "Volatile Barium b-Diketonate Polyether Adducts. Synthesis, Characterization, and Metaloorganic Chemical Vapor Deposition, Chemistry of Materials, 3(6), (1991), pp 1053-1059.

25 Bradley, D.C. and Faktor, M.M., "The Pyrolysis of Metal Alkoxides", Journal of Applied Chemistry, (1959), pp 2117-2123.

26 Nakamoto, Kazuo, "Infrared Spectra of Inorganic and Coordination Compounds", John Wiley & Sons, New York, (1970).

27 Harima, Hiroshi ; Ohnishi, Hiroshi; Hanaoka,Ken-ichi; Tachibana, Kunihide; Goto, Yoshiyuki. "An IR Study on the Stability of $Y(DPM)_3$, $Ba(DPM)_2$ and $Cu(DPM)_2$ for UV radiation". Japanese Journal of Applied Physics, 30, [9A] pp 1946-1955 (1991).

28 Harima, Hiroshi ; Ohnishi, Hiroshi; Hanaoka,Ken-ichi; Tachibana, Kunihide; Kobayashi, Minoru; Hoshinouchi, Susumu. "Spectroscopic Study on a Discharge Plasma of MOCVD Source Gases for High-T_c Superconducting films", Japanese Journal of Applied Physics, 29, [10], pp 1932-1938 (1990).

29 Lawson, Katheryn, "The infrared absorption spectra of metal acetylacetonates", Spectrochimica Acta, 17 (1961), pp 248-258.

30 MacDonald, C.J. and Shannon, J.S., "Mass Spectrometry and Structures of Metal Acetylacetonate Vapours", Australian Journal of Chemistry, 19, pp 1545-1566, (2966).

31 Ueno, Keihei and Martell, Arthur E. "Infrared Study of Metal Chelates of Bisacetylacetone-Ethylenediimine and Related Compounds". 59, pp 998-1004 (1955).

32 Cotton, F.A.and Rice, G.W.; "The Crystal and Molecular Structure of Tetrameric bis (2,4-pentanedionato) Iron (II): an Unusual Iron-Carbon Interaction", Nouveau Journal de Chimie, 1 (4), pp 301-305, 1977.

33 " JCPDS Powder Diffraction File. Alphabetical Index of Inorganic Phases", JCPDS, (1985), p430.

34 Fischman, Gary S. and Petuskey, William T., "Thermodynamic Analysis and Kinetic Implications of Chemical Vapor Deposition of SiC from Si-C-Cl-H Gas Systems", Journal of the American Chemical Society, 68 [4], (1985), pp 185-190.

Chapter 3: T8-HYDRIDOSPHEROSILOXANE

3.1 Introduction

In this final chapter, synthesis and characterization of T8-hydridospherosiloxane, a novel precursor for CVD of silicon dioxide, will be presented. Hydridospherosiloxanes are cage-like polyhedra with the general formula $(HSiO_{1.5})_n$, where n = 8 - 20. The T8-hydridospherosiloxane (also referred to as T8) has the formula $(HSiO_{1.5})_8$, and an O_h symmetry (figure 1.1).

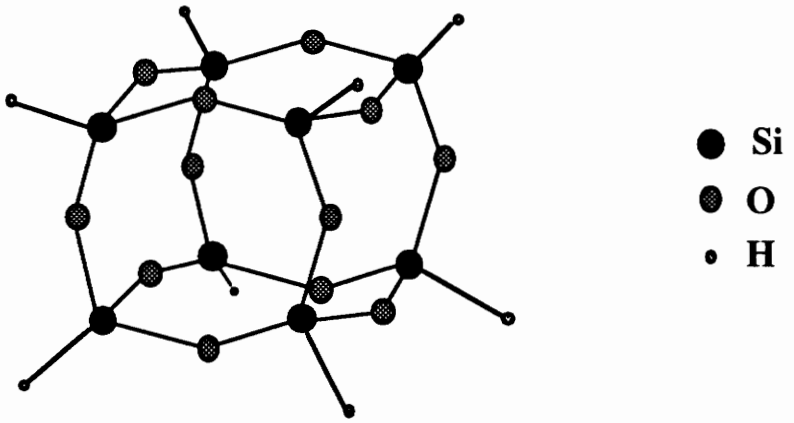

Figure 3.1 T_8-hydridospherosiloxane

Chemical vapor deposition of SiO_2 from hydridospherosiloxanes has not been reported, prior to the work reported by our research group.[1] Therefore, use of the hydridospherosiloxanes as CVD precursors is a novel approach. The first hydridospherosiloxane precursor used by our group for chemical vapor deposition of SiO_2 was a mixture of 64% T8 and 36% T10. The T10-hydridospherosiloxane has the formula

$(HSiO_{1.5})_{10}$ and D_{5h} symmetry. The T8 and T10 mixture was initially used for the novel SiO_2 CVD experiments because they are synthesized together via a reaction which produces a mixture, of 64% T8 and 36% T10 (explained further in section 3.2.1). [2] Therefore, the separation of T8 from T10 was eliminated from these initial CVD experiments.

Hydridospherosiloxanes possess several properties which enhance their suitability as SiO_2 precursors. Common precursors for CVD of SiO_2 thin films include tetraethoxysilane, diacetyl-di-t-butoxysilane and diethylsilane.[3] Silicon dioxide thin films deposited from these precursors via CVD contain carbon, due to the organic nature of the ligands. In contrast, hydridospherosiloxanes contain no carbon; therefore, no potential exists for carbon contamination in the SiO_2 films deposited from these precursors. The hydridospherosiloxanes are stable under ambient conditions, nontoxic and nonpyrophoric. Additionally, they exhibit vapor pressures at low temperatures; T8 sublimes at 32.5 °C and T10 sublimes at 35 °C in vacuo (0.01 torr).

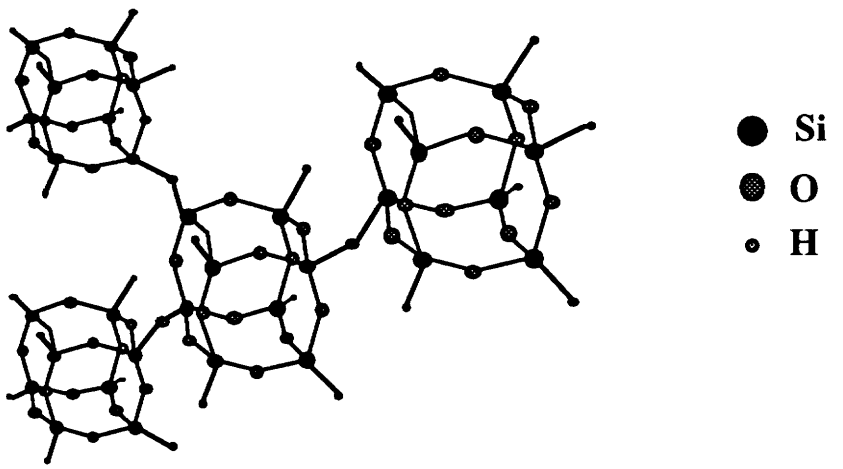

Figure 3.2 T8 units as SiO_2 building blocks

A very intriguing property of the hydridospherosiloxanes is the Si-O-Si framework structure of the polyhedral units. Potentially, the SiO_2 framework can be built up by simply replacing each Si-H bond with an Si-O bond, and bridging each of these oxygens to an adjacent polyhedral unit. This mechanism is demonstrated in figure 3.2 for T8, the hydridospherosiloxane which is the focus of this study. One interesting feature of this mechanism is the Si-O-Si bond angle in the resulting SiO_2 thin film should vary as a function of the Si-O-Si bond angle of the hydridospherosiloxane precursor. The Si-O-Si bond angle of the hydridospherosiloxanes increases with increasing size of n For instance, T8 has a smaller Si-O-Si bond angle than T10. This proposed pathway of SiO_2 formation from hydridospherosiloxanes would not require high formation temperatures, because the Si-H bond is weak, relative to the Si-O bond.

The volatility, ambient stability, nontoxicity, the lack of organic ligands, and potentially simple, low temperature mechanism of thermal decomposition to SiO_2 renders the hydridospherosiloxanes a highly viable class of silicon dioxide precursors.
The objectives of the work presented in this chapter is to characterize the properties of T8 which are pertinent to the CVD process such as volatility, thermal stability, and temperature of SiO_2 formation, and to obtain spectrometric evidence for the proposed decomposition mechanism. Steps of the experiments are as follows: 1) synthesize and isolate pure T8 2) examine the thermal stability of T8 and quantify its volatility (i.e. vapor pressure and enthalpy of vaporization) by isothermal gravimetric experiments 3) execute decomposition experiments and examine the decomposition products by ^{29}Si solid state NMR and infrared spectrometry.

Although a mixture of T8 and T10 was used for the initial CVD deposition of SiO_2 from hydridospherosiloxanes[1], the individual hydridospherosiloxanes must be studied separately to determine their properties. The T8 was chosen for the initial study, and other

hydridospherosiloxanes of increasing polyhedra size will be examined in the future. This study was carried out to initiate the series of experiments of the hydridospherosiloxane family of compounds, and to establish a base for these future experiments.

3.2 Experimental

3.2.1 Synthesis and purification of T8

The T8 and T10 hydridospherosiloxanes were synthesized together using a method developed by P. A. Agaskar.[2] The synthesis apparatus is demonstrated schematically in figure 3.3. A hydrous phase consisting of 20 ml hydrochloric acid, 3 grams dodecyl sulfate sodium (Aldrich catalog #85,192), 100 grams anhydrous ferric chloride (Aldrich catalog #15,774) and 80 ml methanol, and an anhydrous phase of 800 ml pentane were vigorously stirred in a three-neck, 3000 ml Morton-type flask (purchased from Kontes). The stirring apparatus consists of a 10 mm teflon shaft (Ace glass # 8071); multi-paddle, teflon agitator (Ace glass #8089); and a Talboys 40 watt (500-7500 rpm) stirring motor. A mixture of 400 ml pentane and 40 ml trichlorosilane (Petrarch catalog #100,613) was dripped slowly (over 5 hours) from a platinum-needle dropper flask. The reaction mechanism involves a slow hydration of the trichlorosilane. The salt (dodecyl sulfate sodium) acts as a surfactant which binds the water to the ferric chloride; this allows a slow release of the water so that the trichlorosilane is hydrated gradually.

After complete reaction of the trichlorosilane (5 hours), a crystalline, pentane-soluble mixture of 36% T10 and 64% T8, and a polymer phase is dissolved in the pentane layer. Additionally, a white, insoluble byproduct, which is isochemical with T8 and T10 is synthesized. The contents of the flask are siphoned into a large separatory funnel (2000 ml), and allowed to settle into layers; the dark green hydrous phase (containing the ferric

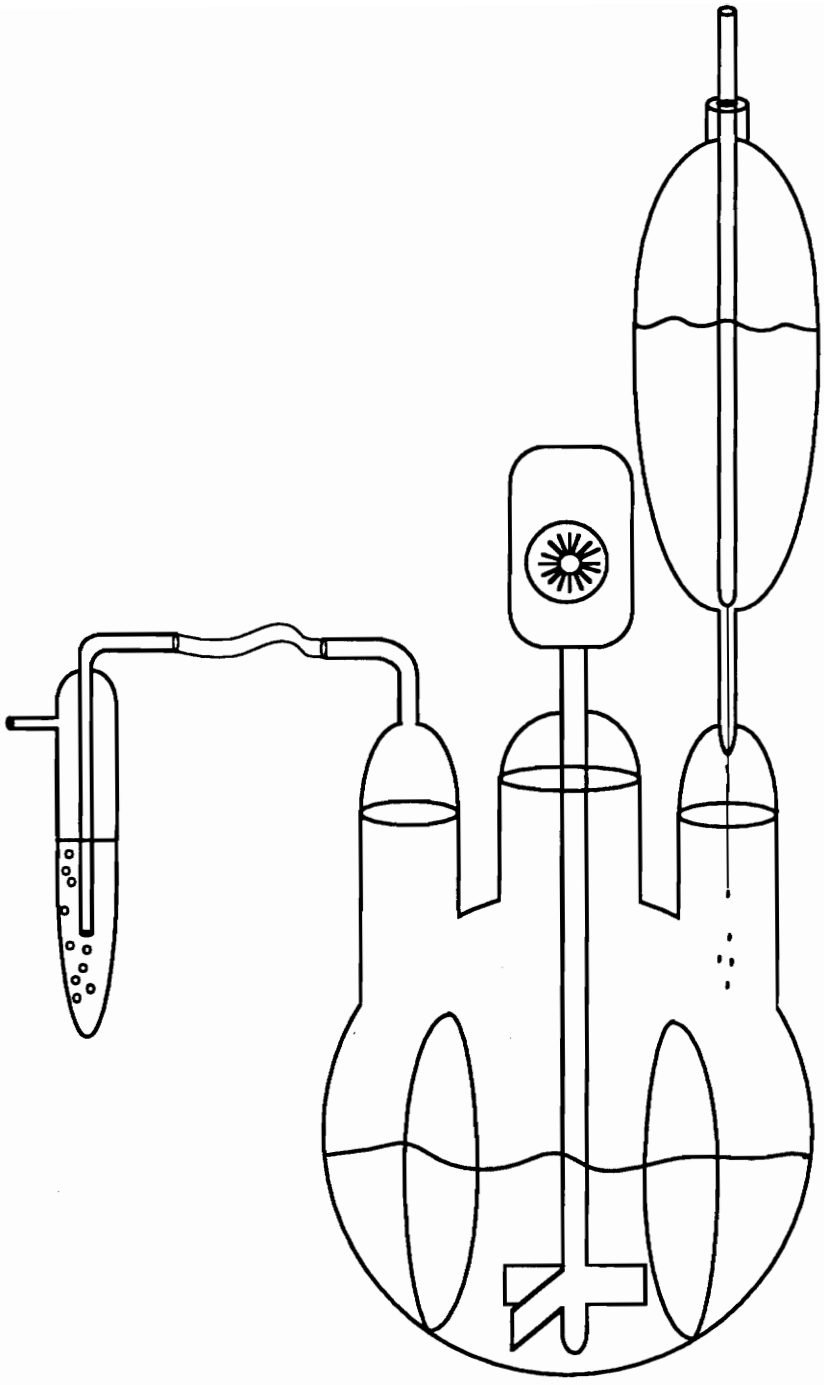

Figure 3.3 T8/T10-hydridospherosiloxane synthesis apparatus

chloride) is on the bottom, topped by the insoluble white byproduct, and the pentane with dissolved T8/T10 and polymer product is on top. The dark green ferric chloride layer is returned to the flask (discussed later), the insoluble byproduct is discarded, and the pentane layer containing T8/T10 and the polymer is added to a second, large (2000 ml) round bottom flask which contains a magnetic stir bar and 28 grams K_2CO_3. The pentane containing the dissolved products is stirred overnight with the potassium carbonate, in order to remove excess water and HCl.

The potassium carbonate is then removed from the pentane mixture by filtering through a fine fritted, large capacity (at least 300 ml) glass filter. Potassium carbonate is layered atop the frit as a filter bed. Excess pentane can be added for complete filtering during this step, if necessary. It is important to keep the filter covered during filtering to avoid evaporation of the pentane, and subsequent crystallization of T8 and T10 on the filter bed. This step also removes any excess insoluble, isochemical product. The pentane solution is then transferred to a large beaker, and the pentane is evaporated to yield a mixture of 64% T8 and 36% T10, and the polymer. After this step, the product is a yellow polymer matrix with abundant, white, needle-like crystals, which is the T8 and T10. Fifty ml pentane is added to the mixture, which dissolves the polymer, and is pulled off with a pipet. This step is done twice. The next step is to remove the T10 from the T8/T10 mixture, so that the T8 can be studied separately. The solubility of T10 in pentane is 150 mg/10 ml, and the solubility of T8 in pentane is 60 mg/10 ml. For each washing, 15 ml pentane is added to the T8/T10 mixture, the mixture is agitated with a spatula, 10 ml pentane is pulled off with a pipet, and the remaining 5 ml is left to evaporate. The sample is weighed before and after adding the pentane. After the initial pentane washings, there should be a weight loss of 0.21 grams (0.15 grams T8 and 0.06 grams T10). The process is repeated until there is 0.06 gram weight loss (only T8).

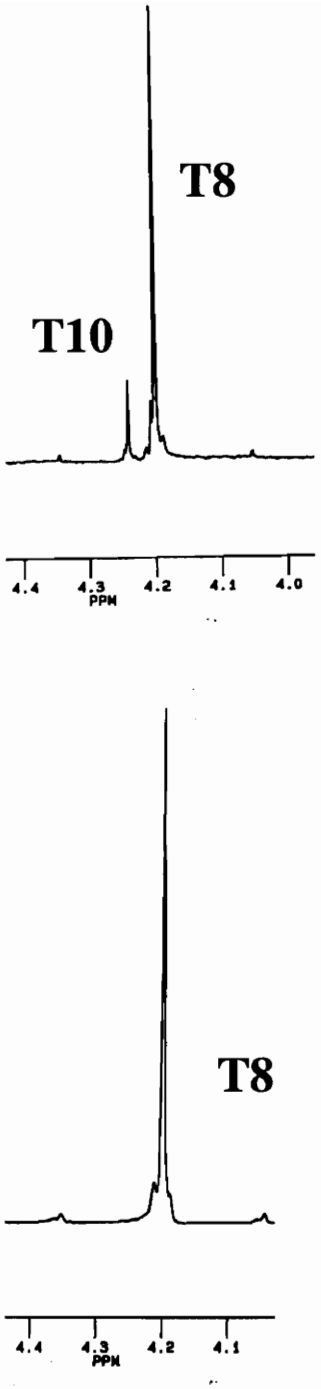

Figure 3.4 Proton NMR of T8 and T10 (top) and Proton NMR of T8 (bottom)

Separation of T8 from T10 was confirmed by proton nuclear magnetic resonance spectrometry (figure 3.4). Proton NMR spectra were obtained from a Bruker 200 instrument with a 5 mm probe. Samples were dissolved in deuterated benzene, and referenced to tetramethyl silane at 0 ppm (Hz/MHz operating frequency). The T8 peak is located at 4.203 ppm, and the T10 peak is located at 4.244 ppm in D-6 benzene. Purity of T8 was confirmed by the absence of the T10 peak. Final T8-hydridospherosiloxane product is a volatile, white crystalline solid (m.p. >300 °C) of 17.5% yield from trichlorosilane.

The ferric chloride which is returned to the reaction flask from the separatory funnel can be reused for 2 to 3 reactions. If the ferric chloride is reused, then 10 ml hydrochloric acid and 800 ml pentane are added to the reaction flask, and the remaining procedure is the same as described above.

3.2.2 Volatility Experiments

Isothermal gravimetric analyses (TGA) were carried out to calculate the vapor pressure of T8 at vaporization temperatures, and examine the thermal stability. The experimental procedure used is the same which is described in section 2.2.2 for the lead and zirconium β-diketonates. Temperatures and time for isothermal experiments were 80, 100, 120, and 140 °C for 250 minutes. The sample size of T8 was kept constant at 1.0 mg. The carrier gas was dry N_2 with a purge rate of 25 ml/min. Dry nitrogen was chosen so that any reactions of T8 with water or oxygen would be eliminated. The N_2 purge rate and sample size were kept constant so that diffusion rate laws could be employed to convert weight loss data generated by TGA experiments to vapor pressures of T8 at the various experimental temperatures. The N_2 purge rate was chosen so that the diffusion of T8 through the boundary layer at the solid-vapor interface was the rate limiting step, rather

than the removal of T8 from the boundary layer by the carrier gas. This was confirmed by duplicating the experiments at a doubled flow rate, and observing no increase in vaporization rate of the T8. If removal of T8 were the rate controlling step, the vaporization rate would increase proportionally (details described in section 2.3.1.1).

3.2.3 Decomposition Experiments

Decomposition studies involved the formation of SiO_2 from T8-hydridospherosiloxane in a closed system, under a fixed set of parameters, over a range of decomposition temperatures. Decomposition temperatures and pathways were studied via examination of the decomposition products by ^{29}Si NMR and Fourrier Transform Infrared Spectrometry (FTIR). A 0.1 liter quartz cylinder containing 0.2 g T8 (0.5 mmol) was evacuated and backfilled with 425 torr O_2 gas (2.5 mmol), and sealed with an oxygen-propane torch (see figure 2.9). This "quartz bomb" was heated for 30 minutes at decomposition temperature. Decomposition temperatures were 250, 300, 350, and 400 °C. The most thermodynamically favored decomposition reaction of T8 in the presence of oxygen would involve the formation of water, and is proposed as follows:

$$H_8Si_8O_{12} + 4O_2 \xrightarrow{\Delta} 8SiO_2 + 4H_20 \qquad (3.1)$$

This implies that the oxidizing source (O_2) is present in 25% excess; therefore decomposition is not inhibited by lack of oxygen.

Products of T8 decomposition were examined by infrared analyses in the mid-IR range (400-5000 wavenumbers). The details of these spectrometry experiments are described in section 2.2.3. Samples for IR analysis were prepared by: 1) mixing T8 decomposition products with 0.5-1.0 grams spectroscopic grade KBr in a weight ratio of 1:

200 in an acetone medium 2) drying 0.3 grams of the KBr/sample mixture in an oven at 140 °C 3) pressing the powder into pellets using a 12 mm die (25,000 lbs for 5 minutes). The moisture-absorbing KBr pellets were stored in a desiccator until analyses were executed.

Solid state ^{29}Si nuclear magnetic resonance spectrometry was also used to examine the T8 decomposition products. The ^{29}Si (4.7% natural abundance) nuclear magnetic resonance spectra were obtained from a Bruker MSL 300 operated at 59.601 MHz for silicon . (90° pulse time [D1] = 3 μs, recycle delay [D0] = 8 sec). Solid samples of decomposition products were packed in a 4mm ZrO_2 rotor and spun at 3.5 KHz at the 'magic angle' (54.73 °). Other parameters included ; 90° pulse time [D1] = 3 μs, recycle delay [D0] = 8 sec. The T8 peak is enhanced by decoupling of the proton at the apex of the silicon. Because there was a small amount of decomposition product from each experiment, excess space in the rotor was pack with KBr. Peak shifts are recorded in ppm (Hz/MHz operating frequency), and referenced to tetramethyl silane (TMS) at 0 ppm. Upon transforming the FID's, line broadening of 100 Hz was necessary to distinguish the small, broad signals from the noise. The ^{29}Si magic angle spinning spectrum of T8 precursor was obtained from a 7 mm probe; therefore, samples were packed in a 7 mm rotor. Cross polarization was used for signal enhancement. Parameters included; recycle delay [D0] = 15 sec., 90 ° pulse time [D11] = 4.45 μs, aquisition time [D7] = 120 msec., and contact time [D5] = 5 msec.

3.3 Results and Discussion

3.3.1 Volatility and Thermal Stability

Figure 3.5 illustrates the T8 isotherms of the TGA experiments. Experiments carried out at 120 °C and 140 °C show constant weight loss and complete evaporation of the sample in approximately 85 and 12 minutes, respectively. No T8 precursor was visible in the sample pan after completion of the TGA experiments executed at 120 and 140 °C. The TGA experiments executed at 80 and 100 °C also show constant weight loss over 250 minutes, but the evaporation rate was not fast enough to obtain complete evaporation of the sample within the time of the experiment. However, the weight loss is constant with no break in slope. The unevaporated T8 remaining in the sample pan after completion of the TGA experiments executed at 80 and 100 °C was a white crystalline solid. Its appearance is not altered, which suggests no decomposition has taken place during these experiments. The constant rates of weight loss for TGA experiments at 80, 100, 120, and 140 °C, no breaks in isothermic slopes, and unaltered appearance of T8 precursor which did not evaporate at 80 and 100 °C suggest T8 is stable over the time and temperature range of the TGA experiments.

The T8 vapor pressures at vaporization temperatures were calculated from the isothermal gravimetric experiments in the same manner that the metal β-diketonates vapor pressures were calculated. The justifications for using diffusion laws to convert weight loss data to vapor pressures are discussed in section 2.3.1.1. Equation 2.9 was used to calculate diffusion coefficient of the vapor phase, diffusing T8 molecule, and equation 2.8 converts the weight loss data to vapor pressures. These equations are also described in detail in section 2.3.1.1. In order to use the TGA data to convert weight loss to vapor pressure, the (%weight loss/Δtime) has to be converted to (Δweight/Δtime). These values,

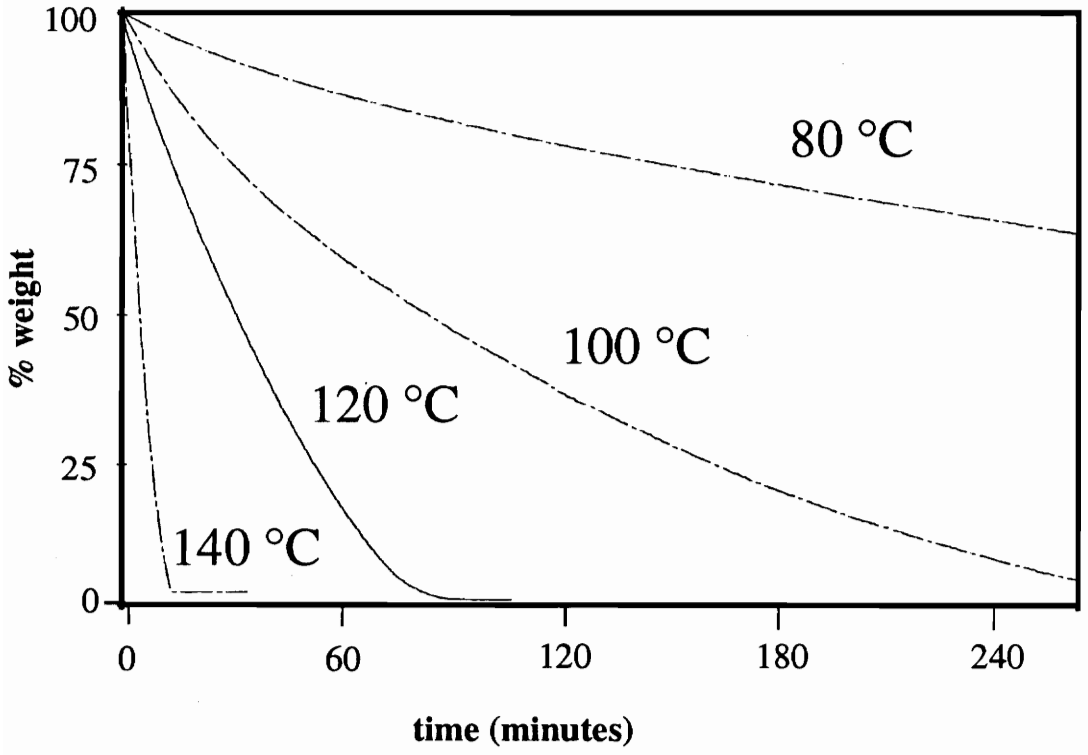

Figure 3.5 T8-Hydridospherosiloxane isotherms

Table 3.1 T8-hydridospherosiloxane weight loss data ($\Delta m/\Delta t$)

Temperature (°C)	weight loss/time mg/min
80	0.00297
100	0.00913
120	0.0356
140	0.117

Table 3.2
Parameters for diffusion controlled vapor pressure calculations for T8-hydridospherosiloxane

approximate diameter of molecule (angstroms) (l)	5.68 angstroms
mol weight (g/mol)	424 g/mol
diffusion coefficient) (D)	1.90 cm^2/sec
dynamic viscosity of carrier gas (η)	2.0×10^{-4} g/cm sec
mean free path of carrier gas (λ)	7.5×10^{-6} cm
area of precursor evaporation surface (S)	0.126 cm^2
boundary layer thickness (d)	0.19 cm

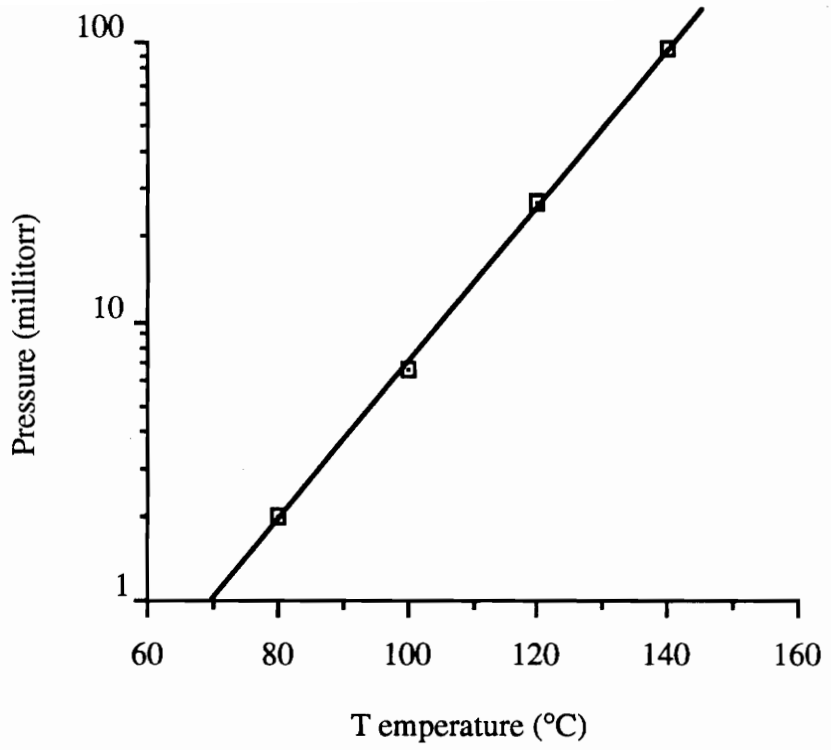

Figure 3.6
Calculated vapor pressure of T8-Hydridospherosiloxane
as a function of temperature

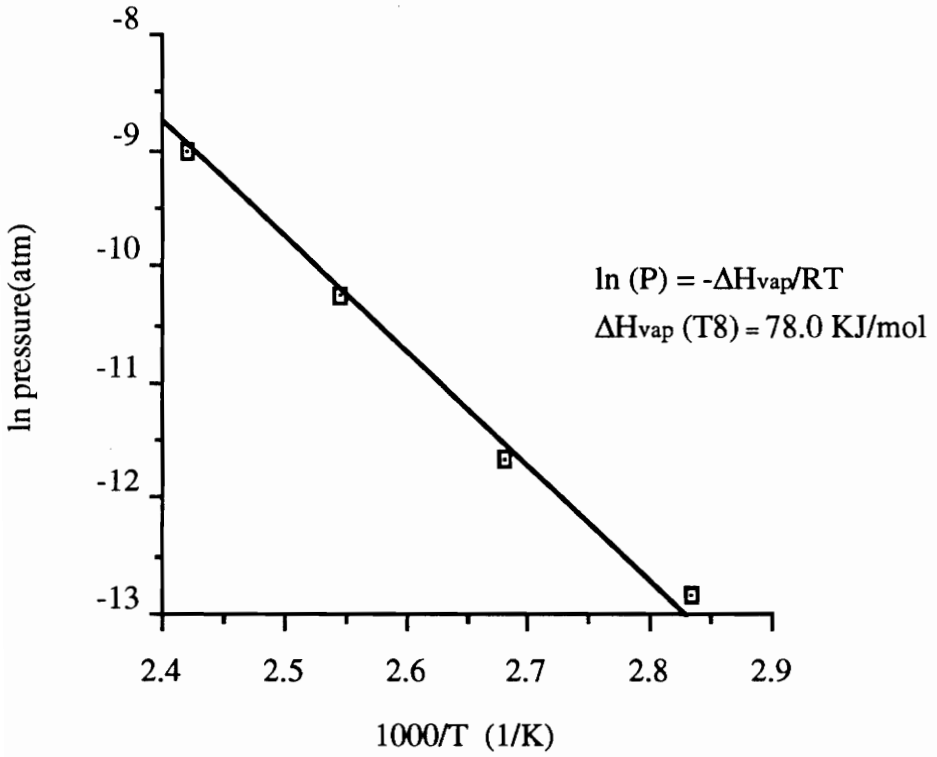

Figure 3.7
Ahrrenius plot of T8 vapor pressure as a function of temperature

and other parameter values necessary to calculate T8 vapor pressure from the TGA data from equations 2.8 and 2.9 are presented in tables 3.1 and 3.2. The approximate size of the diffusing T8 molecule (l) was estimated using reported X-ray data of bond lengths and bond angles within the hydridospherosiloxane precursor.[4]

Vapor pressures calculated from the diffusion equations are plotted as a function of vaporization temperature in figure 3.6. Vapor pressures range from 2 to 100 millitorr over the temperature range of 80-140 °C. An enthalpy of vaporization of 78 KJ/mol was calculated from the Ahrrenius plot of vapor pressure as a function of temperature (figure 3.7).

3.3.2 Decomposition Experiments

Infrared spectra of T8 precursor, and T8 heated at 250, 300, and 350 °C in sealed quartz tubes for 30 minutes each, are shown in figure 3.8. According to the infrared spectra, there is little difference between the in IR transmittance of T8 bonds and the amorphous silica bonds. Therefore, it is important to distinguish which infrared transmittance bands are characteristic of T8, silica, or both T8 and silica. The T8 precursor spectrum was interpreted with reference to infrared absorption data of organosilicon compounds compiled by Launer [5]. A broad transmittance peak located at 1100-1250 cm^{-1} (wavenumbers) is identified as the Si-O-Si transmittance of a polysiloxane $[RSiO_{1.5}]_x$. Therefore, this peak is identified as the Si-O-Si transmittance of the T8 precursor. The transmittance peaks located at 850 cm^{-1} and 950 cm^{-1} on the lower wavenumber shoulder of the Si-O-Si band are identified as the Si-H bond of the T8 polyhedral unit. The small transmittance peak at 2280 cm^{-1} is also characteristic of the Si-H bond. Launer reports locations of amorphous silicon dioxide transmittance peaks at 1080 -1110 cm^{-1}, and 800-810 cm^{-1}. Lucovsky et al. [6] also report locations of infrared silica transmissions. These

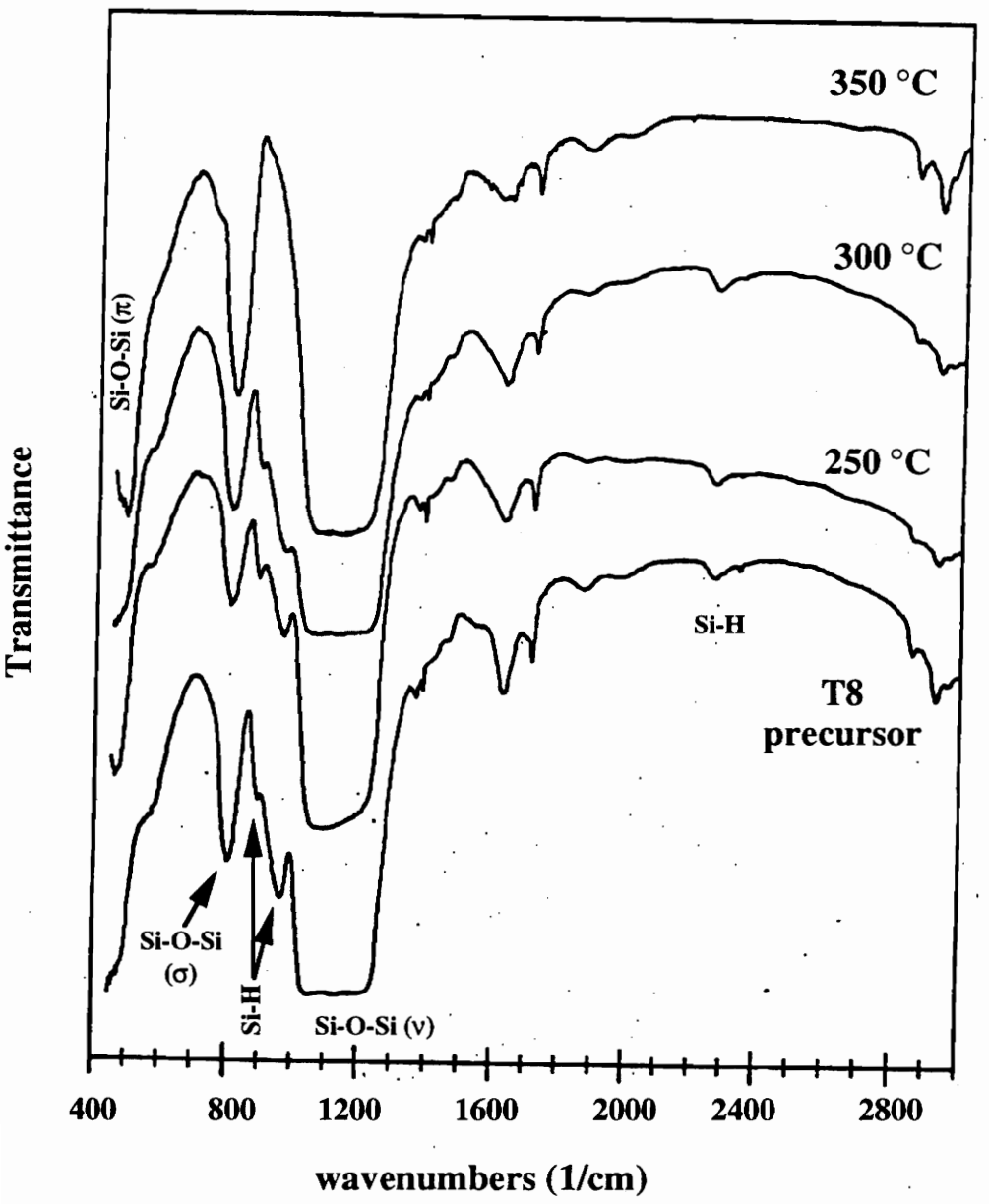

Figure 3.8 IR spectra of T8 precursor and decomposition products (30 minute decomposition time)

include the Si-O-Si out of plane rocking (π) mode located at 450 cm^{-1}, the Si-O-Si in-plane bending (σ) mode located at 810 cm^{-1} , and the Si-O-Si stretching (ν) mode located at 1060 cm^{-1}.

Since the Si-H transmissions are unique to the T8 precursor, they are used as fingerprint peaks to determine the completion temperature of silica formation. The characteristic Si-H peak positions at 850 cm^{-1}, 950 cm^{-1} and 2280 cm^{-1} are labeled in figure 3.8. The transmittance peaks at 850 cm^{-1} and 950 cm^{-1} exhibit decreased intensity in spectrum of decomposition products at 300 °C. None of the three characteristic transmittance bands of Si-H bonds are observable in the products of decomposition at 350 °C. Additionally, the relatively sharp Si-O-Si transmittance band at 810 cm^{-1} (bending) increases in intensity with increasing decomposition temperature. The rocking transmittance of the Si-O-Si structure (450 cm^{-1}) is first apparent in the products of decomposition at 350 °C. The transmittance band at 1100-1250 cm^{-1}, which was identified as the Si-O-Si absorption for both the T8 precursor and the amorphous silica, exhibits very little shift or change in shape from the T8 precursor to the decomposition products at 350 °C.

Completion of T8 decomposition to silica at 350 °C is apparent by the disappearance of the Si-H transmittance bands in the infrared spectra. Consistency in shape and the position of the Si-O-Si transmittance band in the T8 precursor, and products from T8 decomposition at 250, 300, and 350 °C gives evidence for the proposed decomposition mechanism of maintaining the framework structure of the T8 polyhedra in the silica decomposition products.

In order to confirm the completion temperature of silica formation from T8 precursor, and to bracket a decomposition onset temperature, the decomposition products were examined via ^{29}Si NMR spectrometry. The ^{29}Si spectrum of T8 precursor is shown

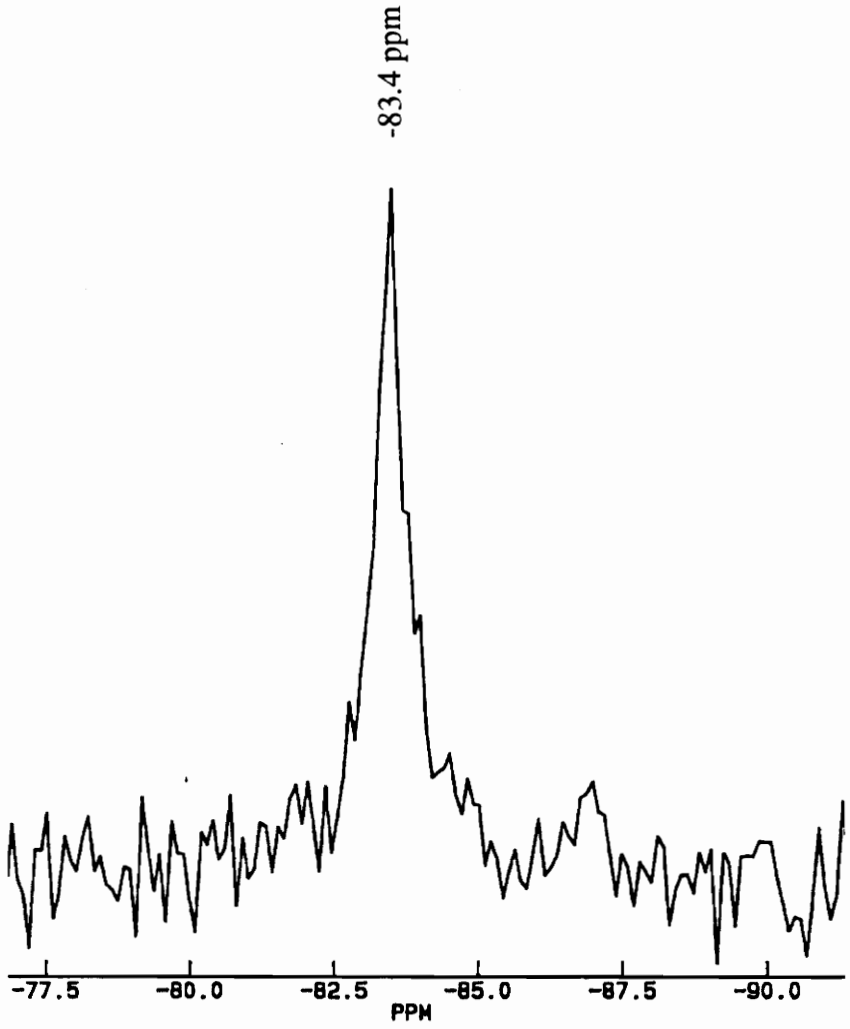

Figure 3.9
CP-MAS ^{29}Si spectra of T8-hydridospherosiloxane precursor

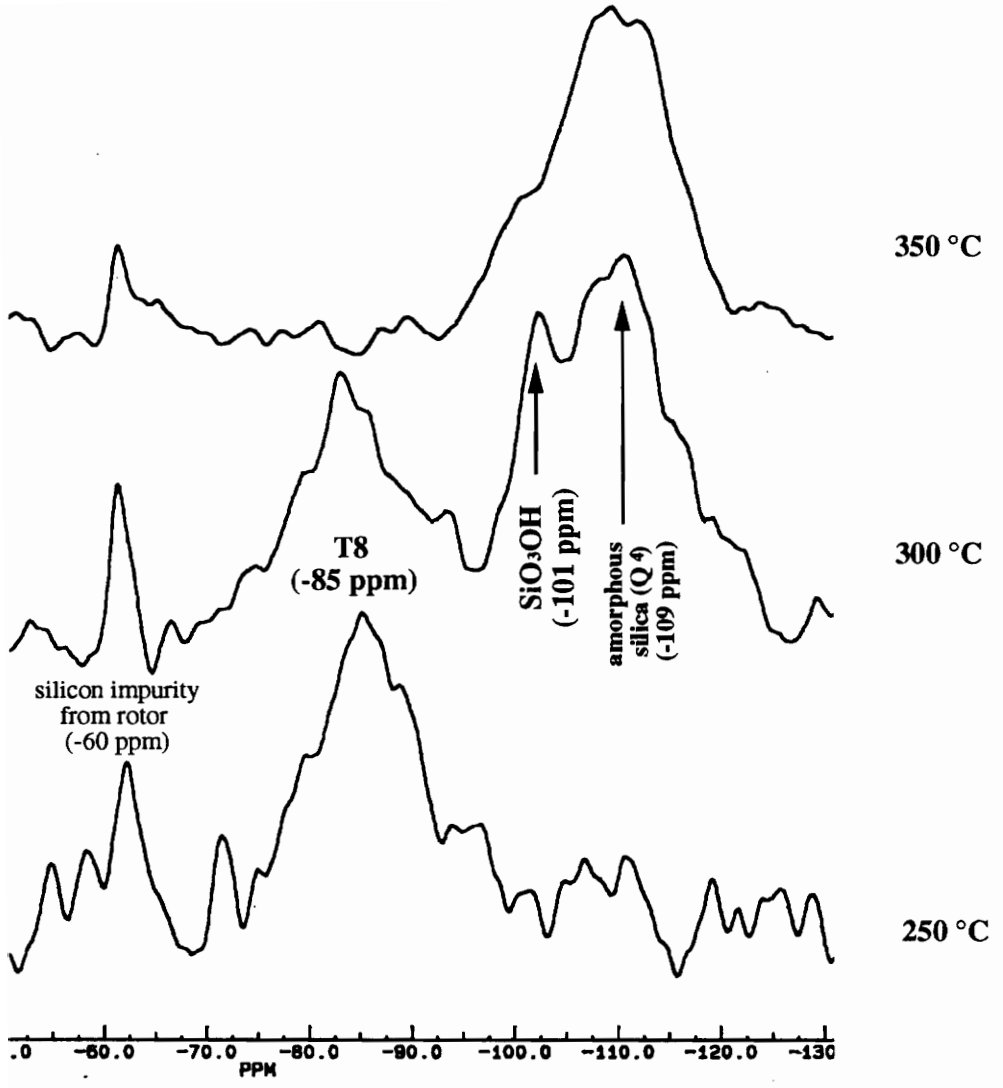

Figure 3.10
MAS ^{29} Si NMR spectra of T8 decomposition products

in figure 3.9. The spectrum consists of a single, sharp peak at -83.4 ppm. The narrowness of the peak is enhanced by cross polarization of the protons at the apex of the silicon tetrahedra within the T8 polyhedra. The ^{29}Si spectra of decomposition products of T8 heated for 30 min in an O_2 environment (25% excess with H_2O as a byproduct) at 250 °C, 300 °C and 350 °C are shown in figure 3.10. The peak located at -60 ppm is a silicon impurity in the ZrO_2 rotor. This was confirmed by running a spectra of the rotor, packed only with KBr.

The ^{29}Si NMR spectrum of T8 decomposed at 250 °C for 30 minutes consists of a single, broad peak at -85 ppm. Distinct environments of SiO_4 tetrahedra are generally referred to as Q^0, Q^1, Q^2, Q^3, and Q^4, where the superscript represents the number of corners the SiO_4 tetrahedron shares with neighboring SiO4 tetrahedra.[7] The silicon tetrahedra in the SiO_2 framework are designated the Q^4 environment. Lippmaa et al.[8] reported a ^{29}Si chemical shift of -109 ppm ($\pm$2 ppm) of silicon in the Q^4 environment, with reference to TMS. This value is in agreement with the peak which was first observed in the spectrum of decomposition products obtained at 300 °C. Onset of T8 decomposition to SiO_2 takes place between 250-300 °C, as inferred by the ^{29}Si NMR spectra. The SiO_2 peak at -109 ppm is not apparent in the spectrum of T8 decomposition products at 250 °C, and is initially observed in the spectrum of T8 decomposition products at 300 °C. The disappearance of the T8 peak in the ^{29}Si NMR spectra of T8 decomposition products confirms the IR evidence for completion of T8 decomposition to silica at 350 °C.

The broadening and slight shift of the T8 peak in the decomposition spectra can be explained by several means. Since the T8 peak is broadened upon decomposition at 250 °C, some decomposition is likely to have been initiated. In other words, several T8 units are likely to be linked together by Si-O-Si bridges, which would increase the average size and distribution of the polyhedral unit. Increase in size of the polyhedral unit results in

decreased freedom of rotation in the solid state, magic angle spinning NMR experiment. Therefore, the T8 peak is broadened. Because decomposition has been initiated at 250 °C, the Q^4 silicon peak at -109 ppm should also be present in the ^{29}Si spectrum of decomposition at 250 °C. However, if the Q^4 silicon is present in small concentration, it is likely to be buried in the noise of the spectrum. Since the Q^4 silicon has no protons, the signal at -109 ppm is not enhanced by the decoupling effect. The shift of 1.6 ppm of the T8 peak in the decomposition product spectra is a consequence of the broadening, which is explained above.

In addition to confirming the decomposition temperature range of T8 to SiO_2, the ^{29}Si NMR spectra also provided information pertaining to the mechanisms of decomposition. A possible mechanism for decomposition reaction is as follows:

$$2 \equiv Si\text{-}H + O_2 \longrightarrow 2 \equiv Si\text{-}OH \qquad (3.2)$$

$$2 \equiv Si\text{-}OH \longrightarrow \equiv Si\text{-}O\text{-}Si \equiv + H_2O \qquad (3.3)$$

An oxygen atom from the diatomic oxygen is inserted into the Si-H bond. The gas phase silicic acid formed by the insertion reaction is involatile, and therefore would condense on the substrate. Condensation reactions would then complete the decomposition to SiO_2. This reaction has been demonstrated in polar solvents using $Me_3NOSiMe_3Cl$ as an oxidizing source, where the polysiloxane unit is preserved in the SiO_2 framework.[9] If the silicic acid intermediate specie is formed, the Si-OH bond should be observable in the partially decomposed T8 products, such as those formed at 300 °C for 30 minutes. In addition to the T8 peak at -85 ppm and the SiO_2 peak at -109 ppm, the ^{29}Si spectrum of T8 decomposed for 30 minutes at 300 °C has an additional peak at -101 ppm. Due to the proximity of this peak to the SiO_2 peak, the two peaks appears a single peak which is split.

Aujla et al.[10] identify this peak position as $SiO_3(OH)$. The ^{29}Si spectra for decomposition products of T8 at 350 C for 30 min shows a SiO_2 peak at -110 ppm with a just a shoulder at the position of $SiO_3(OH)$ (-101 ppm).

3.4 Conclusions

The objective of this study concerning synthesis and characterization of T8-hydridospherosiloxane was to examine its volatility and thermal stability properties, and relate these to its suitability as a precursor for CVD of SiO_2. It was interpreted from isothermal gravimetric experiments that T8 is volatile and thermally stable at vaporization temperatures of 80-140 °C. Thermal stability is apparent from the constant slope of the isotherms, complete evaporation of the 1 mg T8 sample at higher temperatures (120-140 °C) over the time period of the experiment (250 minutes), and no observed decomposition of the T8 samples remaining in the sample pan after 250 minutes for experiments executed at 80 and 100 °C. Diffusion equations were used to calculate vapor pressure at vaporization temperatures from the TGA weight loss data. Calculated vapor pressures range from 2 - 100 millitorr over the 80-140 °C temperature range. The enthalpy of vaporization (sublimation) of T8 was calculated from the Ahrrenius relationship between vaporization temperature and vapor pressure. Calculated enthalpy value is 78 KJ/mol, which is comparable with enthalpy of vaporization of the lead β-diketonate precursors, above their melting points (section 2.3.1.1).

Onset and completion temperatures (300 °C, and 350 °C) of T8 decomposition to SiO_2 were determined by IR spectrometry and ^{29}Si NMR spectrometry. Additionally, the ^{29}Si NMR spectra provide some evidence for the intermediate reaction of oxygen insertion into the Si-H bond. The proposed mechanism of preservation of the Si-O-Si framework

structure of the T8 polyhedra during decomposition to SiO_2 (figure 3.2) is supported by the following interpretations.

The temperature range of decomposition bracketed by the onset and completion temperatures is only a 50 °C span (300-350 °C). Decomposition of the lead and zirconium β-diketonates took place over a 100 °C span (section 2.3.2). This suggests decomposition of T8 to silicon dioxide involves fewer intermediate steps, and is less complex than the decomposition of lead and zirconium β-diketonates to their respective oxides. The proposed decomposition pathway of replacing Si-H bonds with bridging Si-O-Si bonds is a reasonable means of obtaining amorphous silica from T8 over a short temperature range. More evidence for preservation of the Si-O-Si framework in the SiO_2 formed from T8 is the low formation temperature. The Si-H bond (299 KJ/mol dissociation energy) is weak relative to the Si-O bond (799 KJ/mol dissociation energy), and it is not likely that dissociation of the silicon-oxygen framework of the T8 polyhedra could take place under the conditions of the decomposition experiments. (Bond energies from CRC Handbook[11]).

Evidence for proposed insertion mechanism is perceived through detection of the SiO_3OH intermediate by ^{29}Si NMR. The ^{29}Si NMR spectra also provide further evidence for the integrity of the Si-O-Si framework of T8. If SiO_2 formation was initiated by replacing all the T8 Si-O bonds with Si-OH bonds, then $SiO_2(OH)_2$ would also be observed at -91 ppm [9] in spectra of intermediate decomposition (i.e. 300 °C). Additionally, the quartz tubes used for the decompositon experiments were sealed with only 25% stoichiometric excess oxygen gas to replace only the Si-H bonds with Si-O bonds. Therefore, there is not enough oxygen present for all the Si-O-Si bonds of the T8 framework to undergo thermal decomposition. However, complete decomposition of T8 to SiO_2 was observed in the experiments by ^{29}Si NMR and IR spectrometry.

3.5 Suggested Future Work

The initial characterization studies of T8 have shown that the hydridospherosiloxanes are a useful class of novel precursors for CVD of silicon dioxide. Further studies are necessary to confirm the preservation of the T8 Si-O-Si structure in the SiO_2 decomposition product. Spectrometric techniques (such as Raman) which allows comparison of the bond angles in hydridospherosiloxane precursor to bond angles in the SiO_2 decomposition product would be beneficial in examining the integrity of the structure.

Systematic characterization of other hydridospherosiloxanes such as T10 and T12 would also assist in the understanding the decomposition properties of this novel class of SiO_2 precursors. Comparison of the bond angles in SiO_2 formed from the different hydridospherosiloxanes should also provide evidence for preservation of the Si-O-Si framework. The Si-O-Si bond angles of the SiO_2 should increase with increasing bond angle of the hydridospherosiloxane.

Characterization of SiO_2 thin films deposited individually from T8, T10, and T12 should also be useful for confirming the proposed decomposition mechanism. If the structure of the hydridospherosiloxane is preserved in the SiO_2 thin film, then characteristics such as packing density and optical properties should vary with increasing size of the polyhedral unit.

---

1 Desu, S.B.; Peng, C.H.; Tian S. and Agaskar, P.A., "Low Temperature CVD of SiO2 using Novel Precursors", to be published in the Journal of the Electrochemical Society, 1992.

2 Agaskar, P.A.; Day, V.W.; Klemperer, W.G."A New Route to Trimethylsilyated Spherosilicates: Synthesis and Structure of $[Si_{12}O_{18}](OSiMe_3)_{12}$, D_{3h}-$[Si_{14}O_{21}](OSiMe_3)_{14}$, and C_{2v}-$[Si_{14}O_{21}](OSiMe_3)_{14}$", Journal of the American Chemical Society. , 109, pp 5554-5557, (1987).

3 Jensen, Klavs F. and Kern, Werner; "Thermal Chemical Vapor Deposition"; Thin Film Processes II, (edited by Kern and Vossen), Academic Press, Chapter III, (1991).

4 Bornhauser, Peter and Calzaferri, Gion, "Normal coordination analysis of $H_8Si_8O_{12}$", Spectrochimica Acta, 46A(7), (1990), pp 1045-1056.

5 Launer, Phillip, "Infrared analysis of organosilicon compounds: spectra-structure correlations", Petrarch Systems: Silanes and Silicones, Bristol, PA, pp 69-72, 1987.

6 Lucovsky, G.; Tsu, D.V. and Kim, S.S., "Formation of thin film dielectrics by remote plasma-enhanced chemical-vapor deposition (remote PECVD)", Applied Surface Science, 39, (1989), pp 33-56.

7 Fyfe, Colin A., "Solid State NMR for Chemists", CFC Press, Ontario, CA, (1983), chapter 7.

8 Lippmaa, E.; Magi, M; Samoson, A.; Engelhardt, G. and Grimmer, A.R. "Structural Studies of Silicates by Solid State High-Resolution ^{29}Si NMR"., Journal of the American Chemical Society, 102, 15, pp 4889-4893, (1980).

9 Agaskar, P.A.; Day, V.W.; Klemperer, W.G."A New Route to Trimethylsilyated Spherosilicates: Synthesis and Structure of $[Si_{12}O_{18}](OSiMe_3)_{12}$, D_{3h}-$[Si_{14}O_{21}](OSiMe_3)_{14}$, and C_{2v}-$[Si_{14}O_{21}](OSiMe_3)_{14}$", Journal of the American Chemical Society. , 109, pp 5554-5557, (1987).

10 Aujla, R.; Dupree, R.; Farnan, I; and Holland, D., "A Magic Angle Spinning NMR Study of the Structure of Vitreous Silica Prepared in Different Ways", Diffusion Defect Data, 53-54, pp 99-104, (1987).

11 Kerr, J.A., "Strength of chemical bonds", CRC Handbook of Chemistry and Physics, 57th edition, CRC press, Boca Raton, FL, pp F219-F225.

APPENDICES

APPENDIX A:

Near IR spectra of $Zr(thd)_4$ decomposition products.

Spectral range = 125-700 cm^{-1}

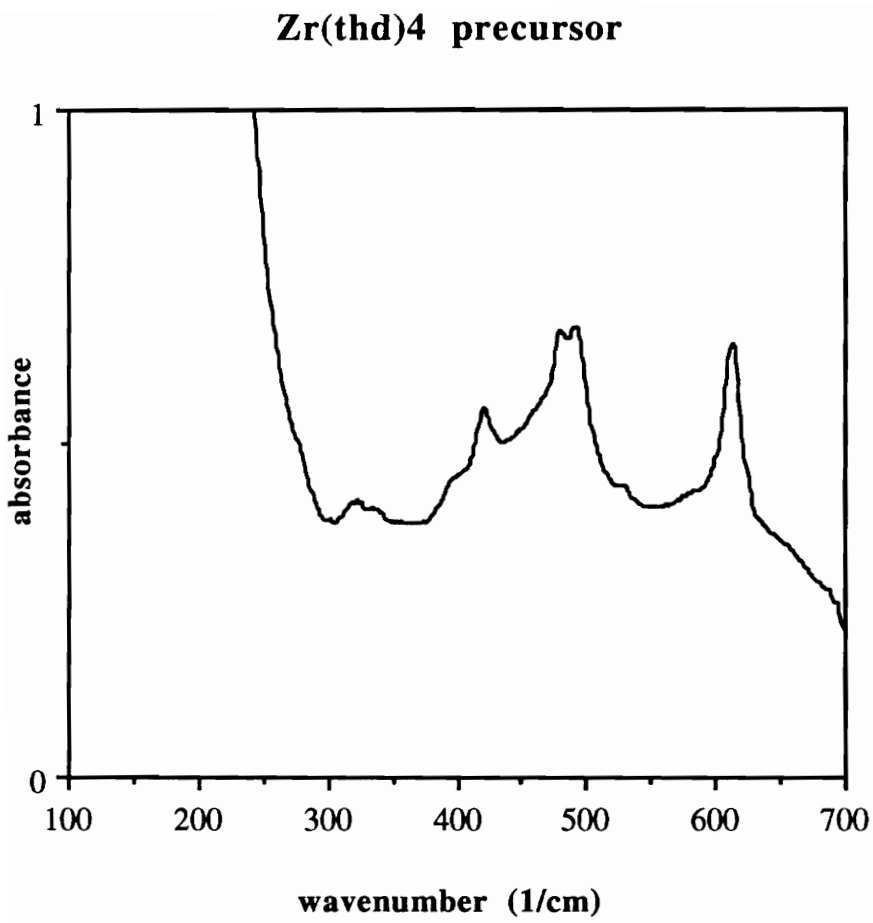
Zr(thd)4 precursor
1
0
absorbance
100
200
300
400
500
600
700
wavenumber (1/cm)

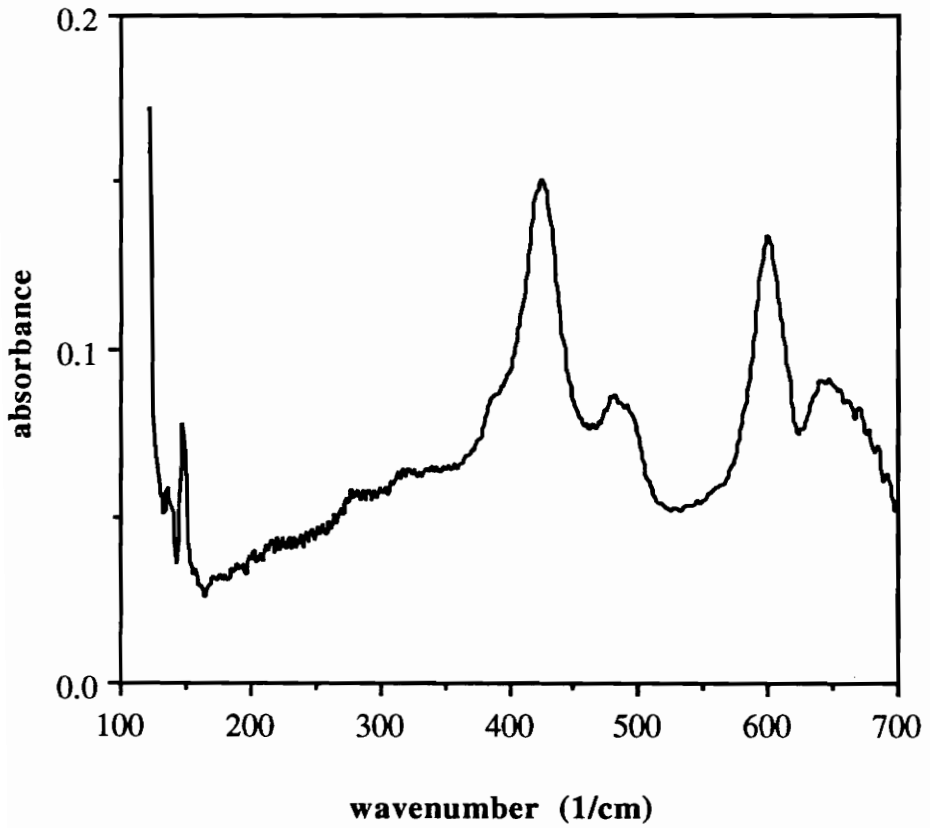
Zr(thd)4 decomposition: 350 °C, 40 min
absorbance
0.2
0.1
0.0
100
200
300
400
500
600
700
wavenumber (1/cm)

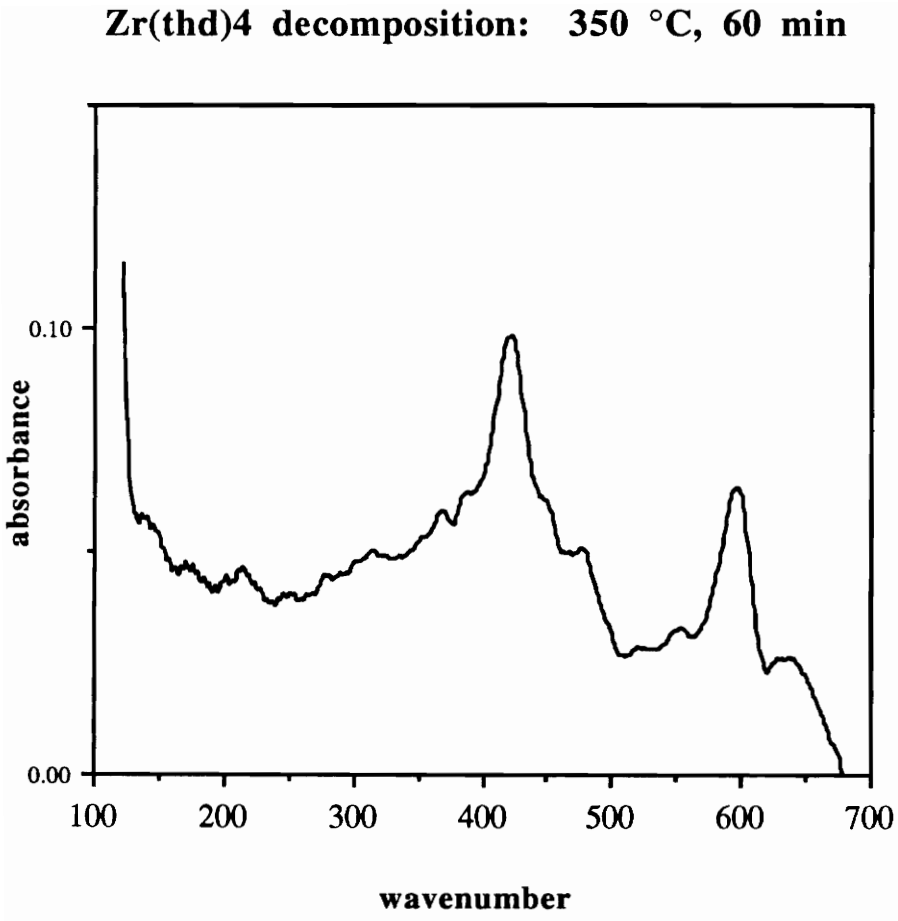
Zr(thd)4 decomposition: 350 °C, 60 min
absorbance
0.10
0.00
100
200
300
400
500
600
700
wavenumber

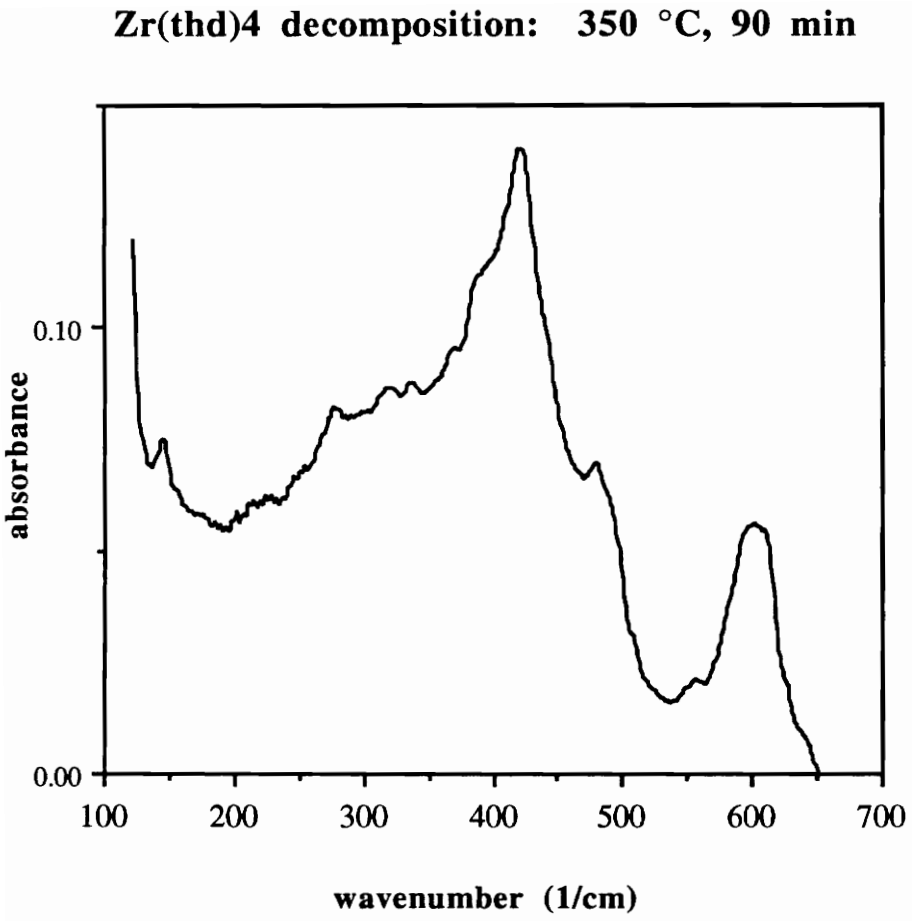
Zr(thd)4 decomposition: 350 °C, 90 min
absorbance
0.10
0.00
100
200
300
400
500
600
700
wavenumber (1/cm)

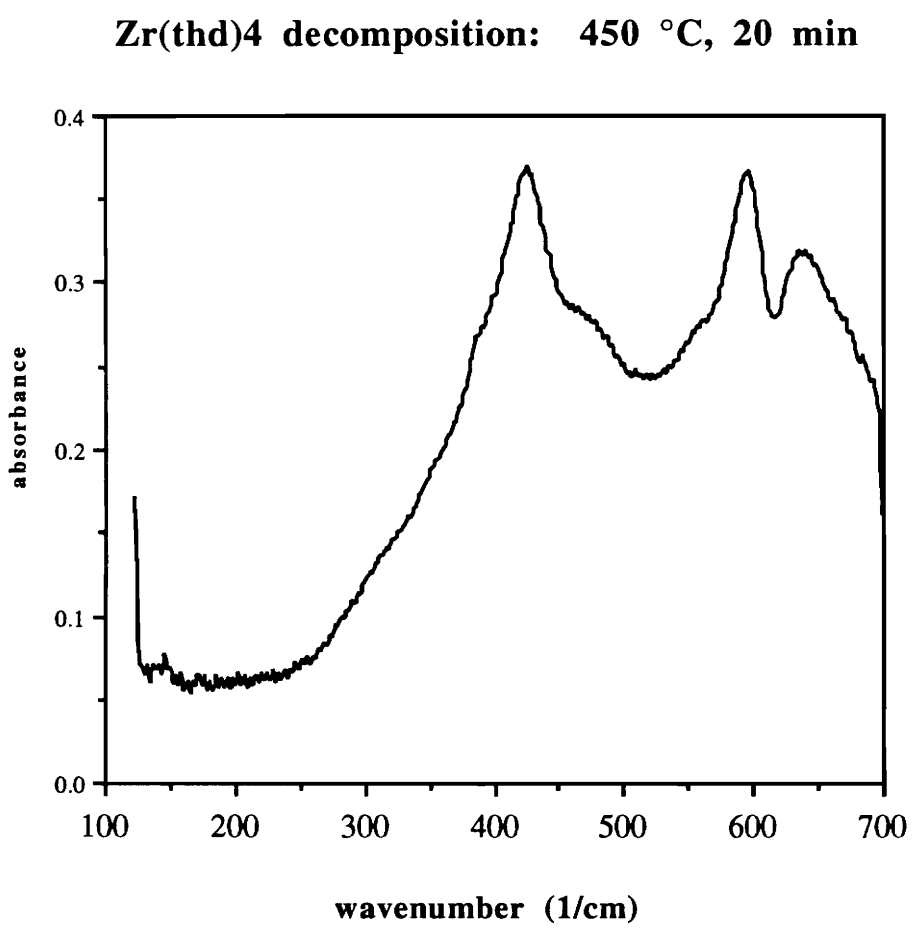
Zr(thd)4 decomposition: 450 °C, 20 min
absorbance
0.0
0.1
0.2
0.3
0.4
100
200
300
400
500
600
700
wavenumber (1/cm)

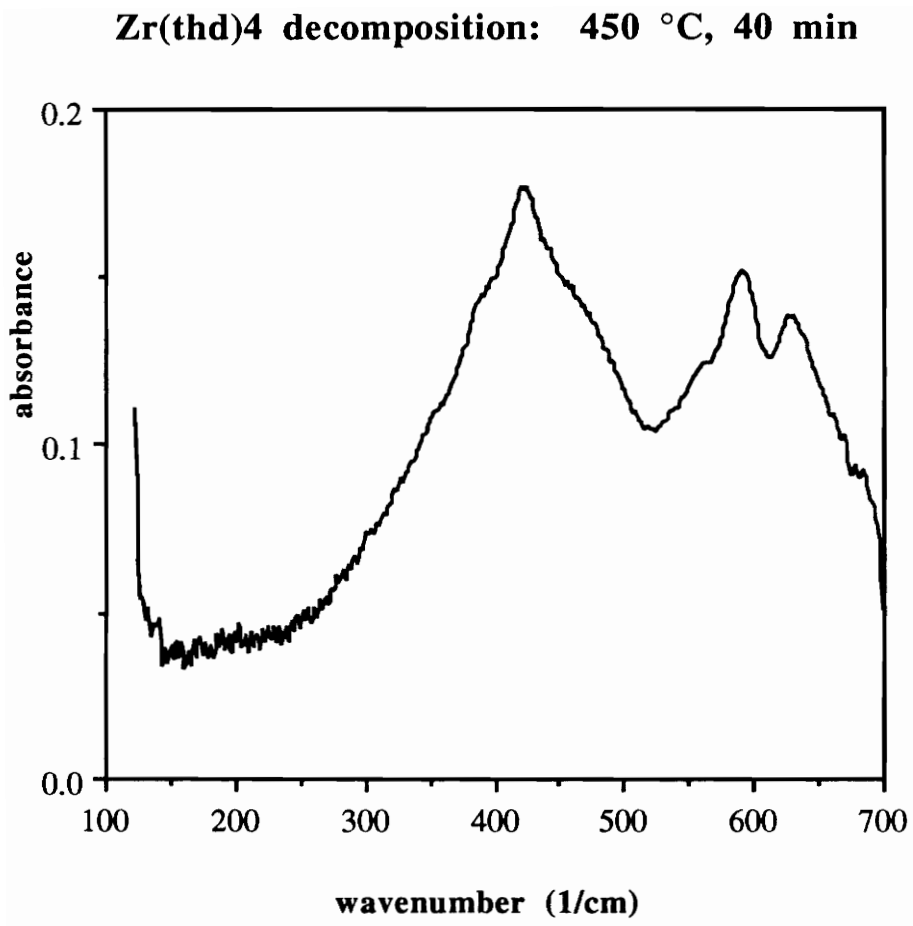
Zr(thd)4 decomposition: 450 °C, 40 min
absorbance
0.2
0.1
0.0
100
200
300
400
500
600
700
wavenumber (1/cm)

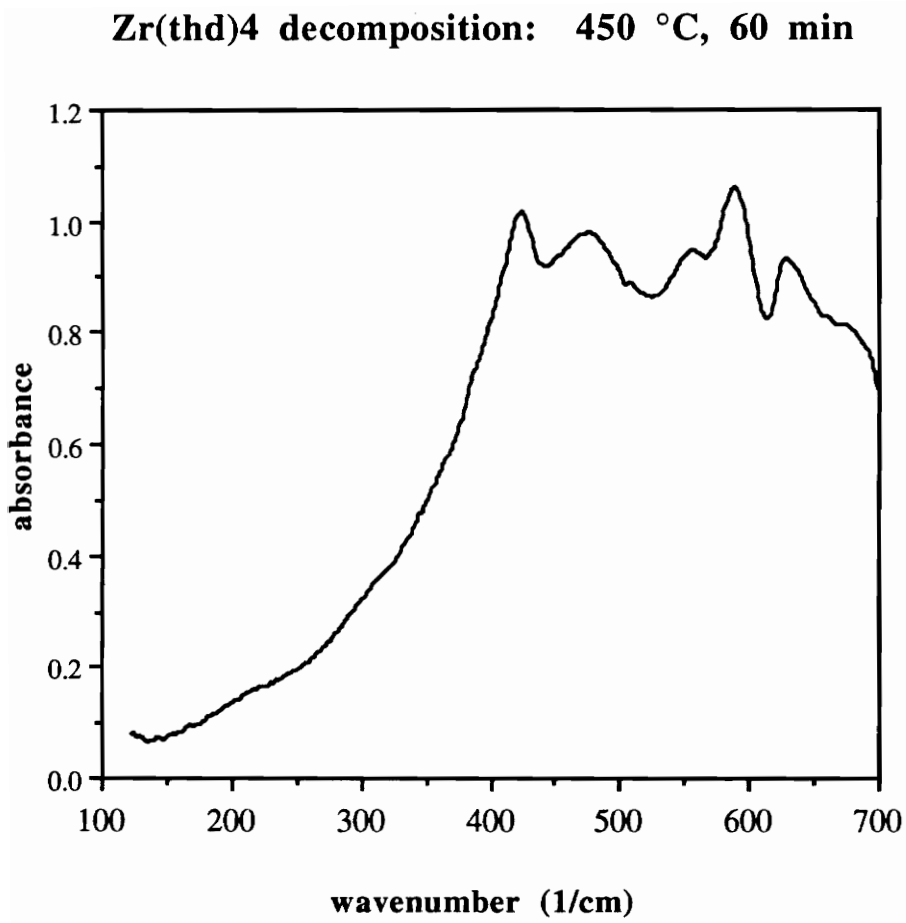
Zr(thd)4 decomposition: 450 °C, 60 min
absorbance
1.2
1.0
0.8
0.6
0.4
0.2
0.0
100
200
300
400
500
600
700
wavenumber (1/cm)

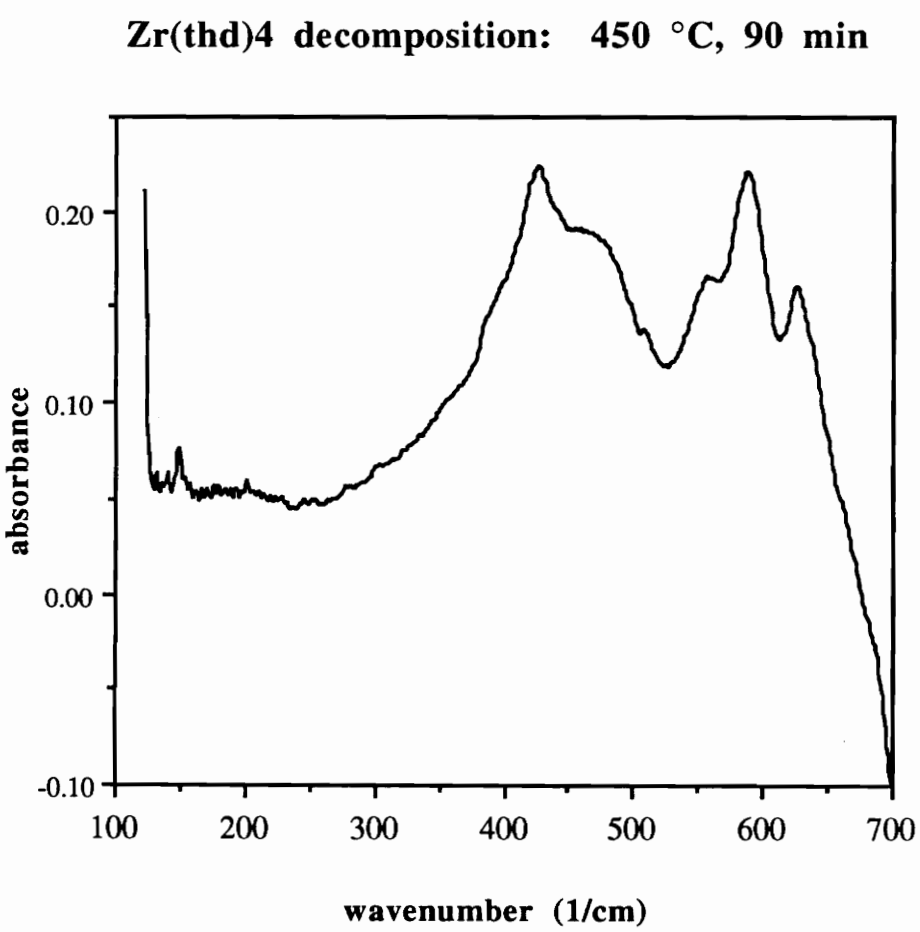
Zr(thd)4 decomposition: 450 °C, 90 min
absorbance
0.20
0.10
0.00
-0.10
100
200
300
400
500
600
700
wavenumber (1/cm)

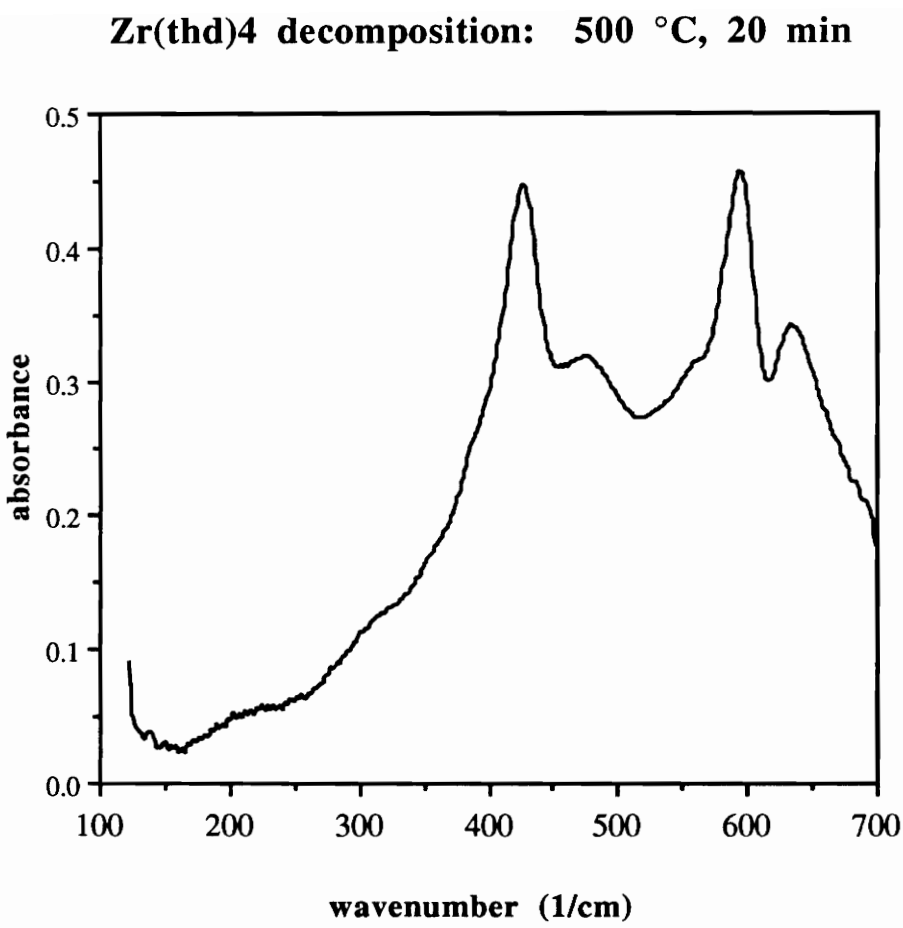
Zr(thd)4 decomposition: 500 °C, 20 min
absorbance
0.0
0.1
0.2
0.3
0.4
0.5
100
200
300
400
500
600
700
wavenumber (1/cm)

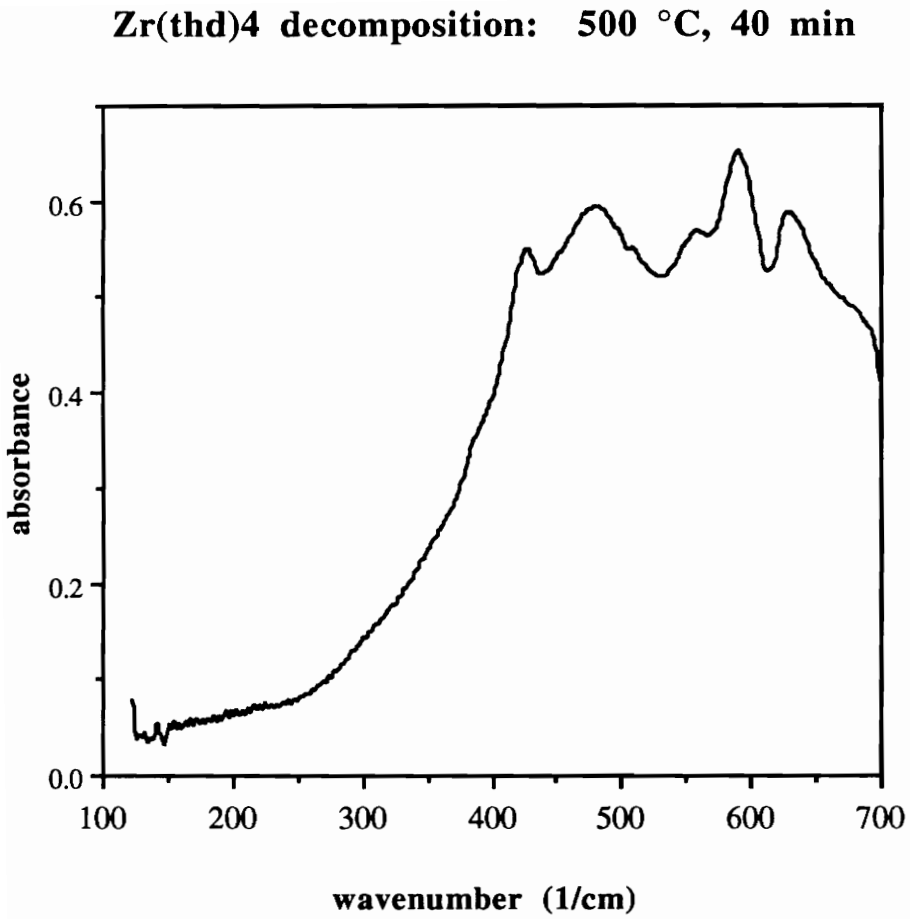
Zr(thd)4 decomposition: 500 °C, 40 min
absorbance
0.0
0.2
0.4
0.6
100
200
300
400
500
600
700
wavenumber (1/cm)

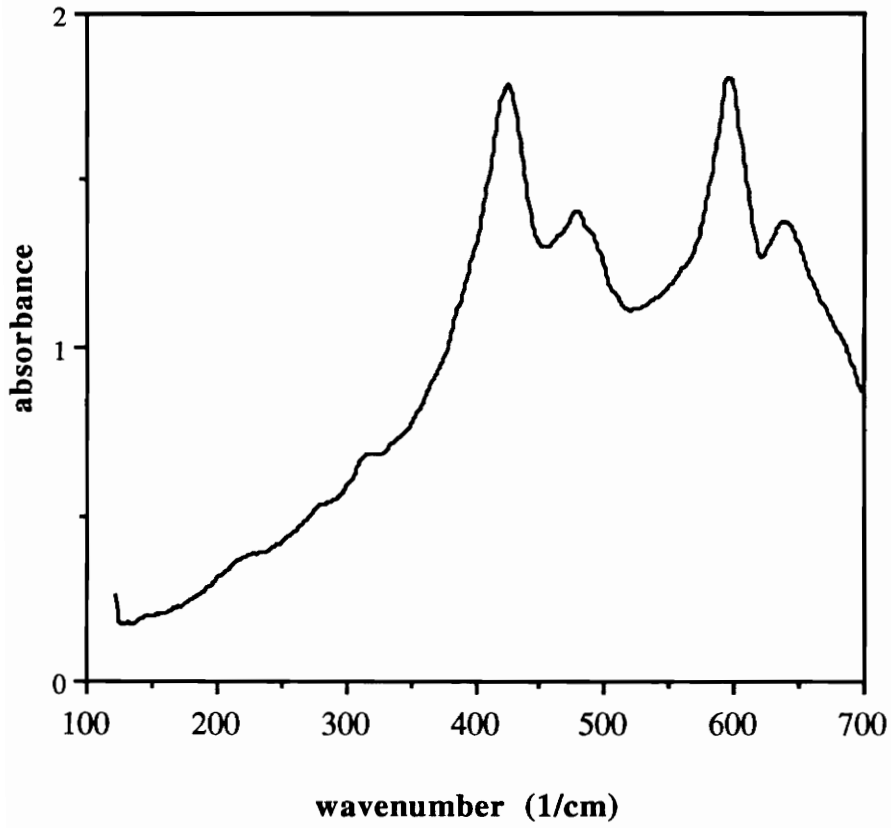
Zr(thd)4 decomposition: 550 °C, 10 min
absorbance
0
1
2
100
200
300
400
500
600
700
wavenumber (1/cm)

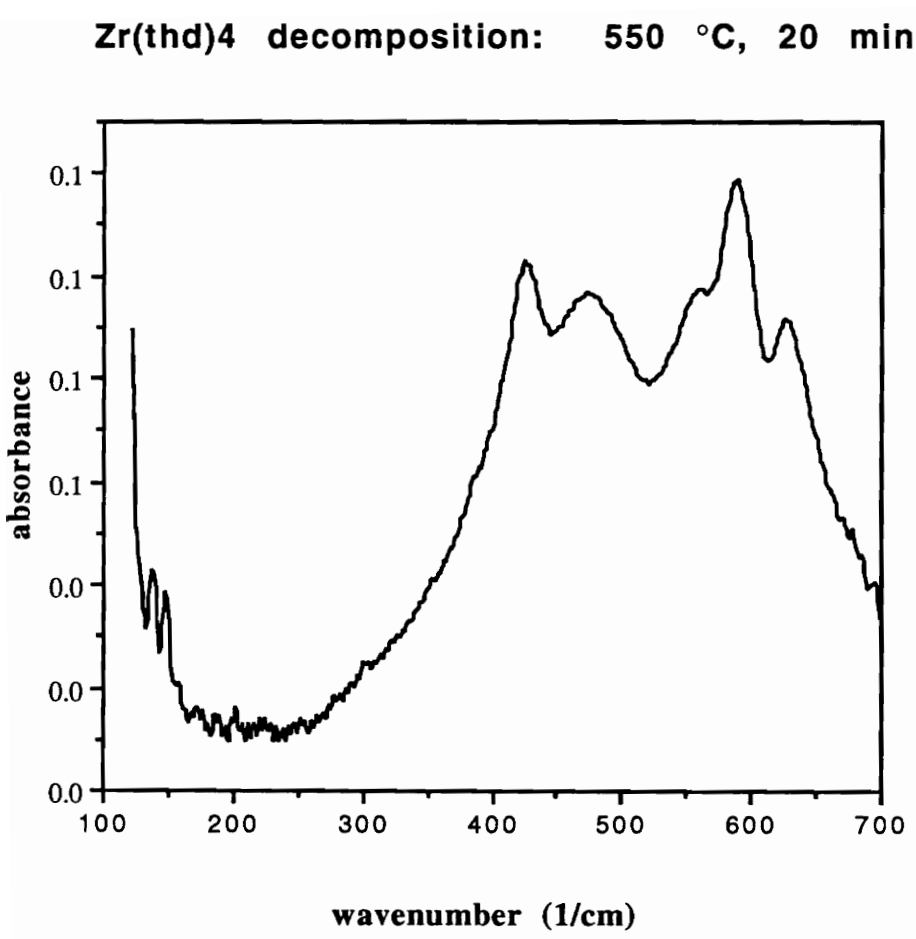
Zr(thd)4 decomposition: 550 °C, 20 min
absorbance
0.1
0.1
0.1
0.1
0.0
0.0
0.0
100
200
300
400
500
600
700
wavenumber (1/cm)

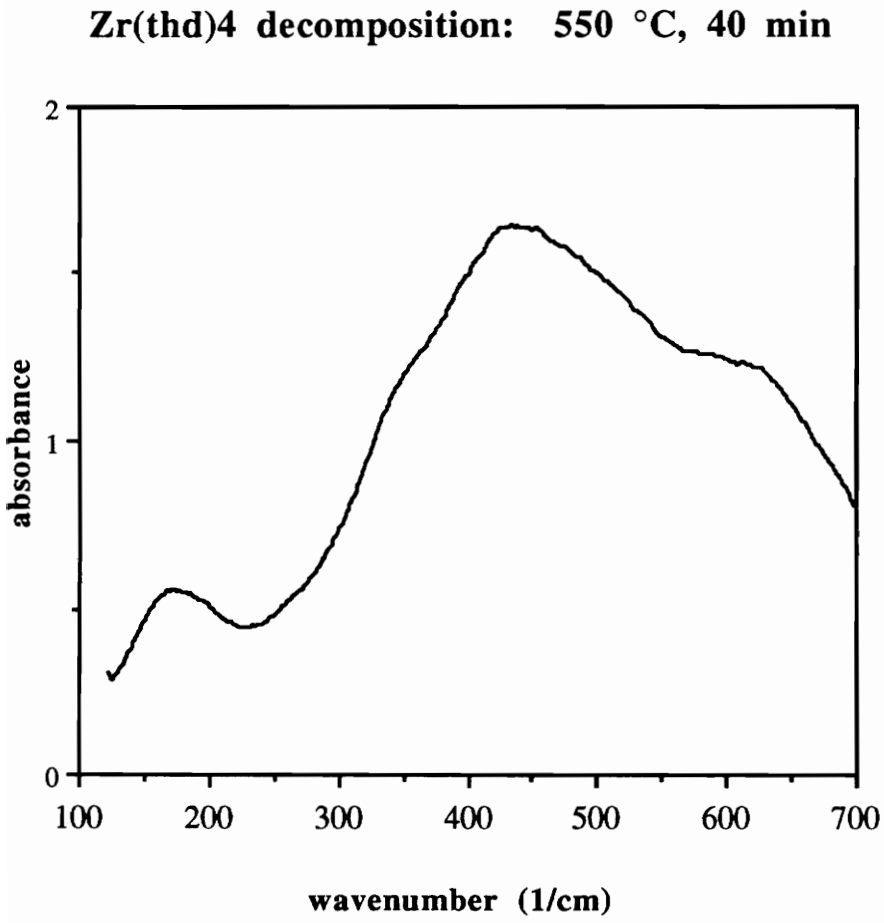
Zr(thd)4 decomposition: 550 °C, 40 min
absorbance
2
1
0
100
200
300
400
500
600
700
wavenumber (1/cm)

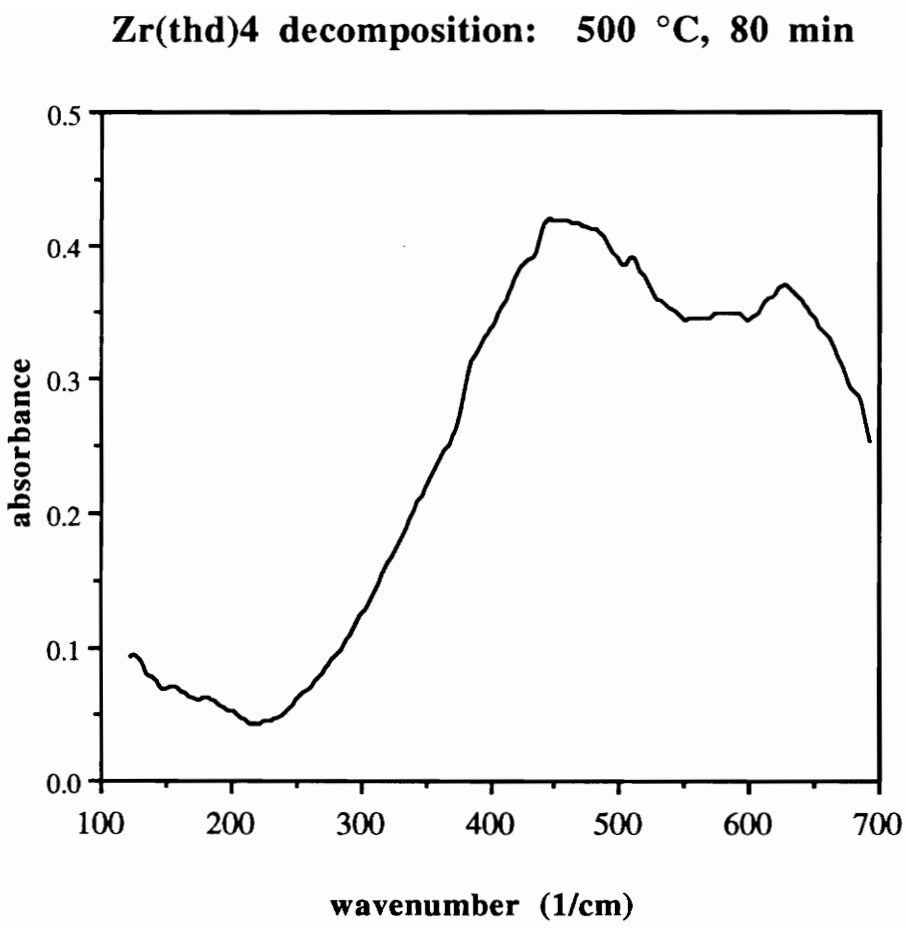
Zr(thd)4 decomposition: 500 °C, 80 min
absorbance
0.0
0.1
0.2
0.3
0.4
0.5
100
200
300
400
500
600
700
wavenumber (1/cm)

APPENDIX B:

Near IR spectra of $Pb(thd)_2$ decomposition products.

Spectral range = 125-700 cm^{-1}

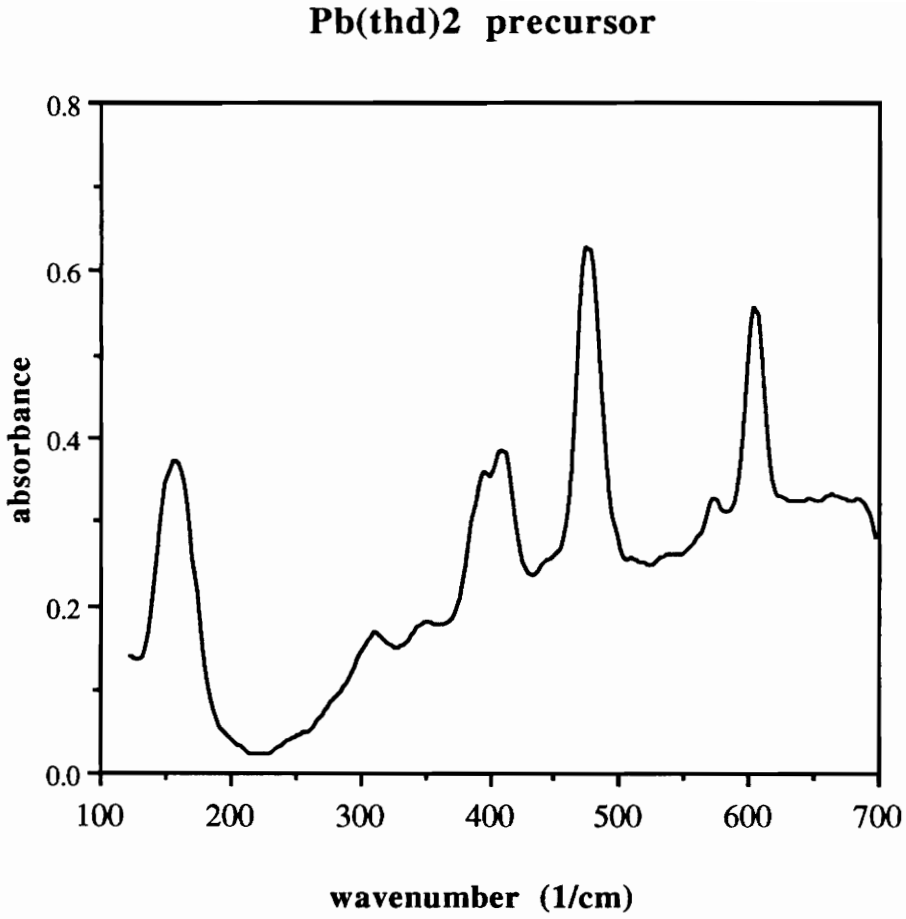
Pb(thd)2 precursor
absorbance
0.0
0.2
0.4
0.6
0.8
100
200
300
400
500
600
700
wavenumber (1/cm)

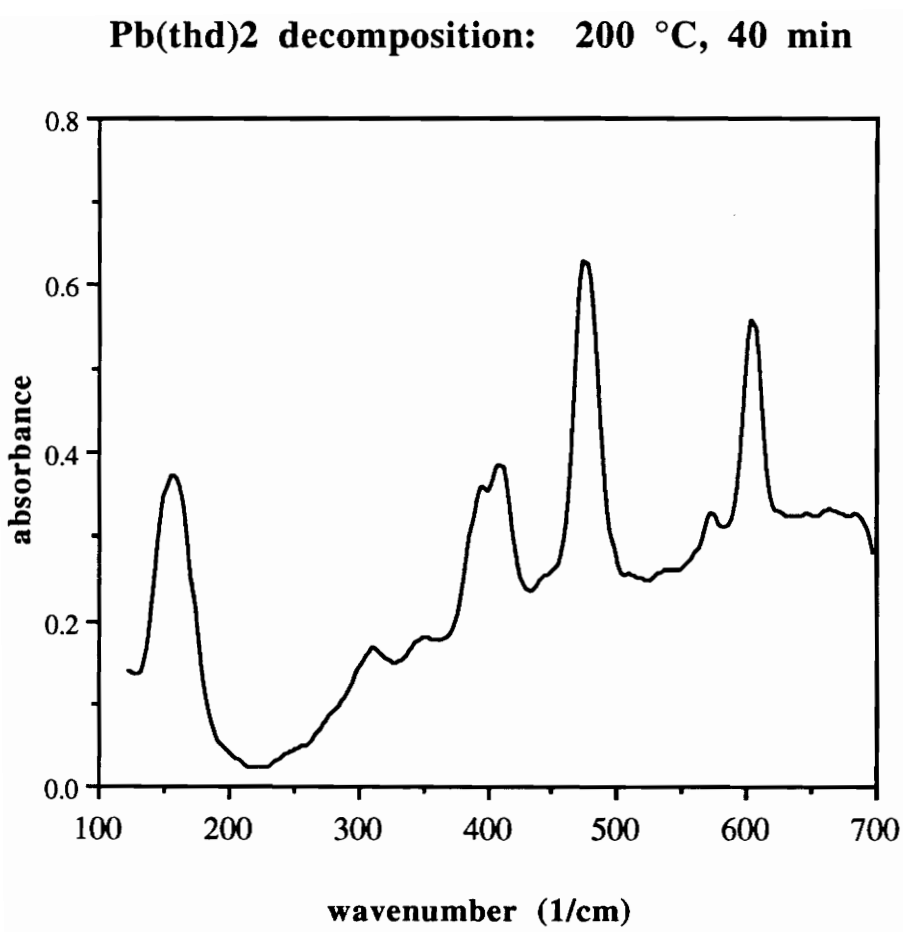
Pb(thd)2 decomposition: 200 °C, 40 min
absorbance
0.0
0.2
0.4
0.6
0.8
100
200
300
400
500
600
700
wavenumber (1/cm)

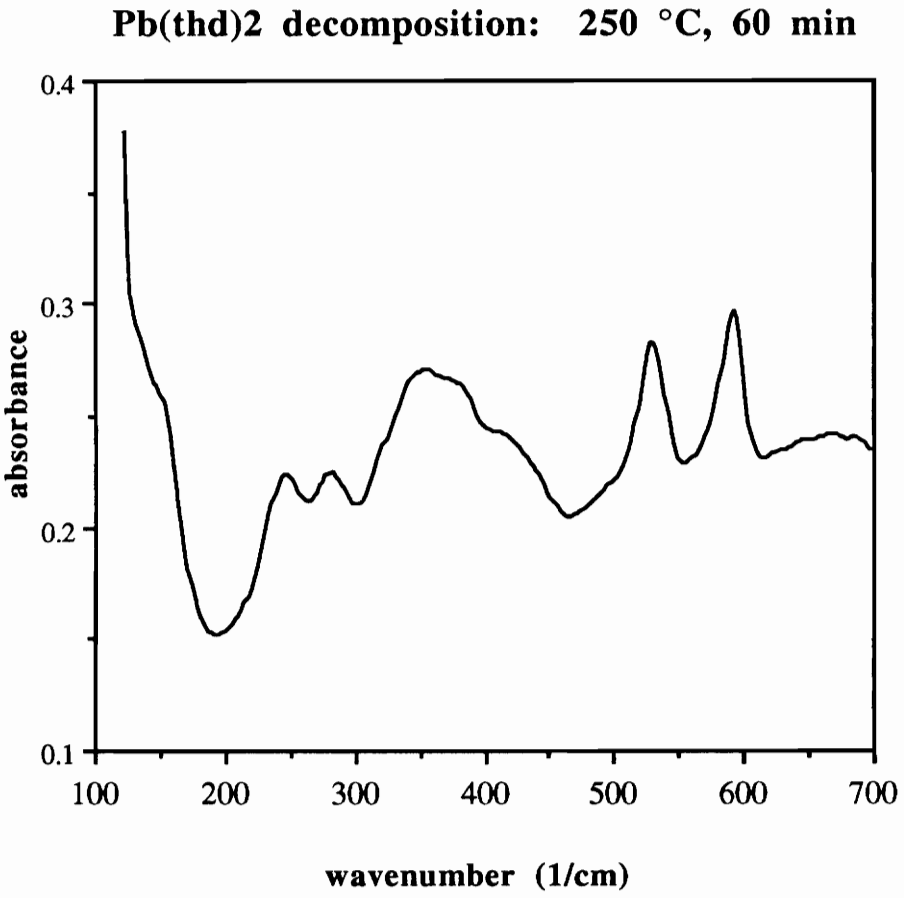
Pb(thd)2 decomposition: 250 °C, 60 min
absorbance
0.4
0.3
0.2
0.1
100
200
300
400
500
600
700
wavenumber (1/cm)

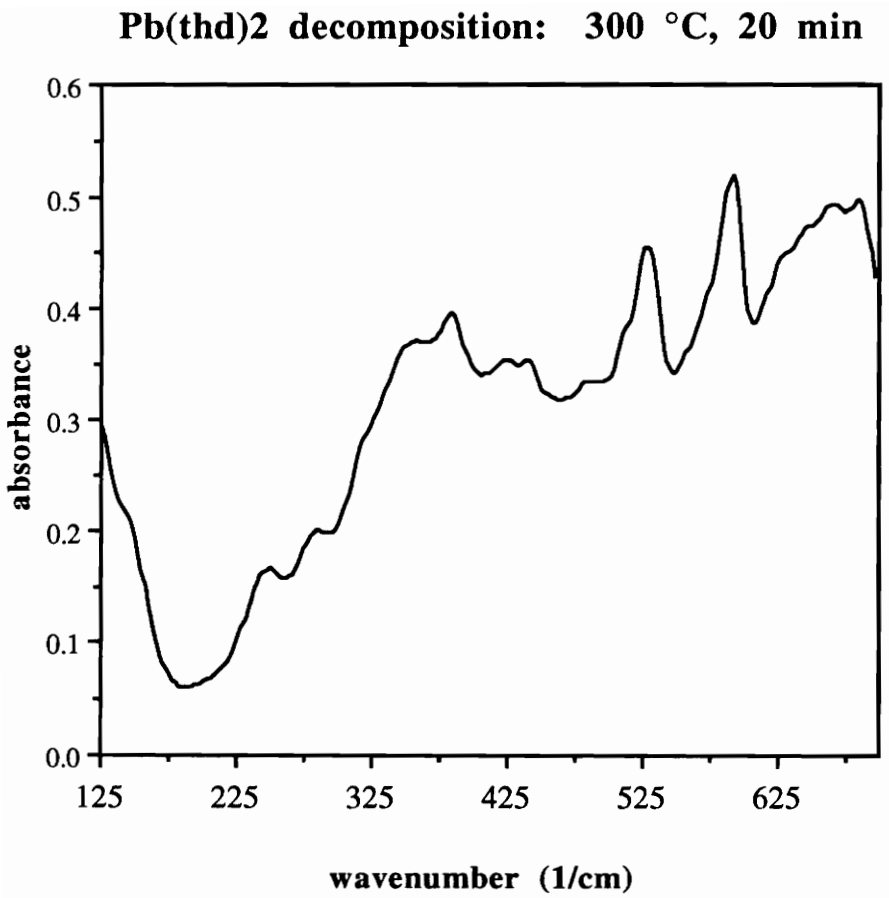
Pb(thd)2 decomposition: 300 °C, 20 min
absorbance
0.0
0.1
0.2
0.3
0.4
0.5
0.6
125
225
325
425
525
625
wavenumber (1/cm)

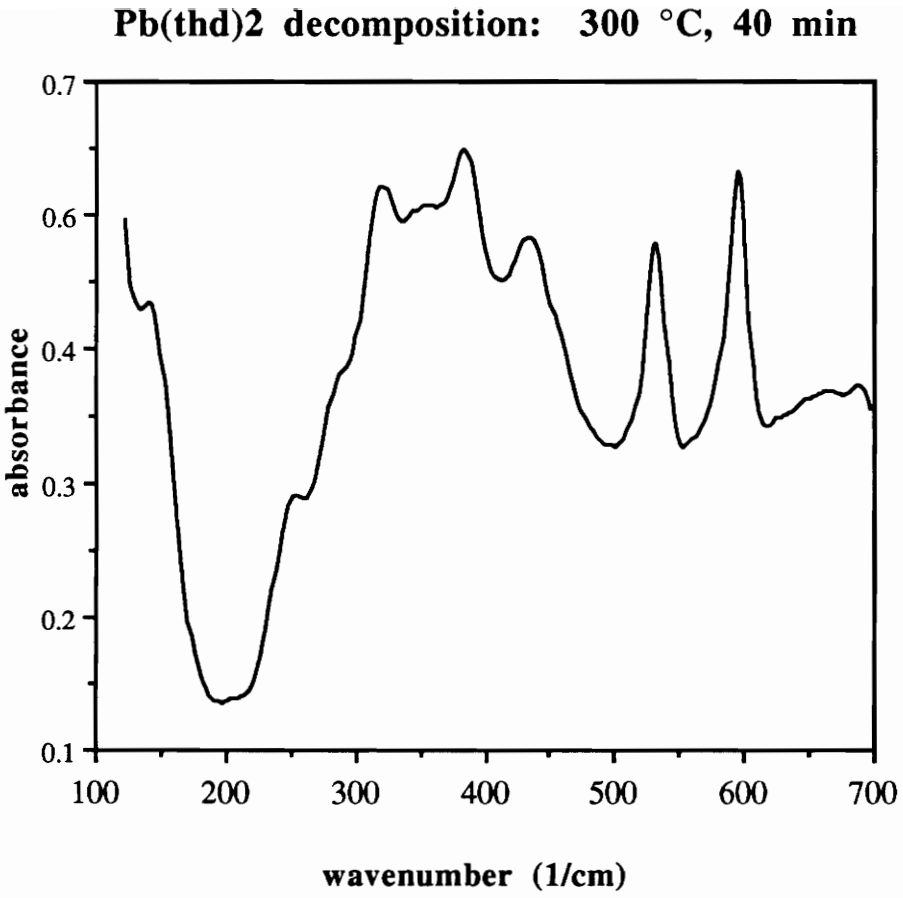
Pb(thd)2 decomposition: 300 °C, 40 min
absorbance
0.7
0.6
0.4
0.3
0.2
0.1
100
200
300
400
500
600
700
wavenumber (1/cm)

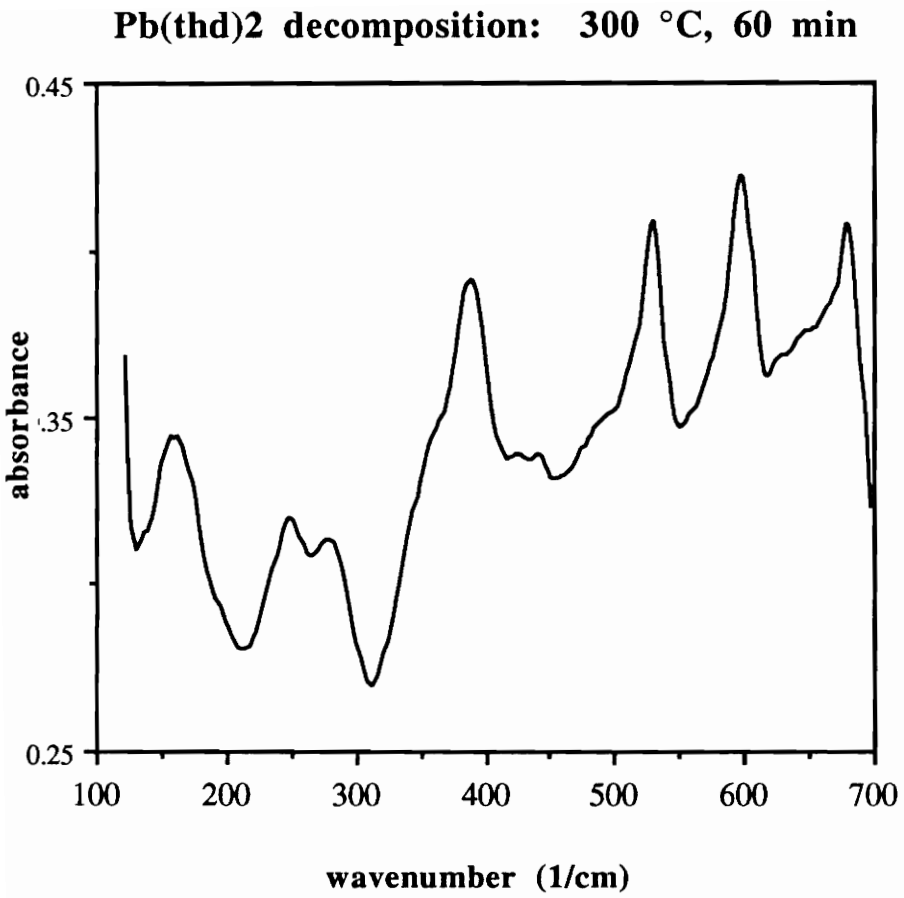
Pb(thd)2 decomposition: 300 °C, 60 min
0.45
.35
0.25
absorbance
100
200
300
400
500
600
700
wavenumber (1/cm)

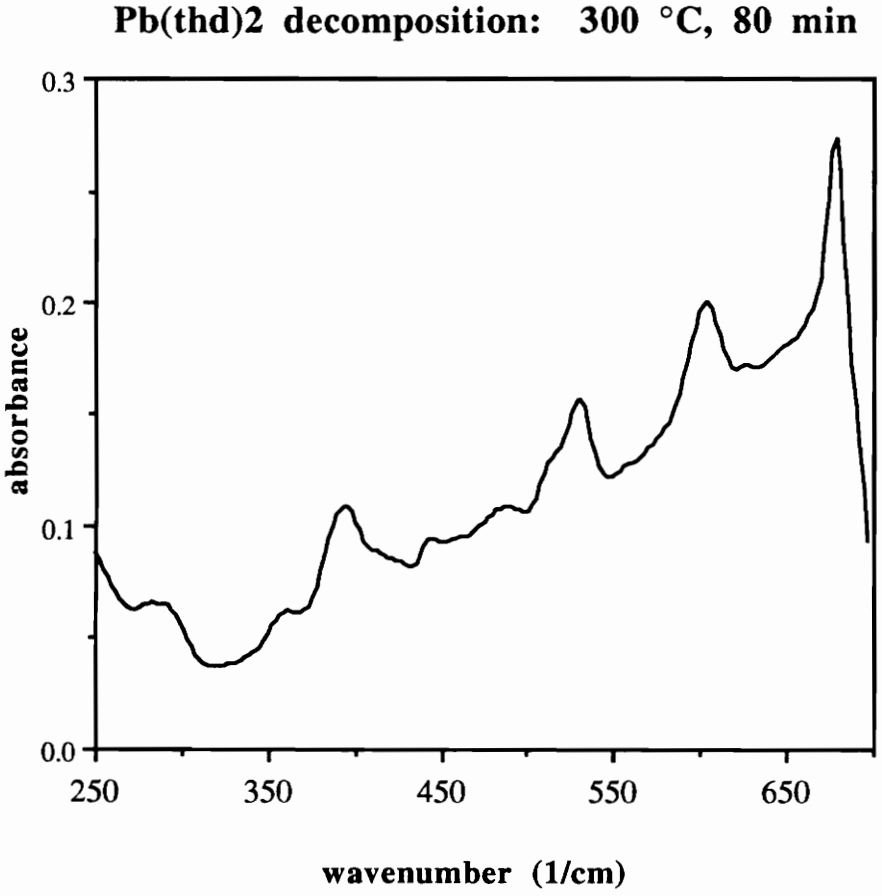
Pb(thd)2 decomposition: 300 °C, 80 min
absorbance
0.3
0.2
0.1
0.0
250
350
450
550
650
wavenumber (1/cm)

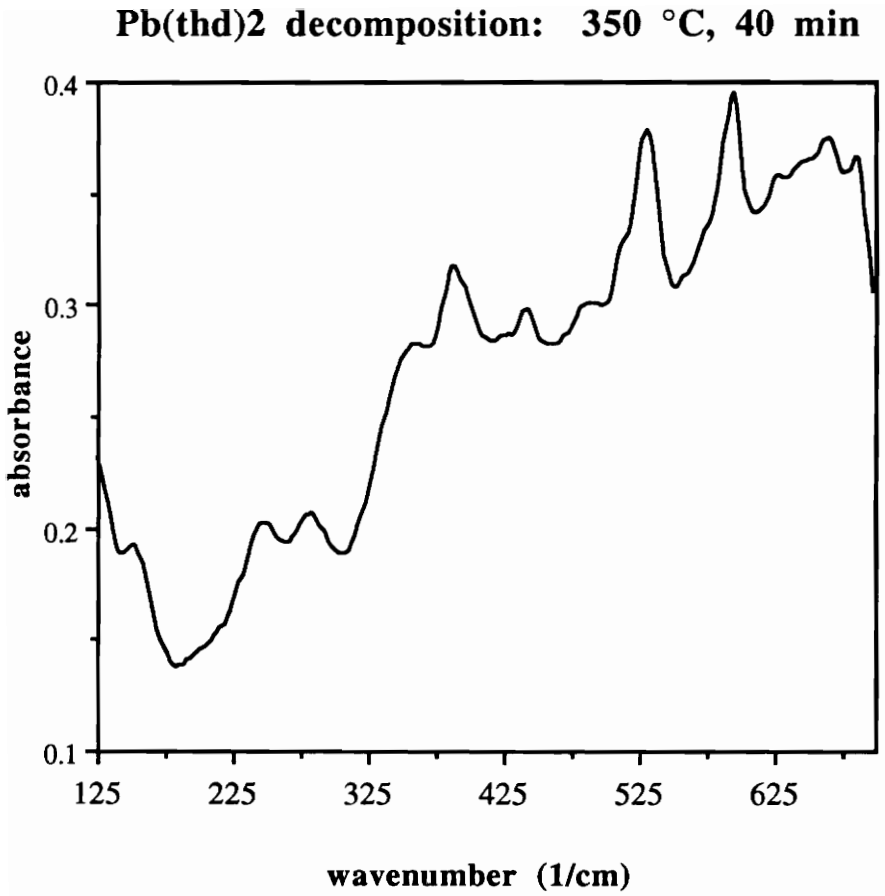
Pb(thd)2 decomposition: 350 °C, 40 min
absorbance
0.4
0.3
0.2
0.1
125
225
325
425
525
625
wavenumber (1/cm)

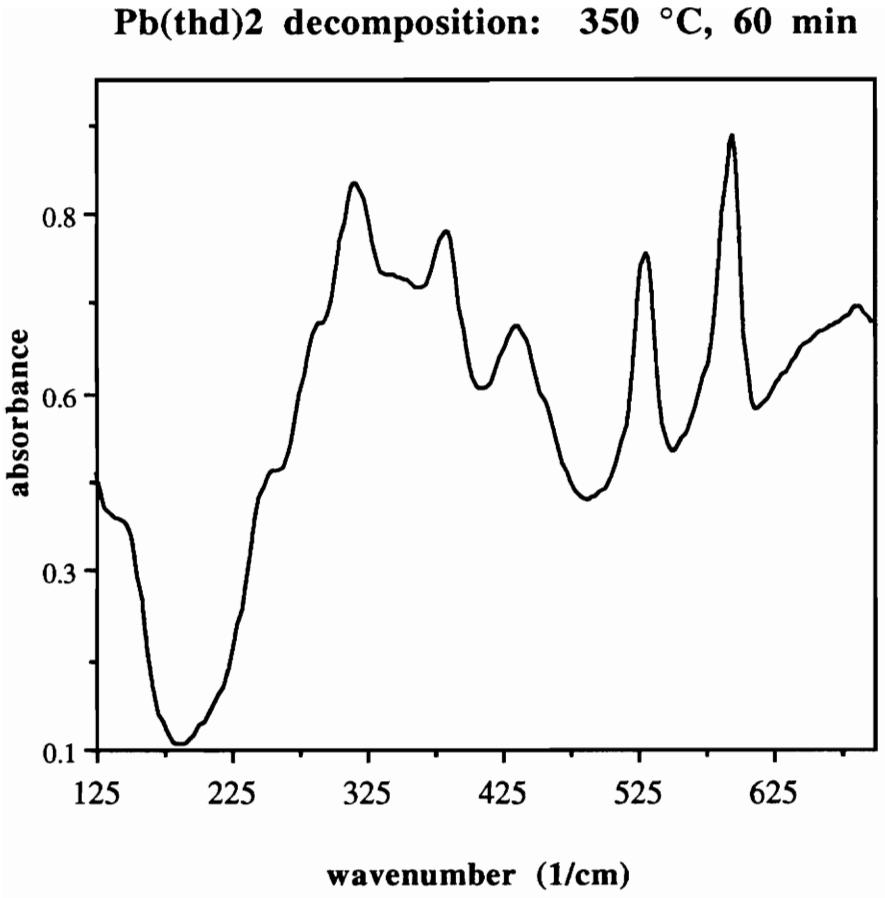
Pb(thd)2 decomposition: 350 °C, 60 min
absorbance
0.8
0.6
0.3
0.1
125
225
325
425
525
625
wavenumber (1/cm)

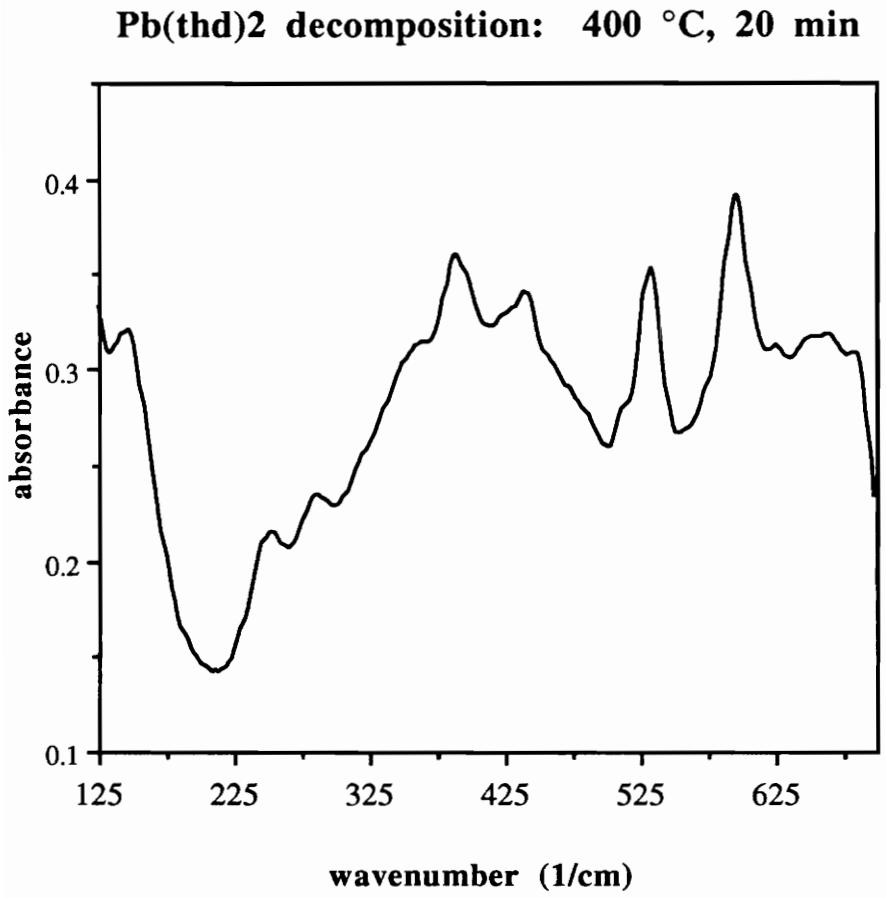
Pb(thd)2 decomposition: 400 °C, 20 min
absorbance
0.4
0.3
0.2
0.1
125
225
325
425
525
625
wavenumber (1/cm)

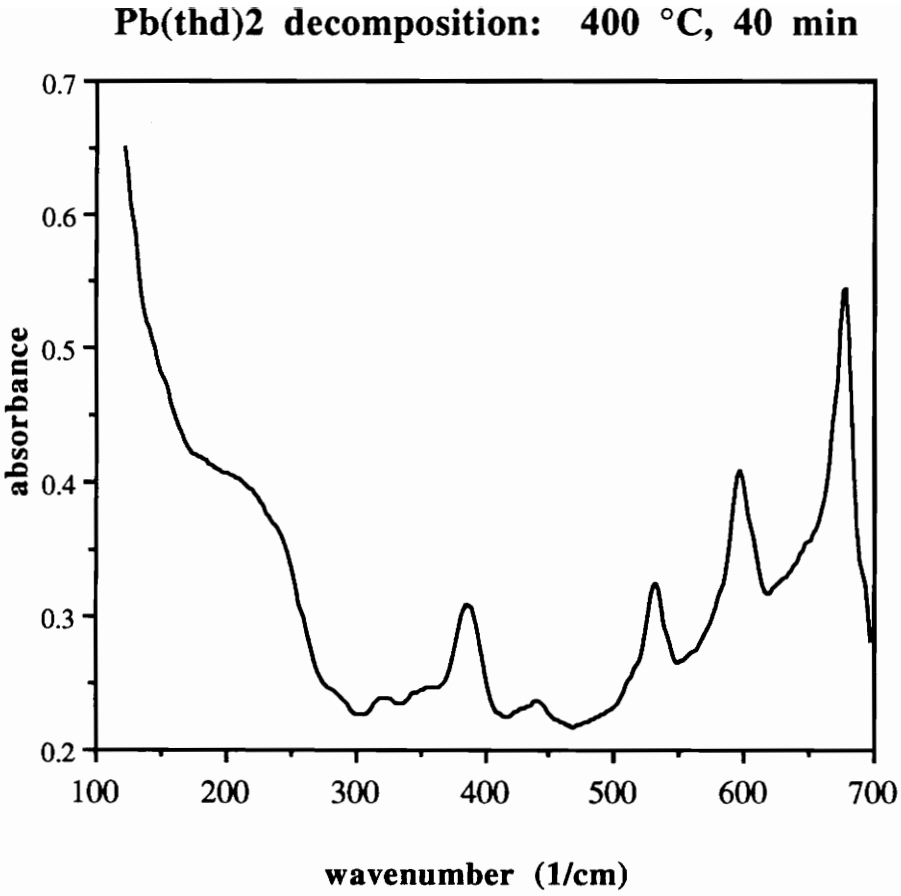
Pb(thd)2 decomposition: 400 °C, 40 min
absorbance
0.7
0.6
0.5
0.4
0.3
0.2
100
200
300
400
500
600
700
wavenumber (1/cm)

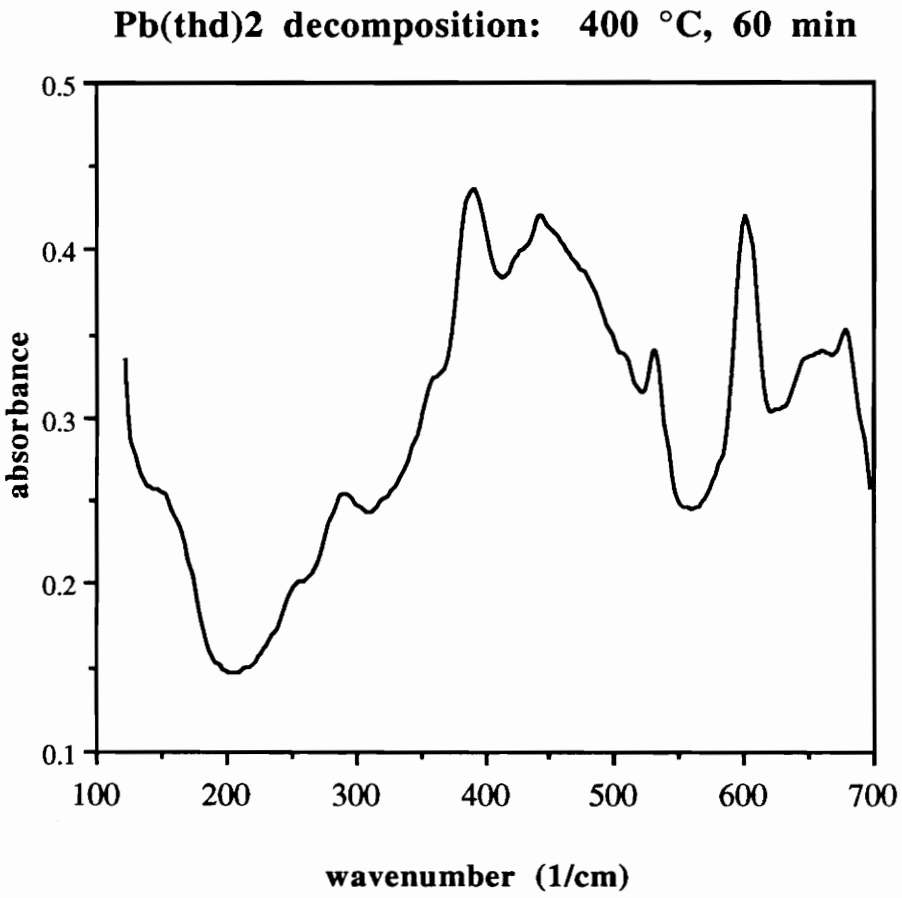
Pb(thd)2 decomposition: 400 °C, 60 min
absorbance
0.5
0.4
0.3
0.2
0.1
100
200
300
400
500
600
700
wavenumber (1/cm)

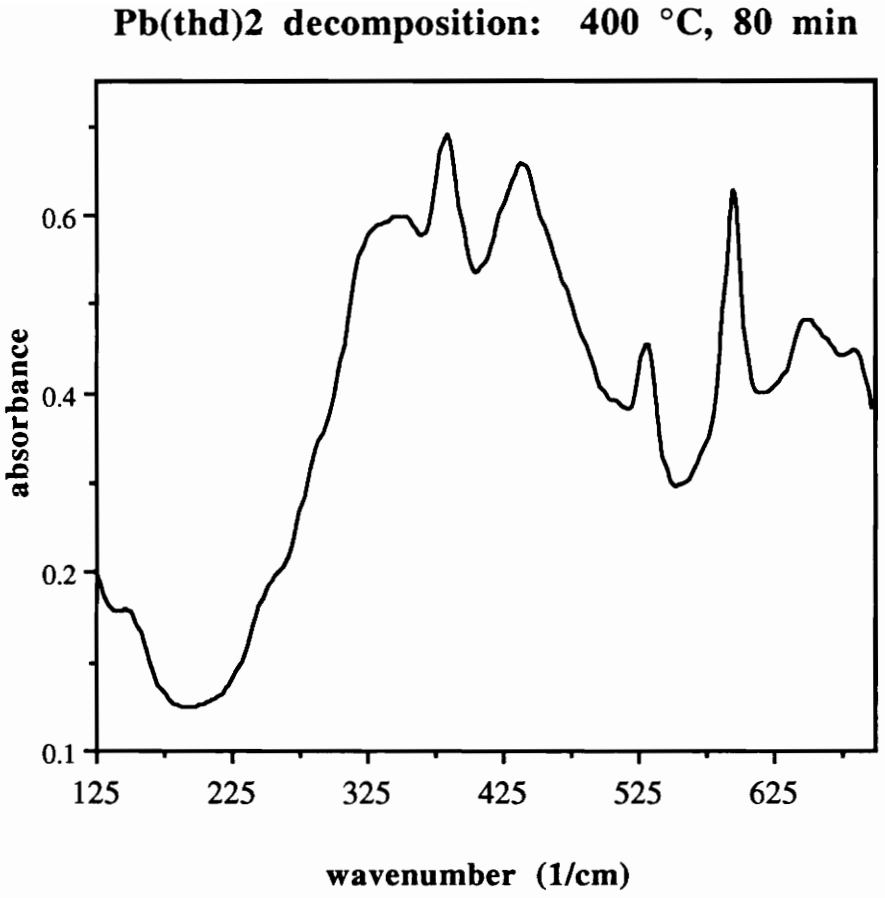
Pb(thd)2 decomposition: 400 °C, 80 min
absorbance
0.6
0.4
0.2
0.1
125
225
325
425
525
625
wavenumber (1/cm)

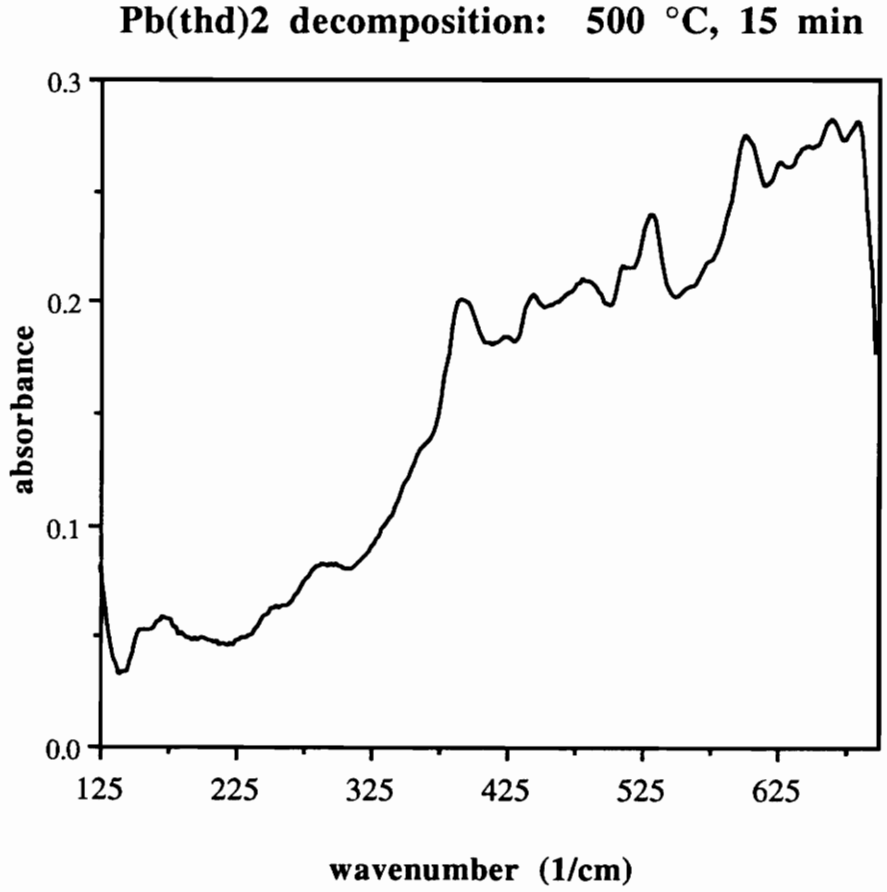
Pb(thd)2 decomposition: 500 °C, 15 min
absorbance
0.0
0.1
0.2
0.3
125
225
325
425
525
625
wavenumber (1/cm)

APPENDIX C:

Mid IR spectra of $Pb(fod)_2$ decomposition products.

Spectral range = 400-4000 cm^{-1}

Pb(fod)$_2$ precursor

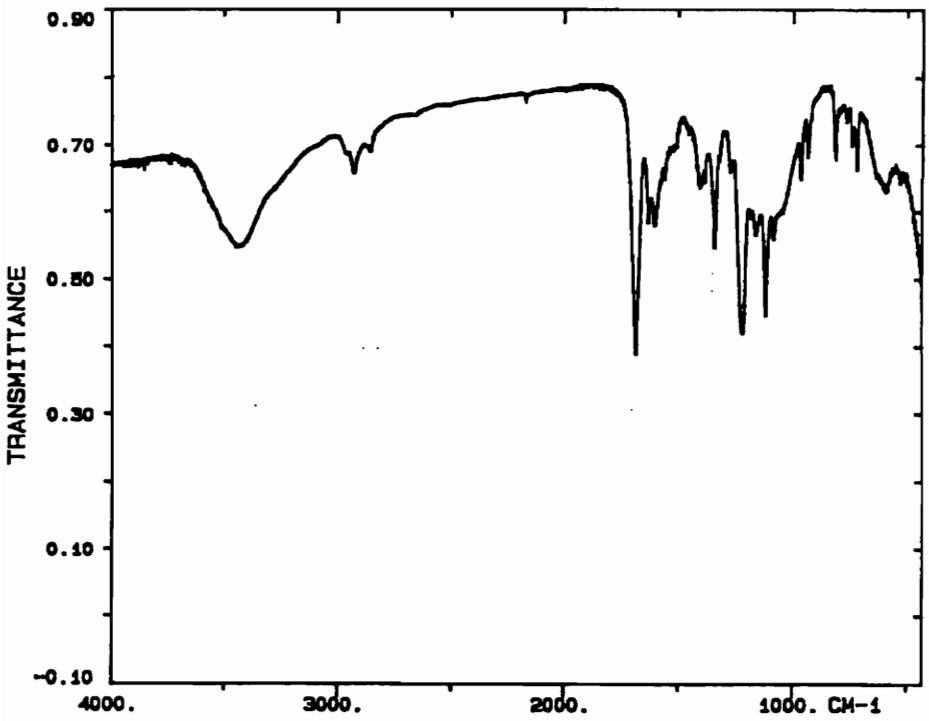

Lead (II) oxide standard

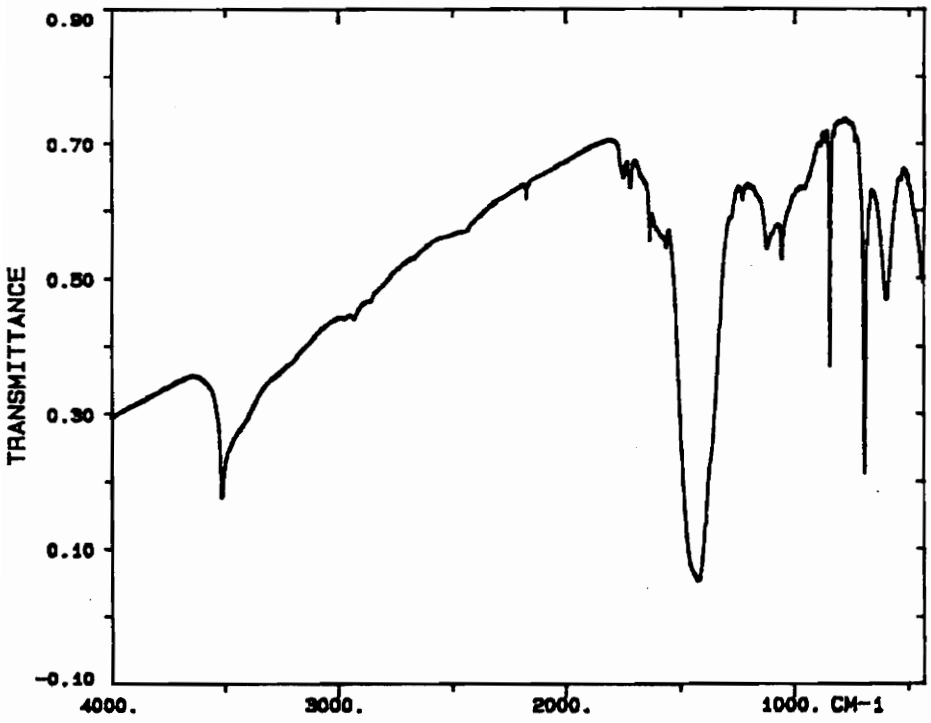

Lead (II) fluoride standard

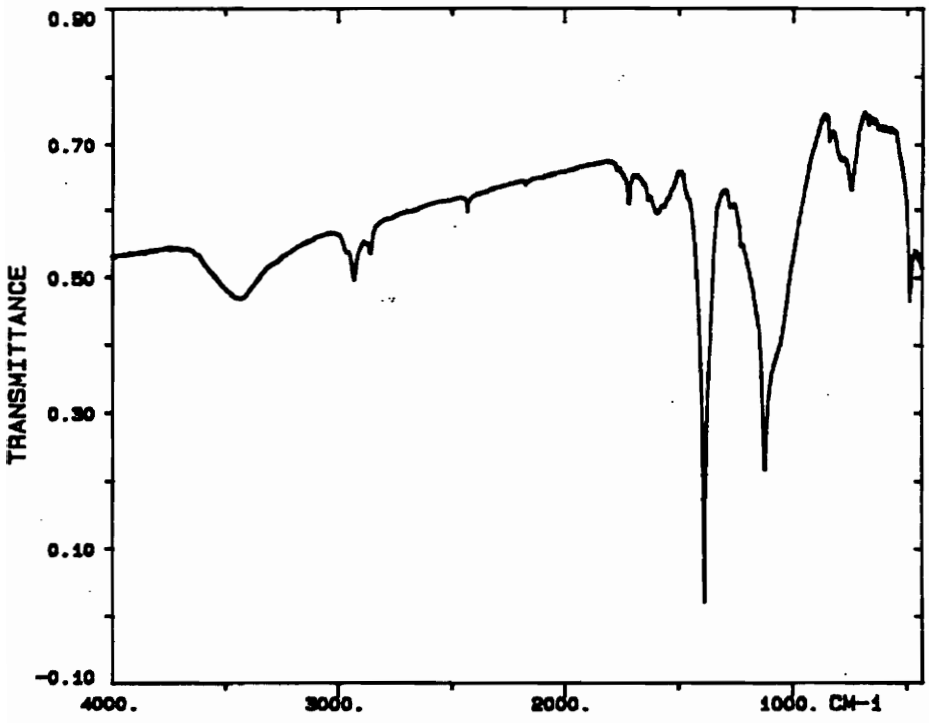

Pb(fod)$_2$ decomposition: 300 °C, 30 min

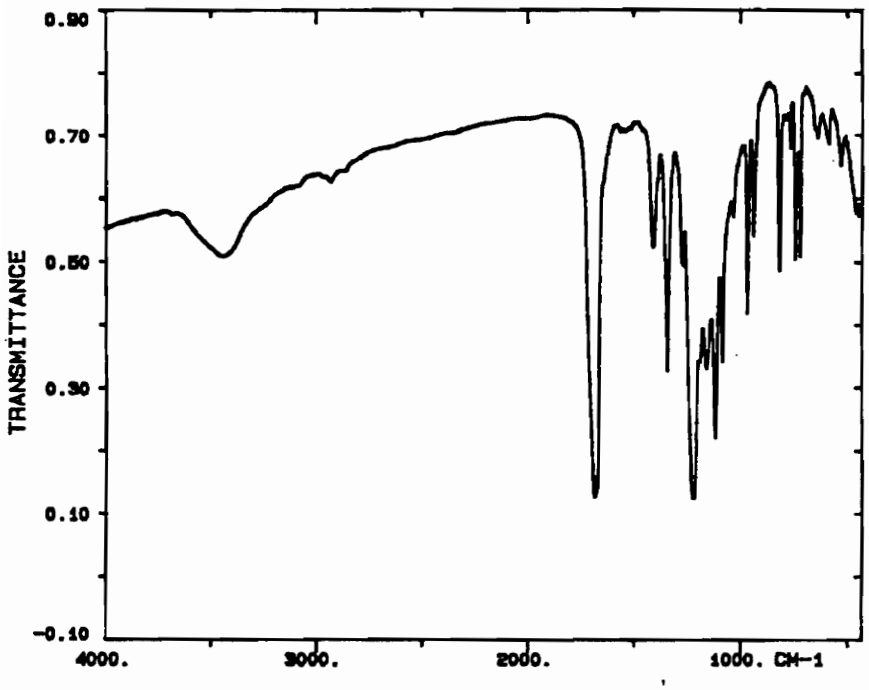

Pb(fod)$_2$ decomposition: 350 °C, 30 min

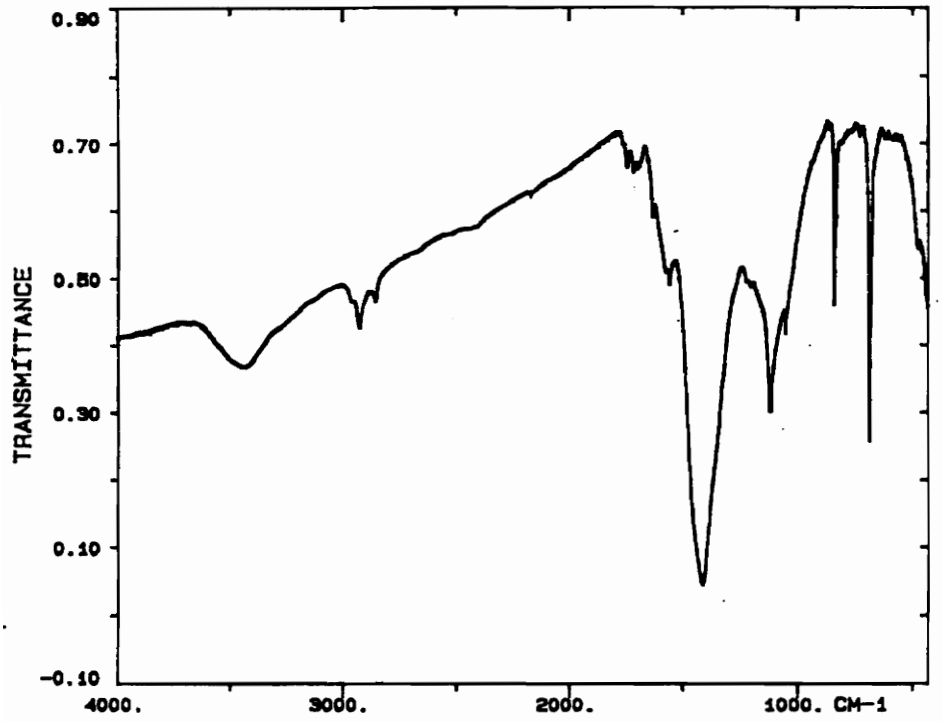

Pb(fod)$_2$ decomposition: 400 °C, 30 min

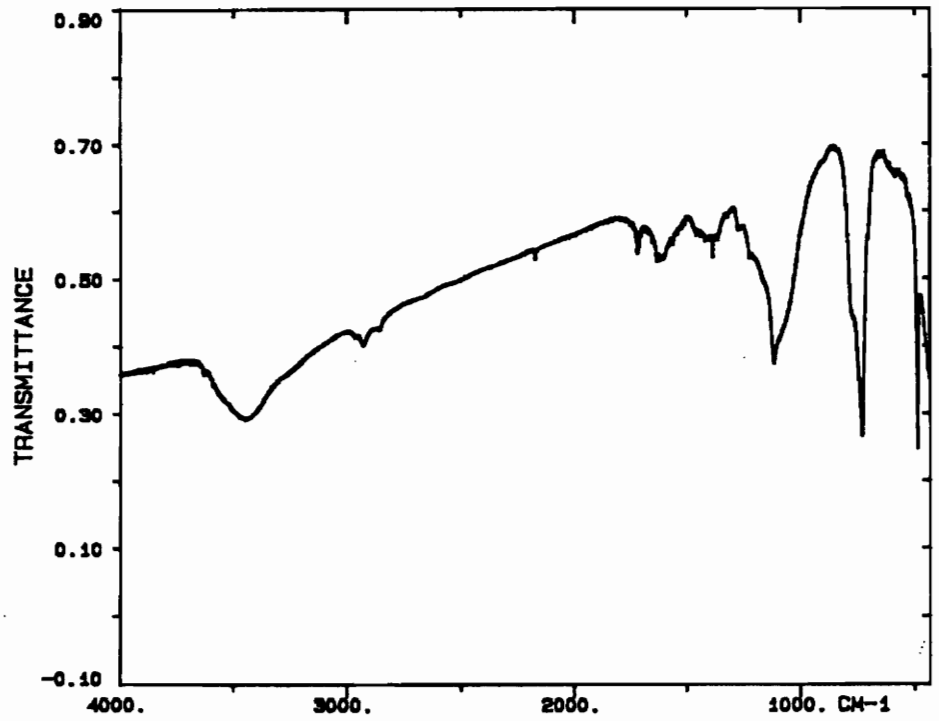

APPENDIX D:

Mass spectra of lead and zirconium β-diketonates, and decomposition products from TGA experiments and decomposition experiments

Zr(thd)$_4$ precursor

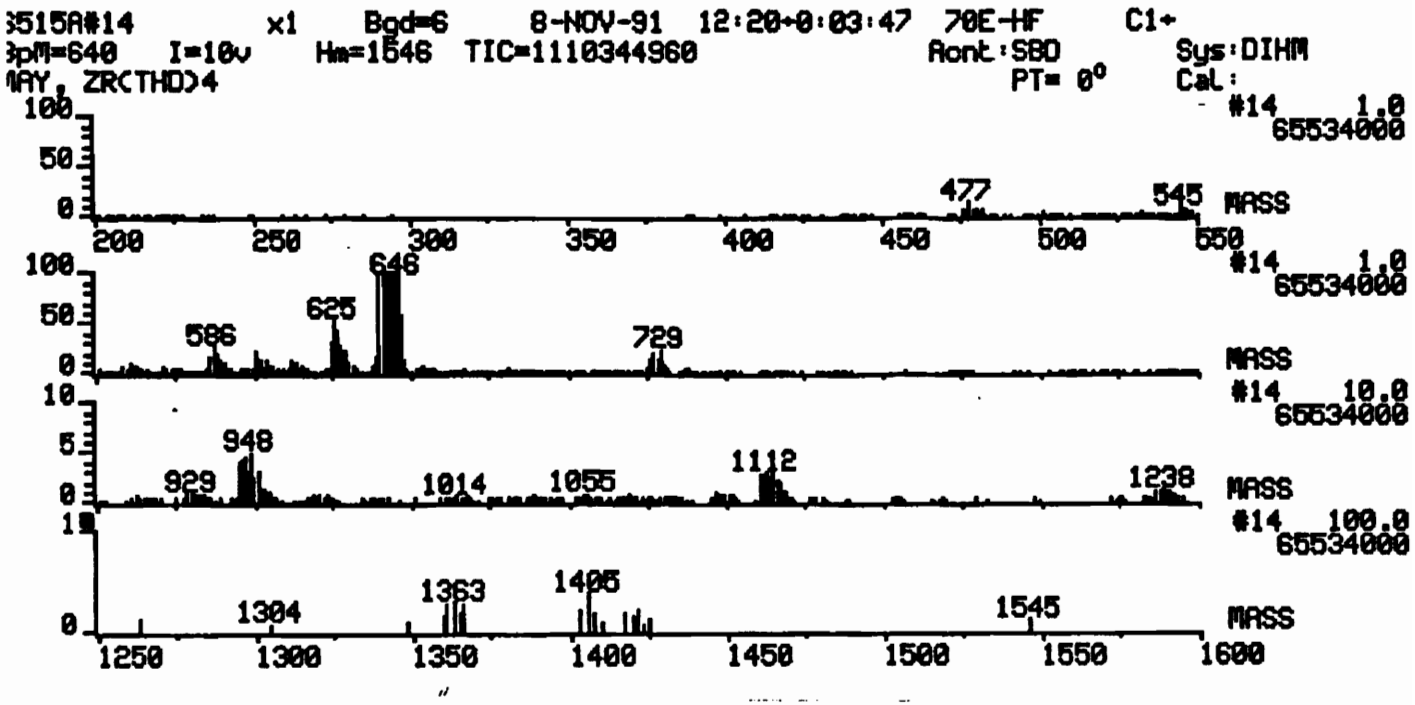

$Zr(thd)_4$ precursor
(low mass range)

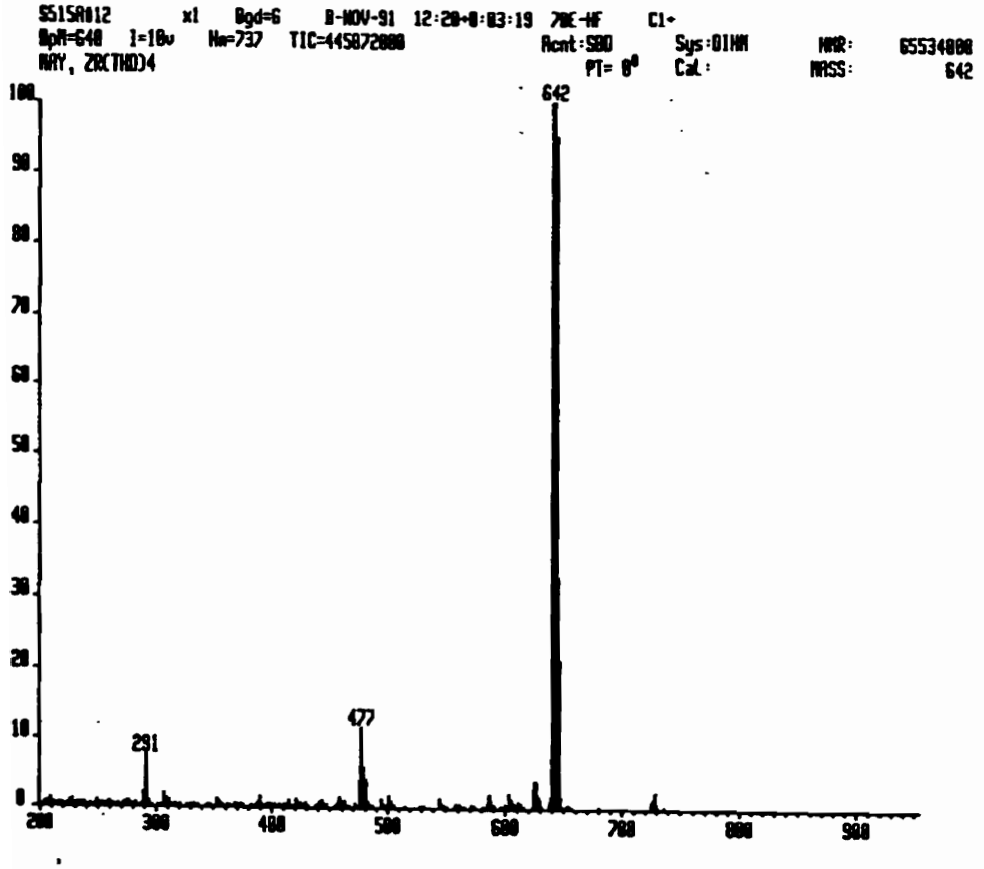

Zr(thd)$_4$ precursor
(high mass range)

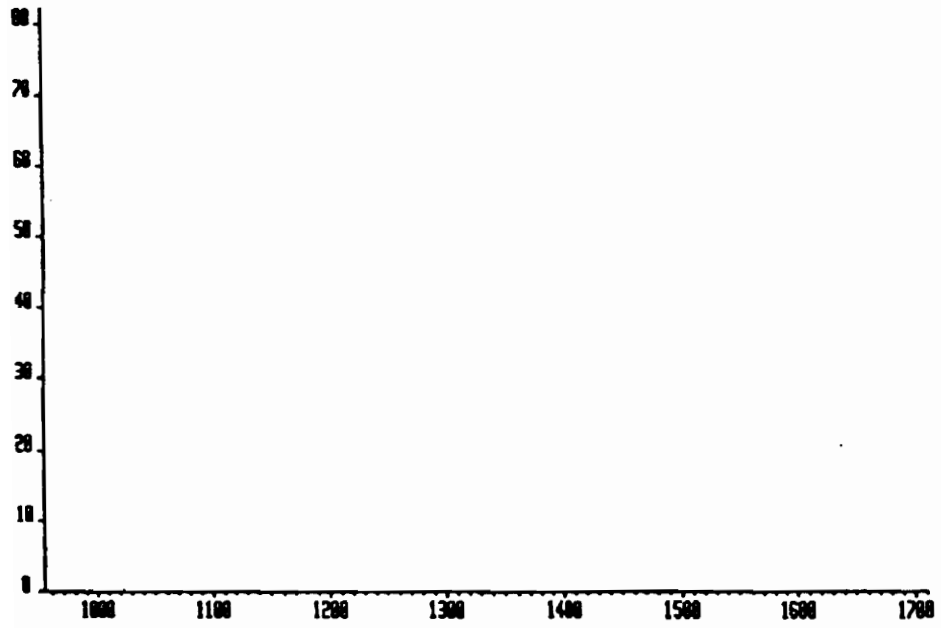

Pb(fod)$_2$ precursor (low mass)

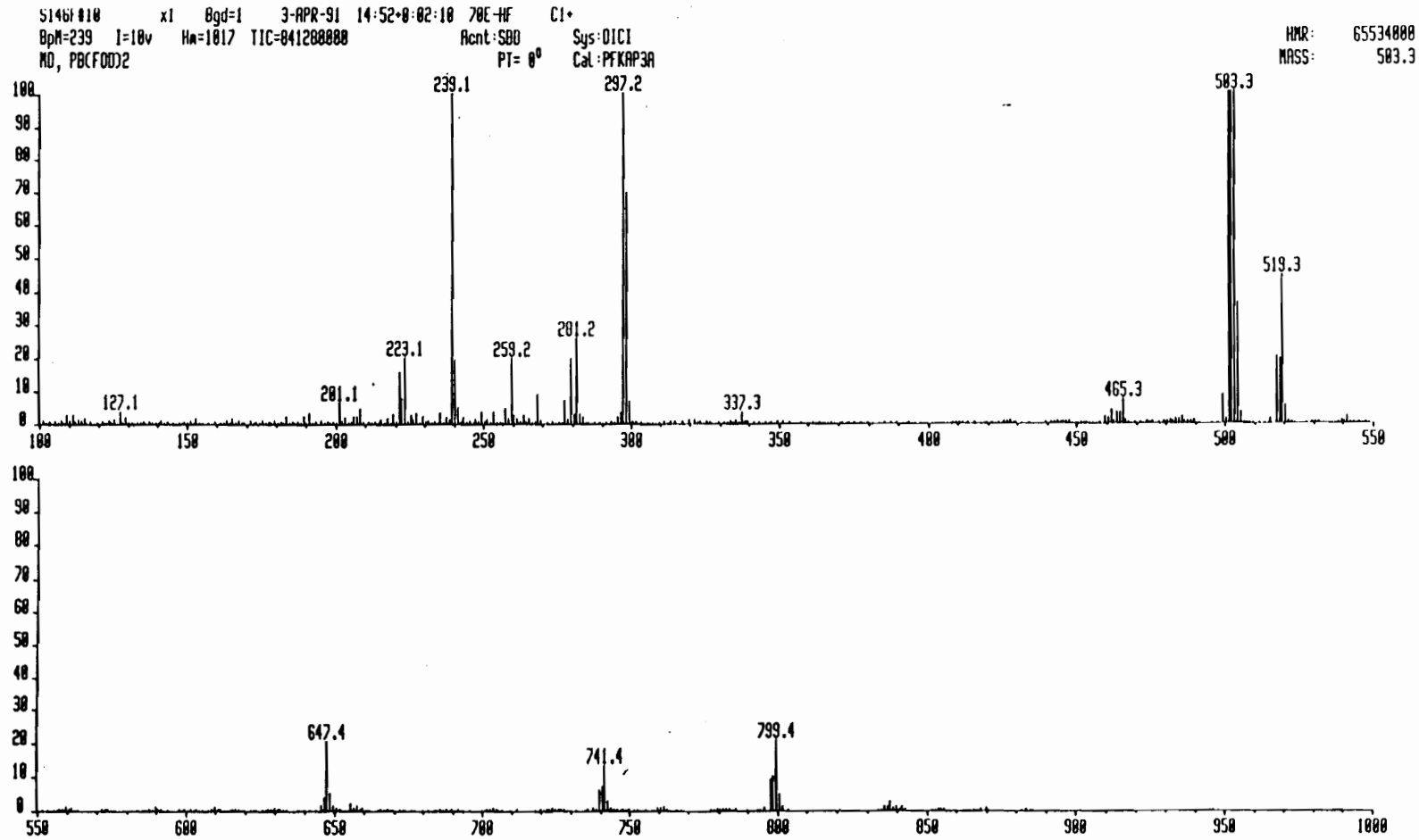

Pb(fod)$_2$ precursor (high mass)

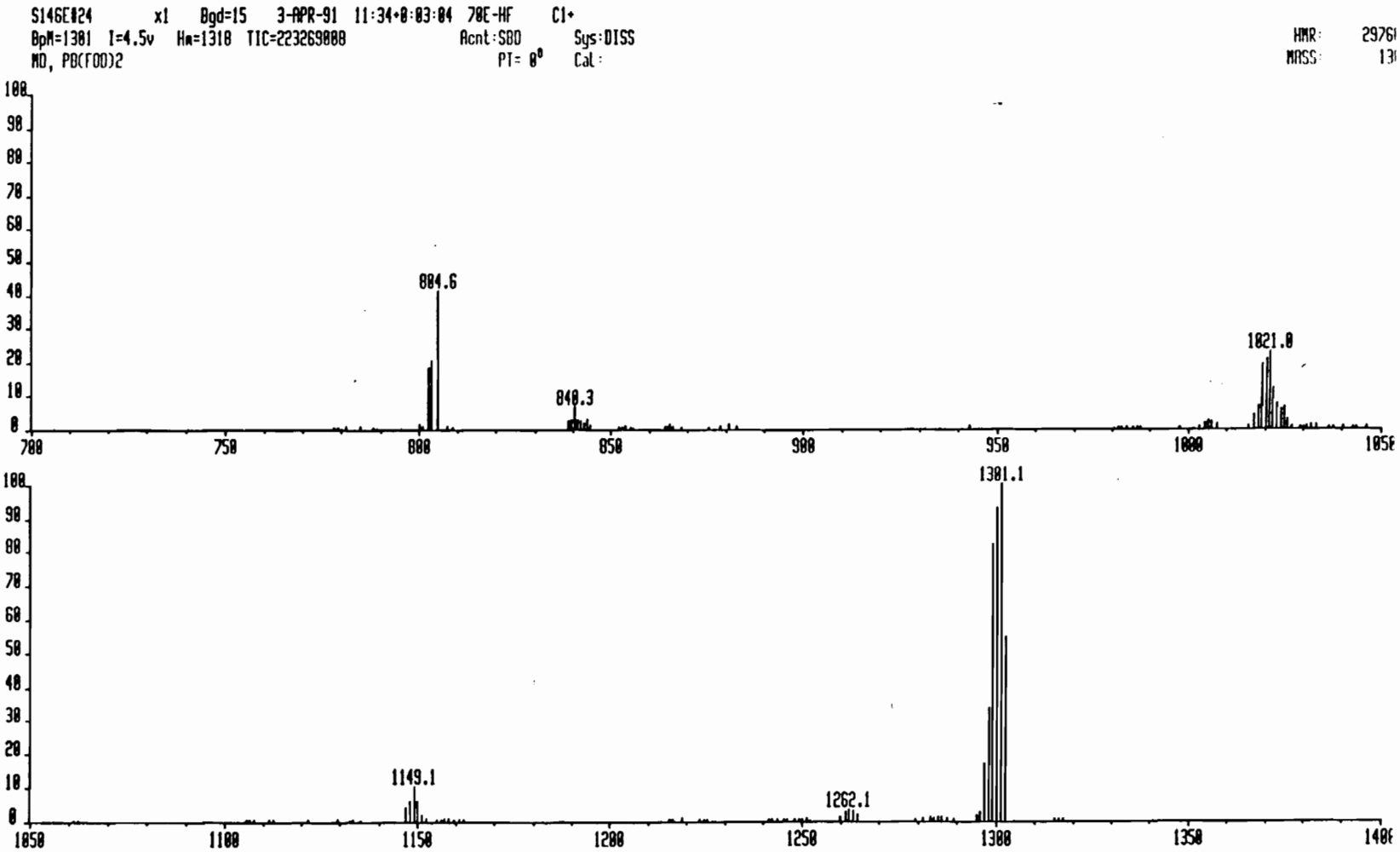

$Pb(thd)_2$ precursor

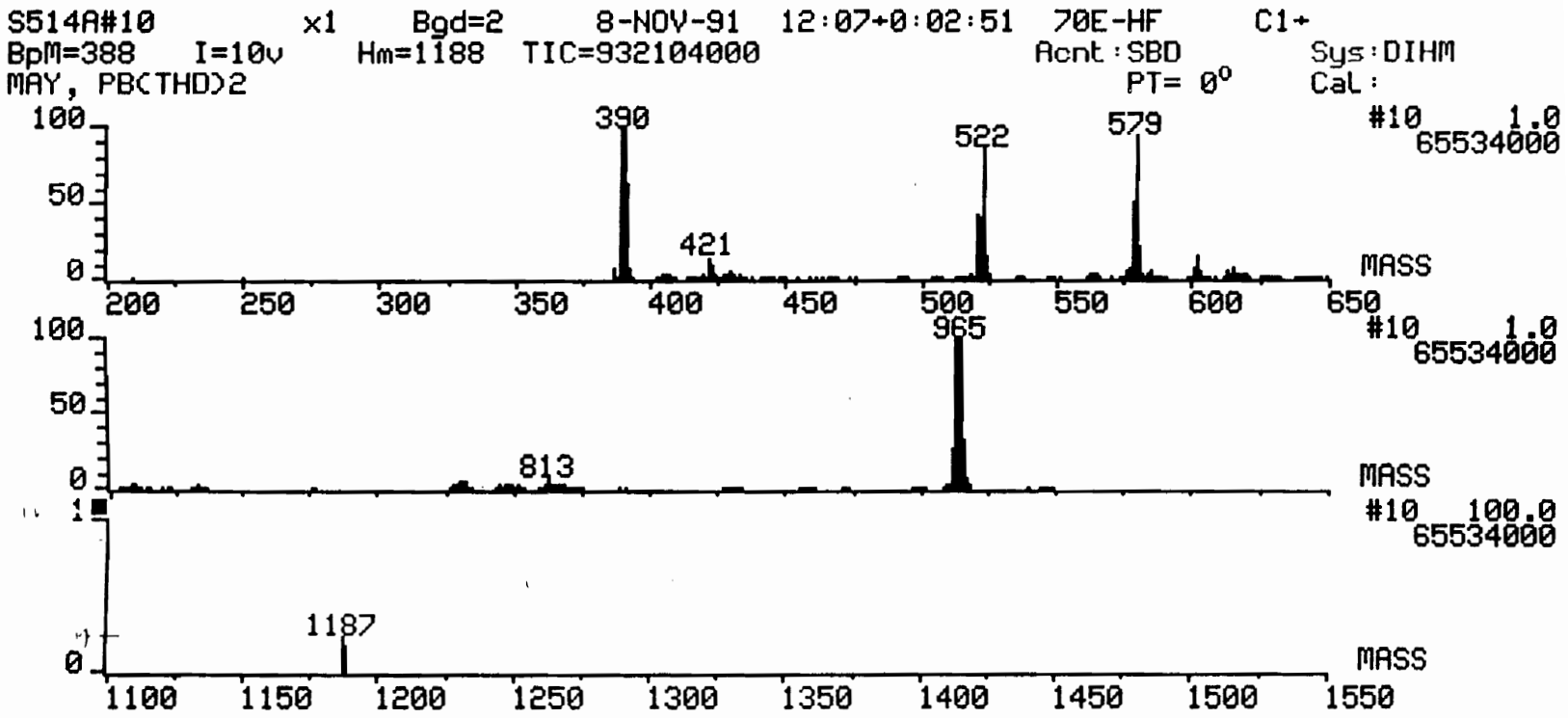

unsublimed fraction of $Pb(fod)_2$ heated at 140 °C in a nitrogen purge

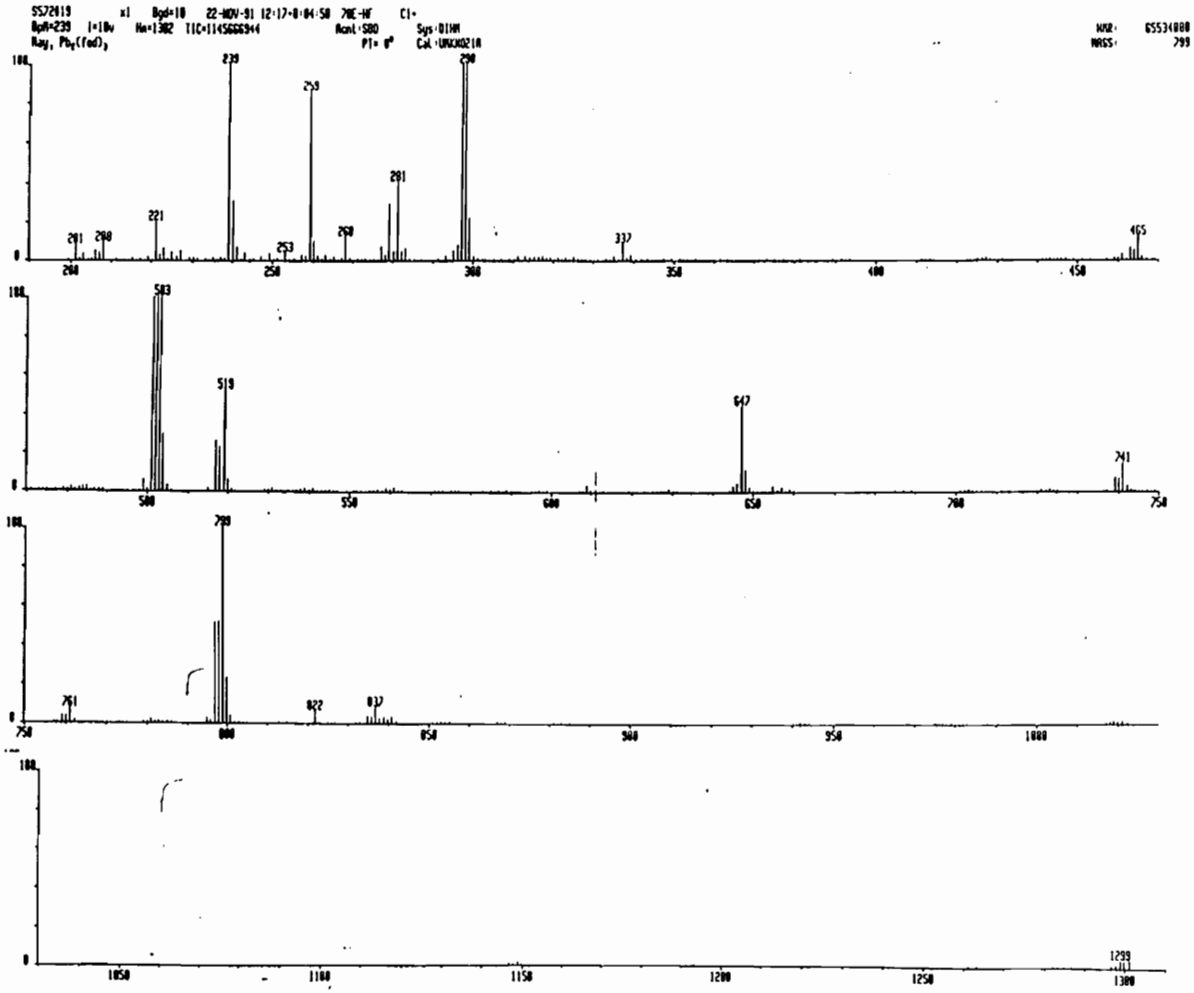

unsublimed fraction of $Pb(thd)_2$ heated at 140 °C in a nitrogen purge

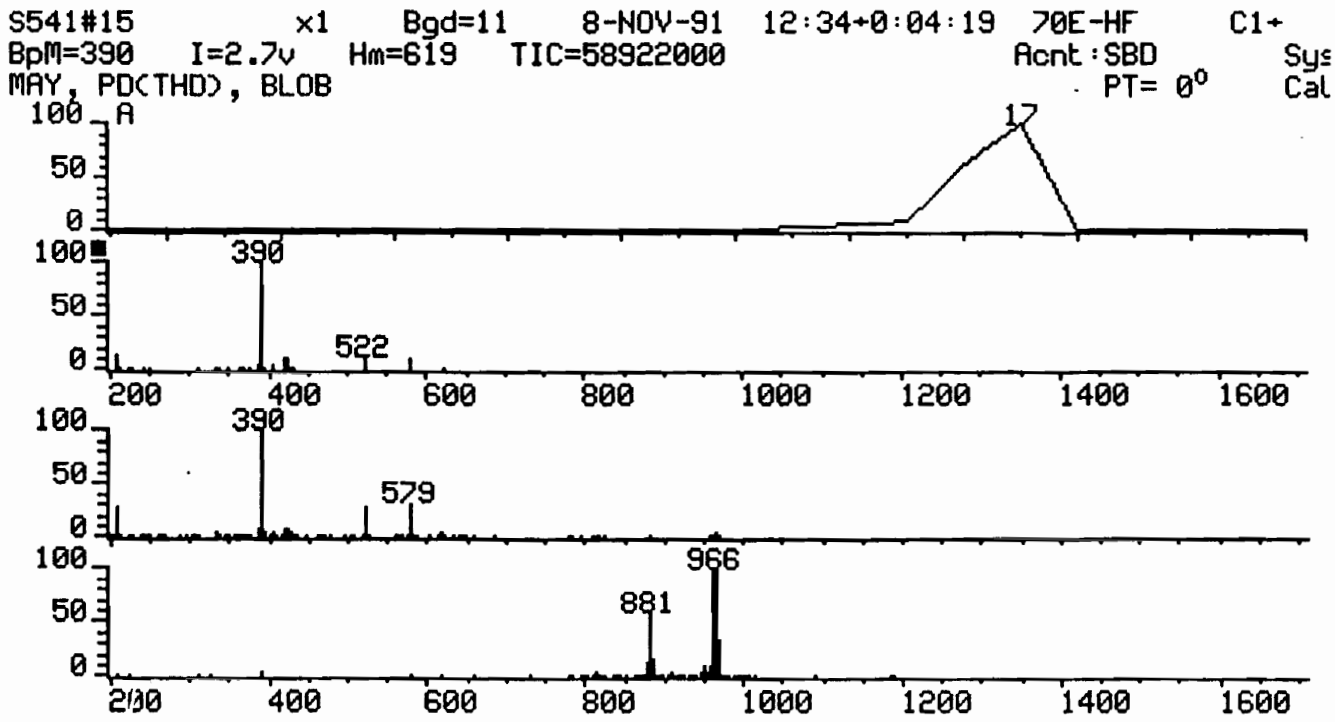

$Zr(thd)_4$ decomposition products (in O_2 atmosphere): 350 °C, 40 min

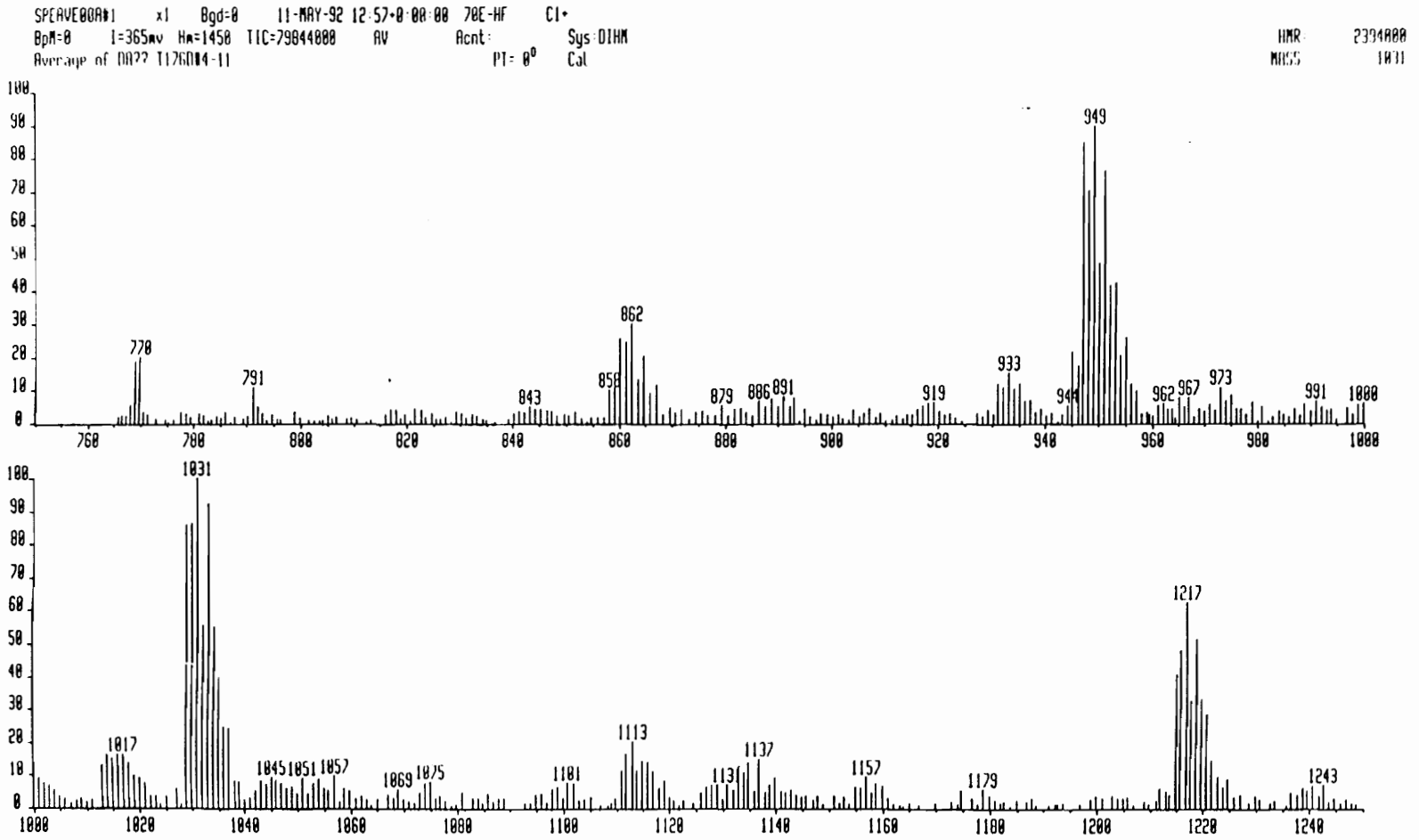

Pbthd)$_2$ decomposition products (in O_2 atmosphere): 300 °C, 40 min

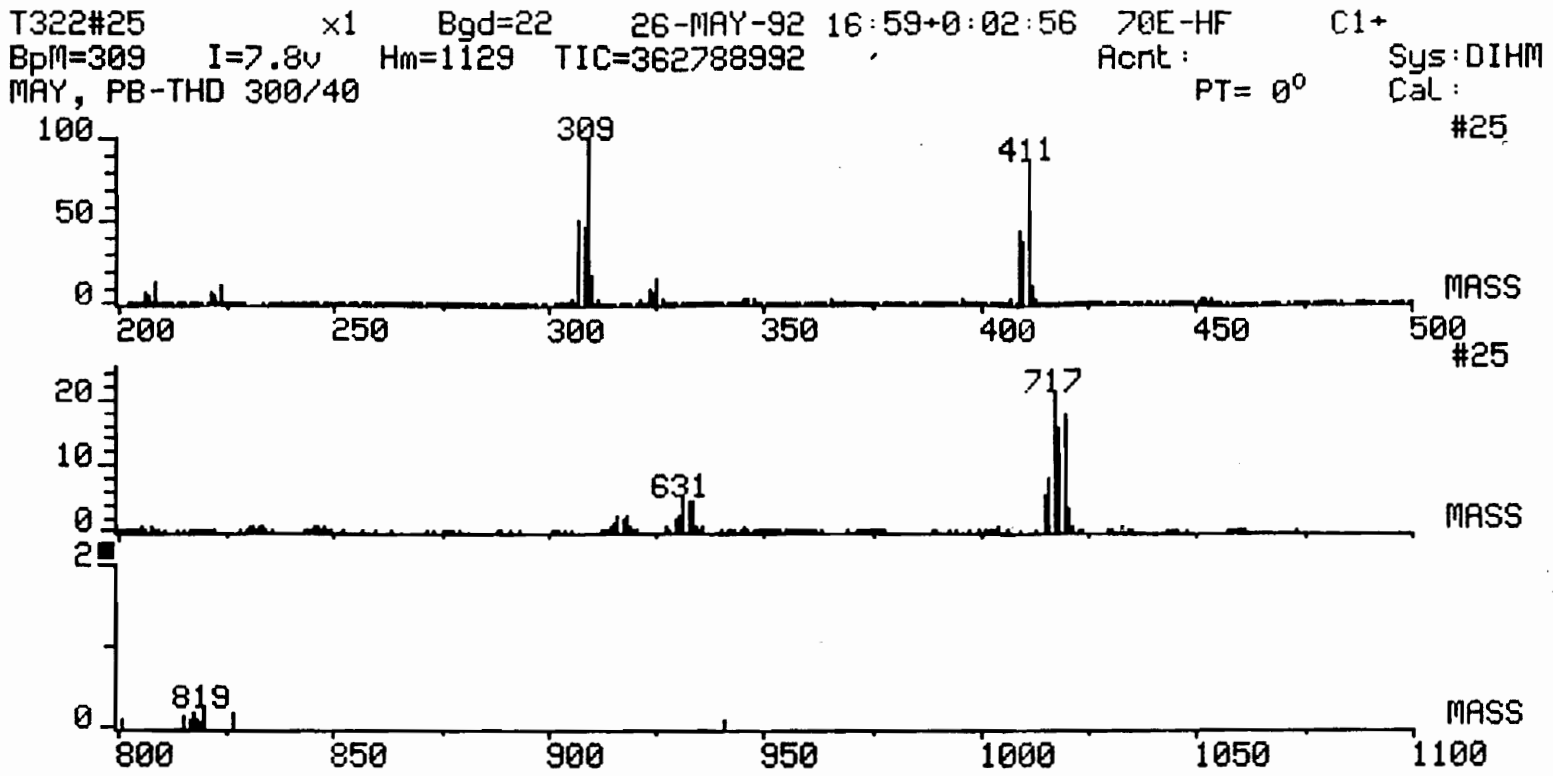

VITA

May Nyman was born as May Devan on August 17, 1967 to Judy and Leroy Devan in Lawrence, Kansas. She married Matthew Nyman, August 1991, and they are still on their honeymoon. She grew up in Fredericksburg, Virginia where she graduated from Stafford High School in 1985. May attended Florida Atlantic University (Boca Raton, Fl.) from 1985-1987, and graduated (finally) from Virginia Tech (Blacksburg, Va) in 1990 with a B.S. in Geology and a minor in Chemistry. From Fall 1990 to Summer 1992, she pursued her M.S. in the Department of Materials Engineering and Science, and graduated July, 1992. May will continue her education at the University of New Mexico, Department of Chemistry, where she will pursue a PhD.